

UC Riverside

UC Riverside Electronic Theses and Dissertations

Title

Titanium Vascular Stents With Rationally-Designed Sub-Micrometer Scale Surface Patterning

Permalink

<https://escholarship.org/uc/item/8wv4b085>

Author

Gott, Shannon

Publication Date

2014

Peer reviewed|Thesis/dissertation

UNIVERSITY OF CALIFORNIA
RIVERSIDE

Titanium Vascular Stents With Rationally-Designed
Sub-Micrometer Scale Surface Patterning

A Dissertation submitted in partial satisfaction
of the requirements for the degree of

Doctor of Philosophy

in

Mechanical Engineering

by

Shannon Cristina Gott

December 2014

Dissertation Committee:

Dr. Masaru P. Rao, Chairperson

Dr. Victor G. J. Rodgers

Dr. Guanshui Xu

Copyright by
Shannon Cristina Gott
2014

The Dissertation of Shannon Cristina Gott is approved:

Committee Chairperson

University of California, Riverside

ACKNOWLEDGEMENTS

I would like to thank my advisor, Dr. Masa Rao, for his continual mentorship, encouragement, and dedication to fostering growing students that has developed me into the researcher I am today. For his leadership and ability to guide his team to independent thinkers, I will always be grateful.

To my fellow Biomedical Microdevice Laboratory members, thank you for your support and comradery throughout the years that made our team productive and enjoyable. And to part of the team, my labmates Clara Zhang, Omid Khandan, and Ryan Peck, I would like to specially thank for being sounding boards and partaking in the joys and woes of developing titanium etching. During all those long drives and late nights in the cleanroom, I am indebted to your companionship as we helped each other grow personally and professionally.

Much of the work that we sought to do would not have been possible without our excellent collaborators in bioengineering, Dr. Victor Rodgers and Dr. Prashanthi Vandurangi. Their expertise and work in understanding the mechanisms behind cell-substrate interactions was key in forwarding this research. Outside the professional sphere, I greatly appreciated their special friendship that aided me in my graduate school journey.

My fabrication research would not have gotten half as far as it did without the direction, dedication, and friendship of Dr. Brian Thibeault, Dr. Ning Cao, and the rest of the cleanroom staff at the University of California, Santa Barbara as well as Dr. Dong Yan and the rest of the cleanroom staff at the University of California, Riverside. The

tutelage and knowledge in cleanroom techniques and during all the phases of process development was indispensable to the success of this work.

For the commitment of Mr. Danny Bogen from Machine Solutions Inc. to graduate students and their research, I am very thankful. Danny offered his time and expertise with stents and balloon catheters to troubleshoot with me during early stage development of the planar-to-cylindrical stent transformation.

I also acknowledge the generous funding from the University of California, Riverside and the National Science Foundation Graduate Research Fellowship Program that made this research possible.

To my family and my church family I owe a great deal of gratitude. I will probably never know all of the ways I have been blessed over the years in graduate school by the love, support, and prayers from mom, dad, grandma, grandpa, Steven, and Donald. Thank you each one for not letting me have a choice but to be a part of your life and for laughing, crying, rejoicing and praying with me through it. I love you all. And for AdventHOPE, which was my home away from home and my Sabbath rest each week, I praise God for you and the way you have helped me to grow.

DEDICATION

I dedicate this work to God as principle investigator in my life the author and finisher of all. – Hebrews 12:2

ABSTRACT OF THE DISSERTATION

Titanium Vascular Stents With Rationally-Designed Sub-Micrometer Scale Surface Patterning

by

Shannon Cristina Gott

Doctor of Philosophy, Graduate Program in Mechanical Engineering
University of California, Riverside, December 2014
Dr. Masaru P. Rao, Chairperson

Drug-eluting stents have revolutionized the field of interventional cardiology by reducing incidence of restenosis through local delivery of drugs that inhibit inflammation caused by implantation-induced injury. However, growing evidence suggests that this may also inhibit reestablishment of the endothelium, thus delaying healing and increasing potential for thrombogenic stimulus. Herein, we discuss progress towards realization of next-generation titanium (Ti) stents that seek to mitigate adverse physiological responses to stenting via rational design of stent surface topography at the micro- and sub-micrometer scale.

To better understand the effect of surface topography on cells, we evaluate the *in vitro* response of EA926 endothelial cells (EC) to variation in precisely-defined, micrometer to sub-micrometer scale groove-based topography, with groove widths ranging from 0.5 to 50 μm . Silicon (Si) and Ti materials are chosen for these studies due to their relevance for implantable microdevice applications, while grating-based patterns

are chosen for their potential to induce elongated and aligned cellular morphologies reminiscent of the native endothelium. We show significant improvement in cellular adhesion, proliferation, and morphology with decreasing feature size on patterned Ti substrates. Moreover, we show similar, yet attenuated, trending on patterned Si substrates as compared to patterned Ti substrates. These results suggest promise for sub-micrometer topographic patterning to enhance endothelialization and neovascularisation for implantable microdevice applications.

We also discuss: 1) advances which now allow patterning of features in Ti substrates down to 150 nm, which represents the smallest features achieved to date using our novel Ti deep reactive ion etching (Ti DRIE) technique; 2) creation and evaluation of balloon-deployable, cylindrical, surface-patterned stents from micromachined planar Ti substrates; and 3) integration of these processes to produce a device platform that allows, for the first time, evaluation of surface patterning in more physiologically relevant contexts, e.g. *in vitro* organ culture. Using elasto-plastic finite element analysis, we also explore planar stents with novel locking mechanisms intended to address radial stiffness deficiencies observed in earlier studies. Collectively, these efforts represent key steps towards our long-term goal of developing a new paradigm for stents in which rationally-designed surface patterning provides a physical means for complementing, or replacing, current pharmacological interventions.

TABLE OF CONTENTS

ACKNOWLEDGEMENTS	iv
DEDICATION	vi
ABSTRACT OF THE DISSERTATION	vii
LIST OF FIGURES	xiii
LIST OF TABLES	xvi
1 INTRODUCTION	1
1.1. Cardiovascular Disease	2
1.2. The Artery	2
1.3. Current Situation With Stenting	3
1.3.1. Stents: Bare-Metal Stents & Restenosis	3
1.3.2. Stents: Drug-Eluting Stents & Thrombosis	4
1.3.3. Stents: DES & Cost Effectiveness	5
1.3.4. Stents: Passively Addressing Neointimal Hyperplasia	6
1.4. Rationale for Integrating Nanopatterning and Stents	7
1.4.1. Nanotopography: Background	7
1.4.2. Nanotopography: Vascular Cells & Random Features	8
1.4.3. Nanotopography: Rational Ti Features and Vascular Cells	9
1.4.4. Impetus to Pursue a Rationally Patterned Stent Platform	10
1.5. Stent Design	12
1.6. Scope of this Work	13
2 METHODS	16
2.1. Introduction	17
2.2. Materials	17
2.2.1. Titanium	17
2.2.2. Silicon	18
2.3. Deposition	19

2.4.	Lithography	20
2.4.1.	Lithographic Techniques for Sub-Micron Patterning of Titanium	21
2.4.1.1.	Deep UV Projection Lithography	21
2.4.1.2.	Laser Interference Lithography	22
2.4.1.3.	Nanoimprint Lithography	23
2.5.	Reactive Ion Etching	24
2.6.	Titanium Etching.....	25
2.6.1.	Sub-Micron Ti Etching – Experimental Design	26
2.7.	Pattern Characterization	34
2.7.1.	Scanning Electron Microscope	34
2.7.2.	Focused Ion Beam.....	35
2.7.3.	Atomic Force Microscopy	36
3	CREATION AND EVALUATION OF SURFACE PATTERNING ON PLANAR TITANIUM.....	37
3.1.	Introduction	38
3.2.	Materials and Methods	40
3.2.1.	Patterned Substrate Design	40
3.2.2.	Patterned Substrate Fabrication	40
3.2.3.	Patterned Substrate Characterization	44
3.2.4.	Endothelial Cell Culture	45
3.2.5.	Endothelial Cell Assays	46
3.2.6.	Immunostaining	46
3.2.7.	Fluorescent Imaging.....	48
3.2.8.	Scanning Electron Microscopy of Cell-seeded Substrates	49
3.2.9.	Cellular Morphology Quantification.....	49
3.2.10.	Statistical Analyses	49
3.3.	Results	50
3.3.1.	Patterned Substrate Characterization	50
3.3.2.	Endothelial Cell Adhesion and Proliferation	54
3.3.3.	Endothelial Cell Morphology and Cytoskeletal Architecture.....	56
3.3.4.	Endothelial Cell Function	65

3.4.	Discussion	66
3.4.1.	Endothelial Cell Response as a Function of Substrate Material and Topography	66
3.4.2.	Comparison to Previous Studies	69
3.4.3.	Implications for Ti- and Si-based Implantable Microdevices.....	70
4	TITANIUM STENT CREATION AND INTEGRATION WITH SUB-MICROMETER SCALE SURFACE PATTERNING	72
4.1.	Introduction	73
4.2.	Materials and Methods	75
4.2.1.	Design Considerations	75
4.2.2.	Finite Element Analysis	77
4.2.3.	Fabrication	81
4.2.4.	Mechanical Testing	84
4.3.	Results	86
4.3.1.	Fabrication	86
4.3.2.	FEA Simulation and Mechanical Testing	87
4.4.	Discussion	94
4.4.1.	Deep Sub-Micrometer Scale Surface Patterning	94
4.4.2.	Surface Patterned Balloon-Deployable Ti Stents	95
4.4.3.	Mechanical response	97
5	TITANIUM STENT DESIGN IMPROVEMENT	98
5.1.	Introduction	99
5.2.	Materials and Methods	99
5.2.1.	Design Considerations	99
5.2.2.	Fabrication	103
5.2.3.	Finite Element Analysis	104
5.3.	Results and Discussion.....	106
5.3.1.	Fabrication	106
5.3.2.	FEA Mechanical Response	106

6	CONCLUSIONS.....	112
6.1.	Recommendations for Future Work.....	114
	BIBLIOGRAPHY.....	117
	APPENDIX.....	129
	Appendix A – Substrate Preparation.....	129
	Appendix B – Deposition (ICP PECVD).....	133
	Appendix C – Lithography	136
	Appendix D – Reactive Ion Etching	146
	Appendix E – Miscellaneous Tools and Methods	154
	Appendix F – Tool Process Flow.....	156
	Appendix G – Ti Material Properties.....	158
	Appendix H – Finite Element Analysis via Femap	162

LIST OF FIGURES

Figure 2-1. FIB cross-section of 150 nm gratings. Platinum deposited.....	29
Figure 2-2. FIB cross-section of 200 nm gratings. Carbon deposited.	30
Figure 2-3. FIB cross-section of 300 nm gratings. Carbon deposited.	31
Figure 2-4. FIB cross-section of 400 nm gratings. Carbon deposited.	32
Figure 2-5. FIB cross-section of 500 nm gratings. Carbon deposited.	33
Figure 3-1. Schematics of the patterned Ti (left) and Si (right) substrates used in the current study. Each substrate is composed of an array of nine sub-patterns, one of which is left unpatterned to serve as a control, and the other eight of which consist of groove-based gratings with groove widths indicated in the schematic.	41
Figure 3-2. Fabrication processes for the patterned Ti (left) and Si (right) substrates. Patterned Ti substrate fabrication: 1) SiO ₂ deposition by PECVD, followed by PR application; 2) Lithographic patterning via thermal NIL with patterned Si imprint master; 3) Pattern transfer to SiO ₂ by F-based dry etching; 4) PR removal and Ti DRIE etch; and 5) Final SiO ₂ removal by F-based dry etching. Patterned Si substrate fabrication: 1) PR application; 2) Lithographic exposure via projection lithography; 3) PR development and O ₂ plasma descum; and 4) F-based dry etching and PR removal.	42
Figure 3-3. Scanning electron microscope micrographs of patterned Ti (left) and Si (right) substrates with 0.5 μm, 0.75 μm, and 50 μm gratings, as well as unpatterned control surfaces.	51
Figure 3-4. Scanning electron microscope micrographs of 0.5 μm grating sub-pattern cross sections from patterned Ti (left) and Si (right) substrates. The Ti grating was imaged in a tilted orientation, while the Si grating was imaged without tilt. The bright layer covering the upper foreground surface of the Ti grating is a Pt film deposited prior to focused ion beam milling. This film protected the underlying structures from sputtering-induced faceting during milling. The vertically-oriented contrast 1 variations observed beneath the Ti grating are “curtain effect” artifacts produced by differential sputtering during milling.....	53
Figure 3-5. Human endothelial cell densities on patterned Ti and Si substrates and tissue culture plastic at varying time points ranging from 30 min (i.e. 0 days) to 5 days. Data = mean ± SEM (**p = 0.01, ****p = 0.0001; unpaired samples T-test, n = 5).....	55

Figure 3-6. Scanning electron microscope micrographs of human endothelial cells after 1 day culture on 0.5 μm gratings and unpatterned sub-patterns of Ti (left) and Si (right) substrates. Arrows indicate filopodia and lamellopodia.	57
Figure 3-7. Scanning electron microscope micrographs of human endothelial cells after 5 day culture on patterned Ti (left) and Si (right) substrates. Each micrograph depicts a single field of view located at the boundary between the 0.5 μm and 50 μm grating sub-patterns, as illustrated in the schematics below the micrograph. Dotted lines indicate boundaries of the sub-patterns and double arrows indicate grating directions.	58
Figure 3-8. Fluorescent micrographs of human endothelial cells after 5 day culture on 0.5 μm gratings and unpatterned sub-patterns of Ti (left) and Si (right) substrates. Double arrows indicate grating direction.	59
Figure 3-9. Confocal micrographs of human endothelial cells after 5 day culture on 0.5 μm gratings and unpatterned sub-patterns of Ti (left) and Si (right) substrates. Cells were immunostained using phalloidin (red) for cytoskeletal protein F-actin, and Hoechst 33342 (blue) for nuclei. Double arrows indicate grating direction.	61
Figure 3-10a. Confocal micrographs and quantification of vWF expression (red), a human endothelial cell protein, after 1 day culture on 0.5 μm gratings and unpatterned sub-patterns of Ti and Si substrates, and tissue culture plastic. Nuclei (blue) were cross-stained using Hoechst 33342. Double arrows indicate grating direction. Data = mean \pm SEM (**p = 0.01, ***p = 0.001; unpaired samples T-test, n = 10).	63
Figure 3-10b. Confocal micrographs and quantification of VCAM-1 expression (red), a human endothelial cell protein, after 1 day culture on 0.5 μm gratings and unpatterned sub-patterns of Ti and Si substrates, and tissue culture plastic. Nuclei (blue) were cross-stained using Hoechst 33342. Double arrows indicate grating direction. Data = mean \pm SEM (**p = 0.01, ***p = 0.001; unpaired samples T-test, n = 10).	64
Figure 4-1. Schematic depiction of a portion of the planar stent form design. All units in micrometers.	78
Figure 4-2. Digital micrographs of the Ti stent transformation process: a) Planar stent form deep etched through an 80 μm thick Ti substrate; b) Initial phase of tapered needle threading process to transform the planar stent form into a compact cylindrical geometry for balloon mounting; c) Balloon-mounted stent; and d) Ti stent after deployment into a mock artery via balloon inflation (stent removed from mock artery for image).	78
Figure 4-3. Fabrication process flow for surface-patterned planar Ti stent forms.	85
Figure 4-4. SEM micrographs of 0.15 μm groove width grating defined in a planar Ti substrate by Ti DRIE: a) High magnification; b) Low magnification. Grating pitch is 0.3 μm and groove depth is 0.8 μm	88

Figure 4-5. SEM micrographs of a balloon-deployed, surface-patterned Ti stent produced by Ti DRIE: a) Full stent; b) Torsionally deformed side-beam and adjoining cross-bands; c) Region of severe cross-band deformation; and d) 0.75 μm groove width surface patterning in a heavily deformed region.	89
Figure 4-6. Elastoplastic FEA simulation of stent deployment: a) Initial configuration; and b) Von Mises stress plot of deployed device.	91
Figure 4-7. Normalized load-displacement data for mechanical testing and FEA-based simulation of deployed stents under uniaxial radial compression: a) Ti stent, measured; b) Ti stent, FEA; c) 304 SS stent, FEA; and d) Commercial stainless steel stent, measured. Inset: Magnified view of elastic deformation regime. Note: Stents in a), b), & c) share identical design and dimensions.	92
Figure 4-8. Deformation response of deployed Ti stent after 1.5 mm uniaxial radial compression: a) Longitudinal view of FEA simulation; and b) Longitudinal view SEM micrograph of tested stent.	93
Figure 5-1. Schematic depiction of a portion of the planar hex stent design. All units in millimeters	101
Figure 5-2. Fabrication process flow for surface-patterned planar Ti stent forms.	102
Figure 5-3. SEM micrographs of the Ti hex stent transformation after fabrication: a) Planar hex stent deep etched through an 80 μm thick Ti substrate; b) Hex stent after balloon deployment to 3 mm diameter, inset: higher magnification of single hex link showing locking hooks.	107
Figure 5-4. FEA deployment response for single link of Ti hex, Ti involute, and commercial stent designs.	109
Figure 5-5. FEA compression response for single link of Ti hex, Ti involute and commercial stent designs.	110
Figure G-1. Stress-strain data for each Ti dogbone tensile test performed.	159
Figure G-2. Ti dogbone stress-strain data averaged according to orientation.	160
Figure G-3. Ti dogbone stress-strain data averaged across orientations.	160
Figures G-4. Close-up of the elastic region of Figure G-3.	161

LIST OF TABLES

Table 2- 1. Ti surface pattern size dependent etch rate.....	33
Table 3-1. Scanning electron microscope measurements of sub-pattern feature dimensions on patterned Ti and Si substrates, including grating groove width, ridge width, and pitch (i.e. groove width + ridge width). Data = mean \pm standard deviation, n = 5.....	52
Table 3-2. Atomic force microscope measurements of sub-pattern ridge-top surface roughness on patterned Ti and Si substrates, including average roughness (R_a), root mean square roughness (R_{sq}), and maximum roughness (R_{max}). Data = mean \pm standard deviation, n = 5.	52
Table 3-3. Confocal microscopy measurements of human endothelial cell elongation ratio and angular deviation (from the grating axis) after 5 day culture on patterned Ti and Si substrates. Angular deviation on unpatterned sub-patterns was determined relative to an arbitrary reference axis that was held fixed for each field of view. Data = mean \pm standard deviation, n = 5.....	62
Table 5-1. Representation of the progressive link deformation during FEA.....	108
Table G-1: Average Mechanical Properties for 80 μ m thick CP Grade 1 Ti.....	161
Table H-1: Abbreviated stress vs. strain data of 80 μ m thick Ti foils for FEA.....	169

1 INTRODUCTION

1.1. Cardiovascular Disease

Coronary heart disease (CHD) is the leading cause of death in the United States and other developed countries with an estimated death toll of 7.2 million men and women each year (Mackay *et al.* 2004). In the United States, approximately 1 in every 6 deaths is caused by CHD, with over 1 million people being affected by a coronary event each year (Roger *et al.* 2011). The disease has also imposed a significant economic burden in the United States of more than \$177 billion in 2007 (Roger *et al.* 2011). Therefore, it is evident that there is a need for a safe and effective solution to CHD. While the disease takes different forms, the most common is cardiovascular disease (CVD) and is caused by atherosclerosis, which is characterized by a fatty material called plaque building up beneath the endothelium, a layer of endothelial cells that comprise the innermost part of a vessel. The result is arterial narrowing, or stenosis, and an inhibition of blood and oxygen to the heart. Symptoms consist of, but are not limited to, shortness of breath, chest pain, and heart attack. Current treatments for CVD include: angioplasty and stent placement to re-open the blocked vessel, coronary artery bypass surgery to graft new vessels around the atherosclerotic narrowing, or a drug regimen to prevent CVD escalation. This work is primarily interested in the advancement of those minimally invasive stent technologies.

1.2. The Artery

Arteries are comprised of multiple tissue layers, function to transport blood from the heart, and are a typical destination for stent placement. The innermost layer is called the tunica intima and is composed of a single thickness of endothelial cells (endothelium)

in direct contact with the blood and an elastic membrane lining (basement membrane). Aligning in the direction of blood flow and reducing friction, endothelial cells have a unique spindle shape that is not manifested when cultured on flat surfaces and/or in the absence of flow. The basement membrane is a thin (primarily collagen) fibrous sheet that provides an anchor for endothelial cells undergoing flow shear stress.

The middle and outer artery layer are called the tunica media and tunica adventitia, respectively. In contrast to the tunica intima, the tunica media is comprised of smooth muscle, collagen, and elastin that are transversely arranged to help them contract or dilate to maintain blood pressure. Meanwhile, the tunica adventitia prevents overexpansion from blood flow with its connective tissues, collagen and elastic fibers. Understanding the anatomy of the artery (in particular the endothelium, basement membrane, and smooth muscle) as well as the mechanisms of CVD and the responses to CVD treatment, aids in the development of stenting technologies.

1.3. Current Situation With Stenting

1.3.1. Stents: Bare-Metal Stents & Restenosis

Stents are mesh-like cylindrical structures that are radially expanded at the site of vessel narrowing to push back the plaque-laden vessel walls and maintain patency. First generation stents, or bare-metal stents (BMS), were designed with purely mechanical functionality and can suffer from restenosis, which is the build-up of vascular smooth muscle cells inside the intima that can lead to lumen narrowing. During stenting, there are two main factors that can lead to restenosis (Edelman and Rogers 1998): 1) When the

balloon is opened and pushes back the plaque in the walls, it damages the artery wall (Kirchengast and Munter 1998); and 2) the artery can react to the stent when it perceives it as a foreign body and mounts an immune system response. As to the former, damage to the blood vessel wall by angioplasty triggers a physiological response that can be divided into two stages. The first stage that occurs immediately after tissue trauma is thrombosis. A blood clot forms at the site of damage and further hinders blood flow. This is accompanied by an inflammatory immune response. The second stage is the result of proliferation of smooth muscle cells in the intima. In response to vascular trauma, growth factors are produced that stimulate smooth muscle cells to start dividing, with 90% of the final intimal proliferation being produced in the first 2 weeks as the smooth muscle cells multiply 3 to 5 times within that period (Marx *et al.* 2011). As the smooth muscle cells multiply, they push through the openings in the stent mesh and cause a narrowing in the stent lumen. This is also known as neointimal hyperplasia. All this leads to the remodeling of the vessel and restenosis.

1.3.2. Stents: Drug-Eluting Stents & Thrombosis

Since then, second generation drug-eluting stents (DES) have revolutionized the field of interventional cardiology by reducing incidence of restenosis through local delivery of drugs that inhibit inflammation caused by implantation-induced injury. However, four prominent studies (Garg and Serruys 2010) raised concerns over the increased mortality in DES. These studies found that stent thrombosis emerged as a major, unpredictable safety issue and, though rare, associated mortality rates can be as

high as 20-30%. These findings led to a large collaborative study that compared stent thrombosis in BMS and DES. It was found that very late stent thrombosis (> 1 year) had higher rates in DES. One of the factors thought to initiate stent thrombosis was incomplete endothelialization. Since the drugs delivered are not target cell specific, they prevent a healthy layer of endothelial cells from forming, thus delaying healing and increasing potential for thrombogenic stimulus.

1.3.3. Stents: DES & Cost Effectiveness

Another issue with DES was emphasized in a worldwide cost effectiveness comparison between BMS and DES (Neyt *et al.* 2009). In three independent studies from the United States, DES were more than triple the price of BMS. The results of this analysis indicated DES was not cost effective for the overall population, excluding certain subgroups, i.e. diabetics, patients with long lesions, or lesions in narrow vessels. The conclusion drawn in this encompassing study, therefore, was that DES has no impact on mortality or on the occurrence of heart attack when compared with BMS. Many proponents of DES, however, suggest they are more cost effective because revascularization (the reopening of an artery that has closed again due to restenosis) is not a problem. This study states, though, that in real world situations, the absolute reduction in repeat revascularization with DES compared to BMS is small. The main barrier for the cost effectiveness of DES is the good performance and safety profile of BMS (Neyt *et al.* 2009).

One aspect of the DES cost was missing from this analysis, though, and that is the long term dependence on dual-antiplatelet therapy. Since platelet aggregation is the basis of thrombosis, current late stent thrombosis mitigation strategies rely on oral dual antiplatelet therapies (DAPT), such as aspirin and clopidogrel. However, clopidogrel is ineffective for ~25% of patients (Gurbel *et al.* 2003; Lau *et al.* 2004) and may interact adversely with other common drugs (e.g. proton pump inhibitors) (O'Donoghue *et al.* 2009). Moreover, poor patient compliance is common with oral therapies, and is implicated in increased risk of death for those on DAPTs (Spertus *et al.* 2006). Patients that are compliant undergo dual-antiplatelet therapy for an indefinite period of time that often extends to the rest of the patient's life. This regimen can be costly since it consists of at least two, and sometimes three, drugs. Another consideration is that the typical stent recipient will often need other surgeries, requiring them to cease the anticoagulants during that time and opening the potential for thrombosis to occur.

1.3.4. Stents: Passively Addressing Neointimal Hyperplasia

Due to the issues also present with DES, several studies (Nazneen *et al.* 2012) are now looking for another way of addressing restenosis and the hyperproliferation of vascular smooth muscle cells by promoting rapid re-endothelialization over the stent. It has been shown (Bjorkerud and Bondjers 1973; Clowes *et al.* 1978; Fishman *et al.* 1975; Haudenschild and Schwartz 1979) that there is an inverse relationship between the luminal endothelial cell coverage and the vascular smooth muscle cell proliferation after arterial injury. One study (Asahara *et al.* 1995) delivered vascular endothelial growth

factor (VEGF), in order to stimulate endothelial growth after balloon-induced arterial injury, and followed with immunostaining for proliferating cell nuclear antigen (PCNA). It was reported that the rapid re-endothelialization was linked to the suppression of neointimal hyperplasia, since the VEGF-treated group had less intimal thickening than those untreated. Moreover, this is supported by the observation that most of the intimal proliferative activity (PCNA-positive cells) is concentrated in non-endothelialized regions for both animal groups. As such, this provides opportunity to explore a new stent paradigm not reliant on pharmacological means to address restenosis through promoting re-endothelialization and healing.

1.4. Rationale for Integrating Nanopatterning and Stents

1.4.1. Nanotopography: Background

The nanotopography present in the body inspired the idea of patterning the stent surface in an effort to facilitate healing by obtaining a layer of endothelial cells on the stent. Topographical features on the nanoscale are prevalent throughout the body and the basement membranes of many tissues, which interact directly with adjacent cells. These tissues are comprised of a complex mixture of nanoscale pores, ridges, and fibers. Nanopatterning, as used in biological research, is available largely due to the ‘smaller, faster, cheaper’ technology drive of the semiconductor industry. As a result, topographies with a dimensional range similar to the cellular environment are now possible, and features with dimensions below 100 nm are now emerging in biological applications (Balasundaram and Webster 2006).

With these capabilities, there is now a growing body of knowledge (Bettinger *et al.* 2009) about cell-substrate interactions. Some of the common features studied include grooves, pits, posts, and randomly-rough features. Through these studies, researchers found that cells have a wide array of responses to topography, which depend on many factors including cell type, feature size and geometry, and the physical properties of the material. It is the latter that directs our focus to titanium (Ti), due to its corrosion resistant TiO₂ surface layer, making it suitable for contact with blood, as well as its track record for biocompatibility in prosthetics and dental implants. Overall, this body of knowledge has great significance that translates to the novelty of this work: topography alone can be used to elicit different responses in the same cell type.

1.4.2. Nanotopography: Vascular Cells & Random Features

Since the reactions to topography depend on cell type, we are interested in the response of vascular cells to promote endothelialization. Studies (Buttiglieri *et al.* 2003; Choudhary *et al.* 2006; Chung *et al.* 2003; Dalby *et al.* 2002; Miller *et al.* 2004) looking at cardiovascular cells and endothelial cells in particular, have shown enhanced adhesion, spreading, and migration on nanostructured surfaces. One such study (Choudhary *et al.* 2006) looked at the response of endothelial cells and smooth muscle cells to nanometer roughness. It was found that on all surface nanostructured samples there was an increase in both endothelial cell and smooth muscle cell adhesion compared to the smooth-surfaced samples. This study suggested that the nanostructured surfaces allowed for favorable protein surface interactions that improved initial adhesion. In each of these studies,

however, the topography was random, such that, there was limited control over the arrangement and size of the feature. Since it has been shown (Bettinger *et al.* 2009) that small changes in the dimension and spatial orientation of features can elicit different effects from cells and that specifically shaped features can be used to obtain a desired cellular response, then a precisely controlled and rationally designed topography on a stent surface may provide a way to enhance healing and the endothelial function in stenting.

1.4.3. Nanotopography: Rational Ti Features and Vascular Cells

As was first reported elsewhere (Lu *et al.* 2008; Lu *et al.* 2007; Rao *et al.* 2008), rational design of surface topography at the microscale may provide a new means for facilitating healing, thus increasing safety and efficacy. Specifically, one of the first *in vitro* studies demonstrated that planar titanium (Ti) substrates patterned with gratings composed of grooves ranging in width from 0.75 to 100 μm were able to increase endothelial migration and promote cellular morphology similar to that of the native endothelium, both of which would be expected to facilitate healing. Grating surface patterning was chosen specifically for its ability to elongate the cells in the direction of the grooves, which mimics the natural morphology of endothelial cells that elongate in the direction of blood flow. Results of this study showed that endothelial cell density increased significantly as pattern dimensions decreased to the nanometer scale with the endothelial cells ultimately forming a confluent layer on the Ti substrates. Furthermore, a competitive co-culture study (Rao *et al.* 2008) of vascular cells showed an increase in endothelial cell adhesion and simultaneous decrease in smooth muscle cell adhesion,

which suggests potential for inhibiting restenosis as well as facilitating healing. Finally, favorable trending was observed of these effects with decreasing feature size. Since the extracellular matrix is typically composed of collagen fibrils with diameters ranging from 260 – 410 nm (Bozec *et al.* 2007), there may be greater gains possible with further reduction of surface pattern feature sizes to these dimensions. Collectively, these results have provided the impetus to enhance Ti micromachining techniques in order to create smaller features sizes as well as to couple the rationally-designed surface patterns with a more physiologically-relevant platform, i.e. the surface of stents, for subsequent cell studies.

1.4.4. Impetus to Pursue a Rationally Patterned Stent Platform

While a multitude of studies have explored the effect of various types of nanoscale topography on vascular cells, the vast majority have focused on *in vitro* cultures on planar substrates. It is conceivable that some of the surface structuring approaches described in these studies could be translated to actual stents as well, however, there have been only limited reports in this regard thus far (Dibra *et al.* 2005; Wieneke *et al.* 2003). In these studies, stents with randomly structured nanoscale topographies (hereafter referred to simply as nanostructured surfaces) were found to have only minimal impact on restenosis *in vivo* relative to stents with smooth surfaces.

The lack of demonstrable benefit provided by nanostructured surfaces *in vivo* would seem to discourage further study. However, it is important to recognize that the stents sought to be developed in the current effort will possess highly anisotropic,

grating-based topographies with precisely-defined feature size, depth, and morphology (hence the designation nanopatterned surfaces). This distinguishes them from nanostructured surfaces, which typically possess relatively isotropic surface features with large variation in size, depth, and morphology. This is a key distinction for a number of reasons. First, numerous *in vitro* studies have shown that nanopatterned surfaces may elicit more desirable cellular responses than both smooth surfaces and nanostructured surfaces with features of comparable length scale (Bettinger *et al.* 2009). Second, although not nanopatterned specifically, Fuss *et al.* demonstrated enhanced endothelialization *in vivo* on stainless steel stents with microscale grooved surfaces (12 – 15 μm groove width range), relative to stents with smooth surfaces (Fuss *et al.* 2001). Continuing beyond this pilot study, (Sprague *et al.* 2012) compared three groups of identically designed stents, except for their surface characteristics: stainless steel with grooved surfaces (15 μm groove width), stainless steel with smooth surfaces, and cobalt chromium with smooth surfaces. It was observed that there was a significant increase in endothelial cell coverage at 3 days and decrease in neointimal thickness at 28 days for the grooved stents as compared to both smooth surfaced stents. When coupled with the previous *in vitro* studies mentioned demonstrating enhanced endothelial response on sub-micrometer scale gratings relative to microscale gratings (Lu *et al.* 2008), this suggests potential for even greater endothelialization on nanopatterned stents *in vivo*. Third, previously mentioned studies have also demonstrated that sub-micrometer gratings can significantly enhance competitive adhesion and proliferation of endothelial cells over vascular smooth muscle cells (Rao *et al.* 2008), thus suggesting potential for promoting

endothelialization and inhibiting restenosis *in vivo*. Finally, studies have also shown that sub-micrometer gratings can induce more native endothelial morphology relative to larger microscale gratings (Lu *et al.* 2008). This is particularly important, since this suggests potential for recapitulating more native functionality as well, which is crucial for ensuring long-term stenting success. It is not yet known whether such favorable results will translate to *in vivo* settings; however, the surface-nanopatterned stents developed in the current effort will eventually enable such studies to be performed. As such, our Ti stent platform should also possess the necessary mechanical qualities to function as a stent.

1.5. Stent Design

To provide a platform on which surface patterning could be tested inside the body, a stent compatible with our surface patterning techniques is needed. Typically, stents are fashioned from laser cut tubes, but manufacturing stents in this manner would prevent the creation of submicron grooves, given that the minimum spot size of common lasers used in industry (CO₂ and Nd:YAG) (Dubey and Yadava 2008) is within the micron realm (Martinez and Chaikof 2011). Also, laser cutting produces burrs and splatter that adheres to the underside of the cut, which must be removed by electropolishing to achieve a smooth-surfaced final product (Kathuria 2005). Electropolishing is a chemical etching process that removes surface material when a current passes to the workpiece in an electrolyte. As such, it would significantly damage all surface patterning.

Micromachining, however, is an economical way to create submicron features in Ti with good dimensional control without the need for electropolishing. Micromachining utilizes batch production, whereas laser cutting is a serial process, so there is potential to reduce the manufacturing costs. The planar requirements for creating nanoscale gratings necessitate development of processes for creating cylindrical stents from planar substrates. A previous study outlines the implementation of a 2D stent design in 304 stainless steel using microelectrodischarge machining (Takahata and Gianchandani 2004). Takahata and Gianchandani showed that a planar stainless steel stent meets the stiffness standards and excels in flexibility over conventional stainless steel stents.

1.6. Scope of this Work

Based on the aforementioned knowledge, this work seeks to achieve three specific objectives detailed below that support the long-term goal of developing a deeper understanding of the effects of rationally-designed sub-micron patterning on vascular response and applying this understanding to the enhancement of the safety and efficacy of vascular stents. Since this work is based on the hypothesis that rationally-designed sub-micron surface patterning will enhance desired vascular cell responses relative to the uncontrolled surfaces typical of most stents, as well as randomly nanostructured surfaces, we seek to develop novel micro/nanofabrication processes that allow testing of this hypothesis at smaller feature sizes and under more physiologically-relevant conditions. Through the following objectives, this will be accomplished: 1) Development of techniques for sub-micron patterning and cellular evaluation of model Ti surfaces; 2)

Development of techniques for realization of 3-D stent geometry comparable to conventional stents; 3) Integration of 3-D stents with rationally-designed sub-micron patterning.

Herein, lithography and plasma etching process techniques were developed, resulting in surface patterning on flat Ti substrates with dimensions down to 150 nm. The characterization of such surfaces reveals nanoscale precision of feature dimensions when using our novel Ti micromachining techniques process over feature dimensions. In addition, the adhesion, proliferation, and signaling of endothelial cells in response to the surface patterning shows favorable trending with decreased feature sizes.

The ability to use the novel Ti micromachining techniques to through-etch thin foils and create a platform (i.e. a stent) for advanced surface pattern evaluation was demonstrated. Techniques for transforming the initially-flat stent into a cylindrical form are detailed, which allowed for comparison to commercially available stents. After balloon deployment, the Ti stents maintained patency of the test vessels with no obvious stent-vessel separation, despite lower radial stiffness under uniaxial compression testing when compared to commercially available stents.

The robust nature of the surface patterning is also seen when combining the stent platform and surface patterning. After deployment, the pattern remained intact with little spatial disturbance in high deformation areas. This demonstrated the ability to integrate the patterning with devices that can be placed in the body, and more specifically, it opened the way to explore the potential for sub-micron surface patterning to enhance endothelialization *ex-vivo*. *Ex-vivo* studies are currently underway.

As a way to allow for future stent design improvements, finite element analysis (FEA) of the stent deployment process and mechanical testing was recreated and validated with experimental results. This highly nonlinear analysis closely correlated to experimental results in the elastic region of the curve, giving an accurate assessment of the radial stiffness of the current design and a means to test alternate designs economically. As a result, planar Ti stents with interlocking mechanisms designed to resist radial compression and increase radial stiffness show a marked improvement over the initial planar Ti stent using FEA. Collectively, each of our objectives are met, moving us closer to our long-term goal of developing a new paradigm for stents in which rationally-designed surface patterning provides a physical means for complementing, or replacing, current pharmacological interventions.

2 METHODS

2.1. Introduction

Each major material or tool key in the development of sub-micron surface patterned Ti stents is addressed here with a brief introduction outlining its importance and role in processing. Specific recipes concerning the preparation or use of the material or tool can be found in the appendix.

2.2. Materials

2.2.1. Titanium

Though it is generally acknowledged that no biomaterial is completely inert and free of adverse reactions, Ti is a widely accepted implantable material. Biocompatibility of a material is dictated by its low immune response activation, ability to integrate with surrounding tissue in healing, prevention of bacteria, corrosion resistance properties, and the mechanical requirements based on the surrounding environment (Tengvall and Lundstrom 1992). Titanium's biocompatibility is partly ascribed to the native 2-6 nm thick Ti oxide (TiO_2) layer that grows on the Ti surface (Brunette 2001). The TiO_2 acts as a physical barrier to corrosion that prevents three types of migration: 1) metal ions out of the bulk material; 2) anions into the metal and; 3) electron passage across the oxide (Balamurugan *et al.* 2008). As such, Ti is a relatively stable and inert biomaterial for vascular devices.

For this work, Grade 1 Commercially Pure (CP) Ti (Tokyo Stainless Grinding Co., Ltd, Tokyo, Japan) was used because the purity of the Ti is important for clean and precise micromachining of features. All foils are cold rolled to the desired thickness, annealed,

and then polished. Two thicknesses of Ti foils were used: 1) single side polished (ground and lapped), 200 μm thick foils for surface pattern studies, and; 2) double sided polished (lapped), 80 μm thick foils for stent studies. The latter were lapped only due to the manufacturing ability for the given foil thickness. Material properties for our specific 80 μm Ti foils were determined experimentally to aid our finite element analyses (see Appendix G).

2.2.2. Silicon

Silicon (Si) is widely used in the semiconductor industry due to its' extreme flatness, relative low cost, and ease of machinability (Madou 2002), and is therefore compatible with planar micromachining techniques. Also, there is a large body of literature devoted to the etching of Si, from which etching processes can be derived. One appealing aspect of Si is its surface roughness ($R_a \sim 0.2$ nm RMS) as compared to that of Ti ($R_a \sim 2$ nm RMS). While this difference appears small, it can have profound effects on the resolution of the features when dealing with light based lithographies (see 2.4 Lithography). For these reasons, Si is used in this work as an intermediary step to transfer patterns to Ti.

While Si is far easier to micromachine and process than Ti, it is largely not preferred for implantable or insertion devices that would potential undergo any type of load bearing because of its brittle nature that could lead to catastrophic failure (e.g. shards in the body). With this in mind, Si has been shown to have healthy neuronal tissue surrounding cortical implants six months after insertion, lending Si to a certain level of

biocompatibility (Edell *et al.* 1992; Schmidt *et al.* 1993). Ultimately, though, while Si is relatively inert its mechanical properties preclude its usefulness and safety with in the body under certain applications, allowing researchers to explore more ductile materials.

2.3. Deposition

Deposition techniques can form thin solid layers on top of substrates by either physical or chemical means. Physical vapor deposition (PVD) uses line-of-sight techniques such as sputter or evaporation to distribute solid, liquid, or vapor raw material to the substrate surface. Alternatively, in chemical vapor deposition (CVD), a vapor reacts with a hot surface ($\geq 300^{\circ}\text{C}$) and is conformally adsorbed to the substrate (Madou 2002). Due to its versatile nature and low temperature and pressure processing conditions, CVD is widely used in the semiconductor industry, especially with the introduction of plasma-enhanced CVD (PECVD). In PECVD, radicals for the film are provided by the plasma activation and the subsequent ion bombardment of the substrate provides the energy required for the reaction, which allows for lower temperatures. In addition, increased ion bombardment leads to good adhesion and step coverage, low pinhole density, higher deposition rates, and thicker oxides (Madou 2002). However, these films often have high amounts of hydrogen from the gas precursors, which can degrade the quality of the film in such ways that include: lower film density and higher etch rate.

Inductively coupled plasma (ICP) PECVD creates a high-density plasma in the reactor and utilizes gas precursors with less hydrogen to obtain a higher density film and slower etch rates (Yota *et al.* 2000). For these reasons, an ICP PECVD is used in this work

to deposit mask oxides for subsequent Ti etching steps. With an SiO₂ mask deposited with this high-density method, selectivity for Ti etching is in the range of (30-36):1 (Ti:SiO₂). This higher selectivity is important since our devices require through etching of bulk Ti foils. See Appendix B for deposition details and processing recipes.

2.4. Lithography

Lithography is a method of transferring a pattern to a surface. One of the most common forms is photolithography, which uses light and a photomask to transfer the pattern to a light-sensitive polymer called photoresist (PR). The type of PR used and the subsequent chemical treatments will determine whether the exposed region will become more or less soluble, dictating the area in which PR is removed and defining the pattern atop the substrate.

Lithography, as it has played a role in previous group experiments, allowed Lu *et al.* (Lu *et al.* 2008) to create rational patterns ranging in size from 100 μm to 0.75 μm for cell cultures. The previous methods (UV projection lithography) used for pattern creation have a resolution limit around 0.75 μm, which prevented smaller feature sizes from being created. Also, micromachining techniques are inherently planar, so they necessitate the use of flat substrates with very little roughness. As mentioned previously, titanium has a larger average roughness than the typical Si substrates used for micromachining, which creates a challenge for light-based pattern transfer directly onto Ti. A reflective substrate will, as the name implies, reflect light back through the PR. Incoming and outgoing light interfere with each other and produce standing waves, which, in turn, cause scalloped

sidewalls. This effect is worsened if the substrate is not flat, as the light will be reflected at various angles. Bottom antireflective coatings can reduce the reflectivity, but are not cure-alls for rough surfaces.

To overcome these challenges, this research focuses on the development of deep UV projection lithography, laser interference lithography, and nanoimprint lithography techniques for integration with flat Ti substrates that provide, for the first time, capability for minimum feature sizes as low as 0.15 μm , when coupled with our novel Ti micromachining techniques (Parker *et al.* 2005). Pattern geometries will match those of our previous studies (i.e. gratings), whose design was guided by the desire to foster cellular proliferation that mimics the vascular wall. See Appendix C for lithography details and processing recipes.

2.4.1. Lithographic Techniques for Sub-Micron Patterning of Titanium

2.4.1.1. Deep UV Projection Lithography

Projection lithography uses light and a series of lenses to project the mask pattern onto the PR-covered substrate surface. Resolution, the smallest feature able to be transferred, is limited by the imaging light source and the numerical aperture (NA) of the projection lens according to the Rayleigh equation: $\text{Res} \propto \lambda / \text{NA}$, where λ is the wavelength of the light source. Ultraviolet projection systems have a wavelength of 365 nm, while deep UV systems are less than 248 nm. Wavelengths are dependent on the use of ultraviolet light from gas-discharge lamps or excimer lasers for UV or deep UV, respectively. With available deep UV systems for our project, there is potential to make

dense feature sizes as small as 0.15 μm on Si. See Appendix C for projection lithography details and processing recipes.

2.4.1.2. Laser Interference Lithography

Laser Interference lithography (LIL) can create grating sizes below 0.15 μm on Si utilizing the Lloyds mirror setup. LIL can create periodic patterns on a substrate surface as a result of the interference of two laser beams. As such, it does not use photomasks and is limited in the geometries it can create. Laser interference lithography, though, is capable of economically creating uniform nanoscale patterns over a large area in a single exposure, unlike other lithographies, e.g. electron beam lithography, scanning probe lithography. This ability is critical for the eventual clinical translation (i.e. surface patterning a stent). Much like projection lithography, the minimum feature able to be realized is limited by the wavelength of the light source. Also, as previously mentioned, the feature possibilities are limited by the periodicity, though multiple exposures with reorienting the substrate can lead to hole or pillar features.

The Lloyds mirror setup is a common system for LIL and consists of a laser beam (325 nm wavelength He-Cd laser was used for this research) expanded and spatially filtered through a pinhole for coherent light. The collimating lens then directs light toward the mirror and substrate holder, which creates a grating pattern via light interference on the surface of the PR-covered substrate. The grating pitch (p) is governed by the equation $p = \lambda / (2\sin\theta)$, where λ and 2θ are the wavelength of the laser and angle of the incoming light and the wave-reflected light, respectively. The pitch is easily changed by rotating the

substrate holder and mirror to the appropriate angle. The system available to us, when oriented at 54° , yields ~ 100 nm gratings (pitch 200 nm) to complement those gratings produced by deep UV projection lithography. While created, this dimension of pattern was not used for cell studies. See Appendix C for LIL lithography details and processing recipes.

2.4.1.3. Nanoimprint Lithography

Nanoimprint lithography (NIL) is an economical, high throughput, and high resolution nanolithography that relies on the mechanical deformation of imprint resist to form patterns. Both projection lithography and laser interference lithography rely on light for pattern transfer. Quality of the pattern for light-based lithographies depends on the roughness of the substrate, since rougher surfaces increase reflected light scatter. Thus NIL possesses greater tolerance for surface roughness and, thus, is well suited to be used with Ti in conjunction with other lithographies.

Light-based lithographies can create the mold necessary for NIL in Si. When coated with a hydrophobic layer to prevent sticking, the mold serves as an imprint master to mechanically deform the thermoplastic polymer layer on top of the Ti substrate. During imprinting, the Ti is heated above the polymer's glass transition temperature (T_g) to promote polymer flow and fill the imprint master features. After decreasing the temperature below the polymer's T_g , the mold is removed, leaving a complementary replica of the mold pattern on the surface of the Ti.

With the ability to create imprint masters with features down to 100 nm, using the previous imprinting parameters was inadequate. Upon Si master demolding, the polymer tore away from the substrate for the 100 – 200 nm features. This is due to the difference in thermal expansion coefficients for Si ($3 \times 10^{-6}/^{\circ}\text{C}$ at 20°C) and Ti ($8.6 \times 10^{-6}/^{\circ}\text{C}$ at 20°C) (Callister 2007), which results in lateral strain that is concentrated at the lower inside corner of the polymer pattern (Hirai *et al.* 2003). Slow cooling in addition to releasing the applied pressure below the T_g has been shown (Wi *et al.* 2011) to relieve the thermal stresses and prevent pattern defects as well as the resist tearing due to the thermal mismatch and high-aspect-ratios. These techniques have been applied success and near perfect demolding down to $0.15 \mu\text{m}$. Following lithography, the grating patterns are ready for pattern transfer into the Ti via etching. See Appendix C for NIL lithography details and processing recipes.

2.5. Reactive Ion Etching

Reactive ion etching (RIE) is a dry etching technology that uses reactive plasma to remove material from the surface of a substrate. As with deposition, the use of plasma in etching processes allows for lower temperatures because the plasma is comprised of positive ions and neutral atoms/radicals that are more chemically reactive than the gas precursors. The RIE plasma and substrate interactions occur in a chamber with upper and lower plates, where the substrate resides on the lower plate. With the desired gases in the chamber, a radio frequency (RF) electromagnetic field (usually 13.56 MHz) is applied to create the plasma consisting of positive ions and free electrons. As a result of the large

voltage drop between upper and lower plates, the positive ions accelerate toward the negatively charged lower plate and remove material by chemical reaction or by transferring kinetic energy in collision. Due to the parallel plates and delivery of the reactive species, RIE is capable of creating anisotropic features, especially when compared with isotropic wet etching (Madou 2002).

Reactive ion etching is further improved by the application of an ICP source which creates high density plasma independent from the RF applied to the substrate (Madou 2002). The overall effect is to increase etch rates and directionality of the ions to further increase the anisotropic etch profiles. Since precise control of bulk etching and sub-micron scale surface topographies are important, the ICP RIE and the RIE are suited to meet the needs of the Ti and Si etching processes, respectively.

2.6. Titanium Etching

Titanium Inductively Coupled Plasma Deep Reactive Ion Etching (TI DRIE) is a plasma-based micromachining process that has provided, for the first time, opportunity for realization of high-aspect-ratio (HAR) anisotropic bulk micromachining for Ti-based micromechanical devices (Parker *et al.* 2005). Until recently, capability for Ti etching was limited to either thin films prone to residual stress-induced bowing or acid-based etching methods unable to produce precise features with HAR due to its isotropic nature (Aimi *et al.* 2004). TI DRIE uses Cl_2/Ar plasma generated in an inductively coupled plasma tool, which produces greater plasma density and ion directionality. The ionized gas bombards and modifies the Ti surface, resulting in etch products from the chemical reactions

between the elements of the material and the etch species generated by the plasma. These etch products serve as an important part of the TI DRIE process since they passivate the etched feature walls and prevent undercutting. Etch rates in excess of 2 $\mu\text{m}/\text{min}$ and a TiO_2 mask to Ti selectivity of 40:1 have been reported (Parker *et al.* 2005). Previously by our group, 0.75 μm dense gratings created by projection lithography were the smallest feature size reliably etched (Lu *et al.* 2008). Efforts to etch smaller features resulted in significant undercutting and feature lift-off, prompting an investigation into the sub-micron etching of Ti. See Appendix D for dry etching details and processing recipes.

2.6.1. Sub-Micron Ti Etching – Experimental Design

For the creation of implantable Ti micro devices with sub-micron scale surface patterning, the TI DRIE (Parker *et al.* 2005) process needed to be altered for the aforementioned reason. All Ti etching processes were performed on an ICP RIE (E620-R&D, Panasonic Factory Solutions, Japan) and parameters of the TI DRIE etch to be considered include: ICP source power, RF sample power, the pressure, and the Cl_2/Ar gas composition (as well as additions of O_2 as needed to aid passivation). Standard values for the TI DRIE process are 400 W ICP source, 100 W RF sample power, 100 sccm Cl_2 , 5 sccm Ar, 15 mTorr chamber pressure, and 10°C chiller temperature.

In an effort to improve the TI DRIE process for sub-micron surface patterning, each parameter was varied individually and substrates with gratings from 50 μm to 0.15 μm were etched and qualitatively characterized for dimensional accuracy, sidewall roughness, and anisotropy. As previously mentioned, the ICP source power controls the

plasma activation and modifying it will contribute to the amount of ionization and dissociation of the gas precursor, with higher powers creating higher ion and radical densities. The RF sample power dictates the energy of those ions striking the substrate surface (Madou 2002). When increasing and decreasing the ICP source and RF sample power from the baseline TI DRIE process, similar trends were observed as those stated in Parker *et al.* (Parker *et al.* 2005) (i.e. lower etch rate and rougher sidewalls with power drop, rougher local and global surfaces, etc.). As such, both the powers are kept at baseline for the new recipe.

Pressure is known to affect ion directionality and plays an important role in feature anisotropy. The trajectories of ionized gas are altered by ion-neutral collisions as well as ions scattered from the mask edge can contribute to lateral etching, which worsens with higher aspect ratios (Coburn and Winters 1989). Reduction in pressure allows the ions to accelerate toward the substrate with fewer collisions, thus keeping to their intended path as dictated by the RF sample power (Senturia 2005). With a pressure setting of 3.75 mTorr (lowest setting available), there is a marked improvement in sidewall quality. A decrease in etch rate is also noted, but not an issue since surface patterns are meant to be shallow as compared to the bulk material.

Another method to preserve the fidelity of the sidewalls is to increase the passivation. Since the passivation is thought to be a compound of Si/Ti/O/Cl, the oxygen content can be increased in the plasma to assist in sidewall passivation creation. This method has been employed in Cl₂ plasma etching of InP (Carlstrom *et al.* 2006). It was found in this study that additions of O₂ aided sidewall passivation and prevented chlorine

radicals from interacting with sidewall material. Remaining chlorine radicals at the bottom of the feature were activated by ion bombardment, leading to vertical etching (Carlstrom *et al.* 2006). While certain amounts of O₂ can protect the sidewall from undesired etching, excessive quantities can lead to over passivation of the trench floor, causing micromasking. Also, additions of O₂ to plasma have been shown to dissociate molecular Cl₂ and increase the amount of atomic chlorine via ClO, thus enhancing the vertical etch rate by additional Cl on the substrate surface (Burton and Smolinsky 1982). This observation is consistent with Ti etching, as some of the etch rate lost with a decrease in pressure is regained with a Cl₂/O₂ plasma combination. Applying this knowledge, up to 4 sccm O₂ can be added to the TI DRIE process to enhance vertical etching.

The final aspect to consider is the Cl₂/Ar gas composition. Parker *et al.* reports no significant increase in etch rate, but an increase in sidewall roughness for values of Cl₂ above 40 sccm. At higher gas flow rates, there is less overall molecular dissociation due to the lower residence time of the incoming gas in the discharge (Danner and Hess 1986). Therefore, the steady etch rate and rough sidewall can be explained by an increase in the percentage of non-directional neutrals. These neutrally charged molecules or atoms collide with themselves, other gas species, or the substrate to increase isotropy. For the purposes of surface patterning of Ti, the Cl₂ content was decreased from 100 sccm until the positive effect of smoother sidewalls waned. This occurred below 40 sccm Cl₂.

Argon is an inert gas and is often added to stabilize the plasma or control etchant concentration (Muthukrishnan *et al.* 1997). Small additions (5 sccm) of Ar, though, can

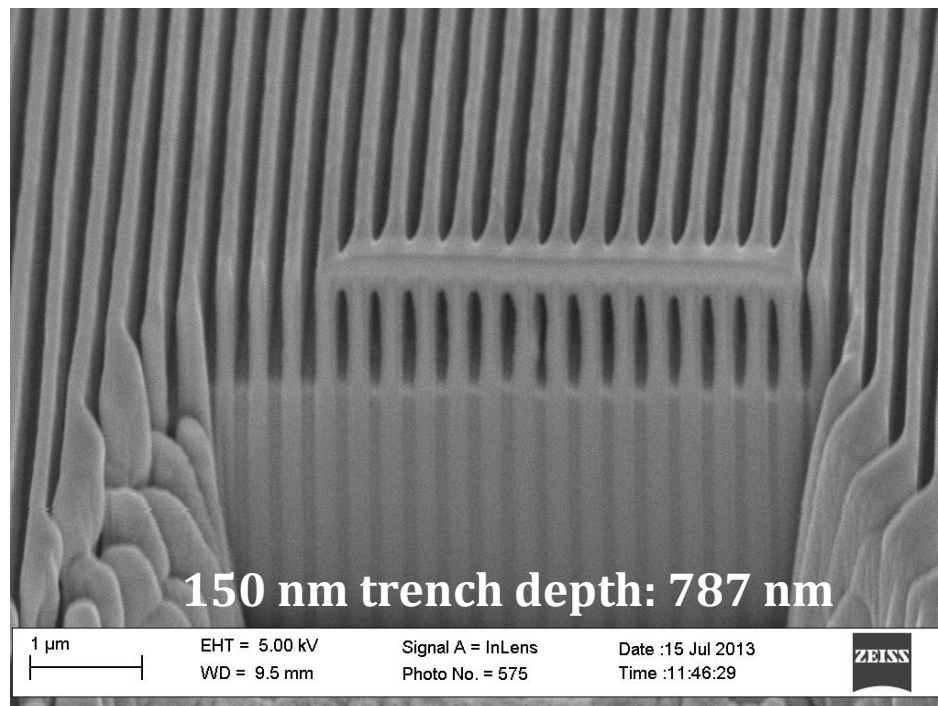


Figure 2-1. FIB cross-section of 150 nm gratings. Platinum deposited.

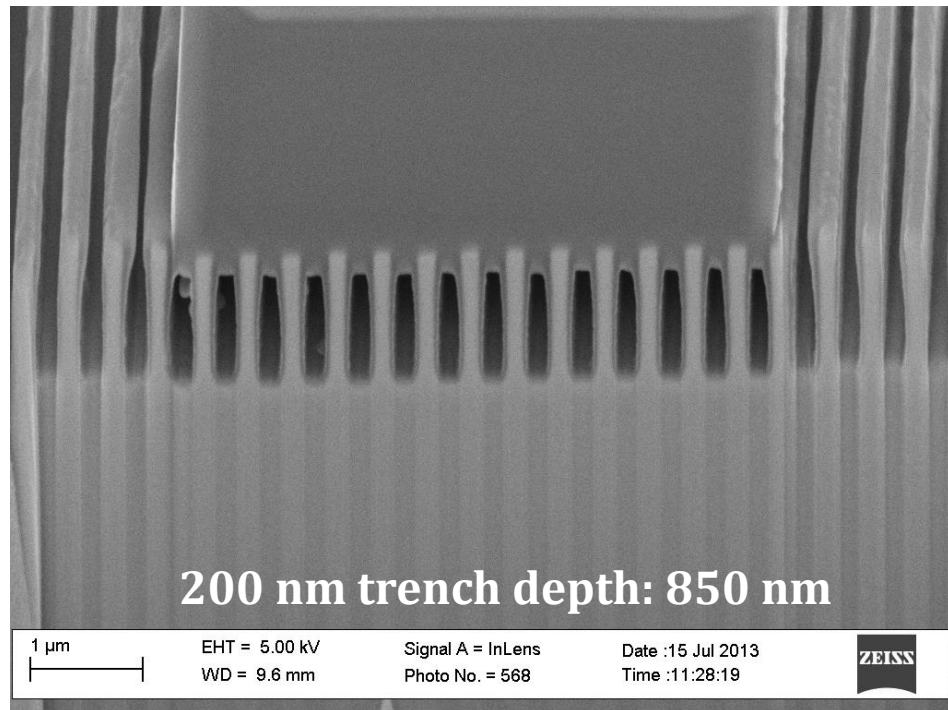


Figure 2-2. FIB cross-section of 200 nm gratings. Carbon deposited.

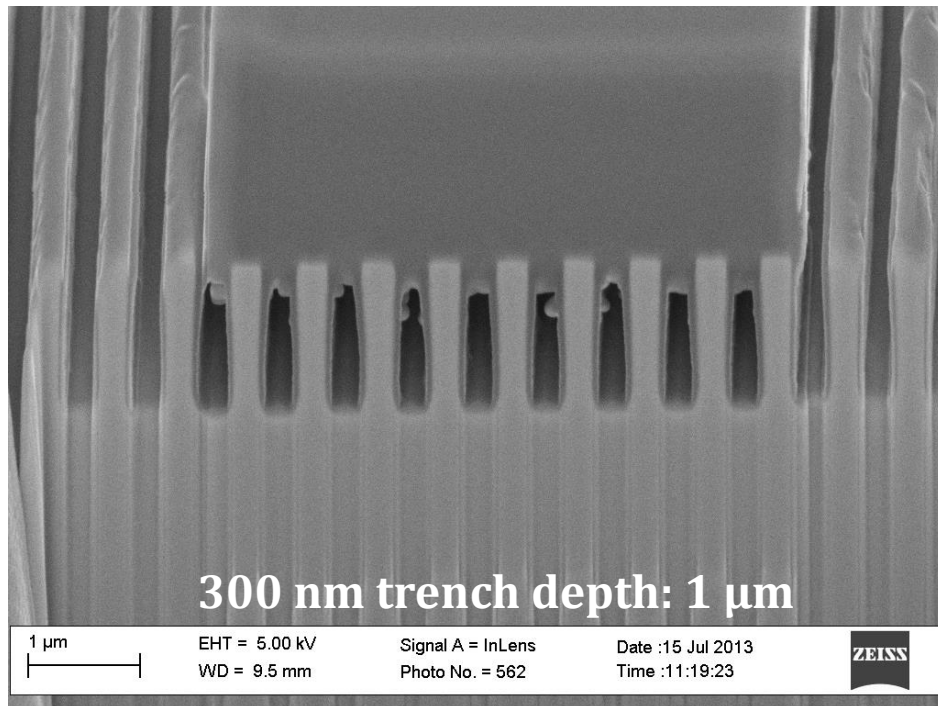


Figure 2-3. FIB cross-section of 300 nm gratings. Carbon deposited.

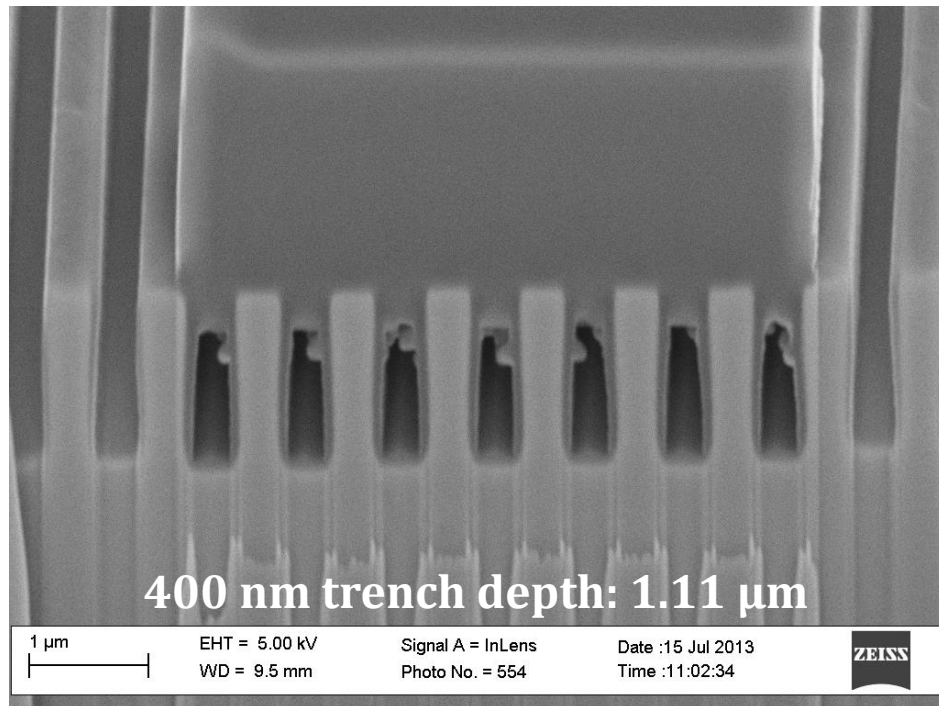


Figure 2-4. FIB cross-section of 400 nm gratings. Carbon deposited.

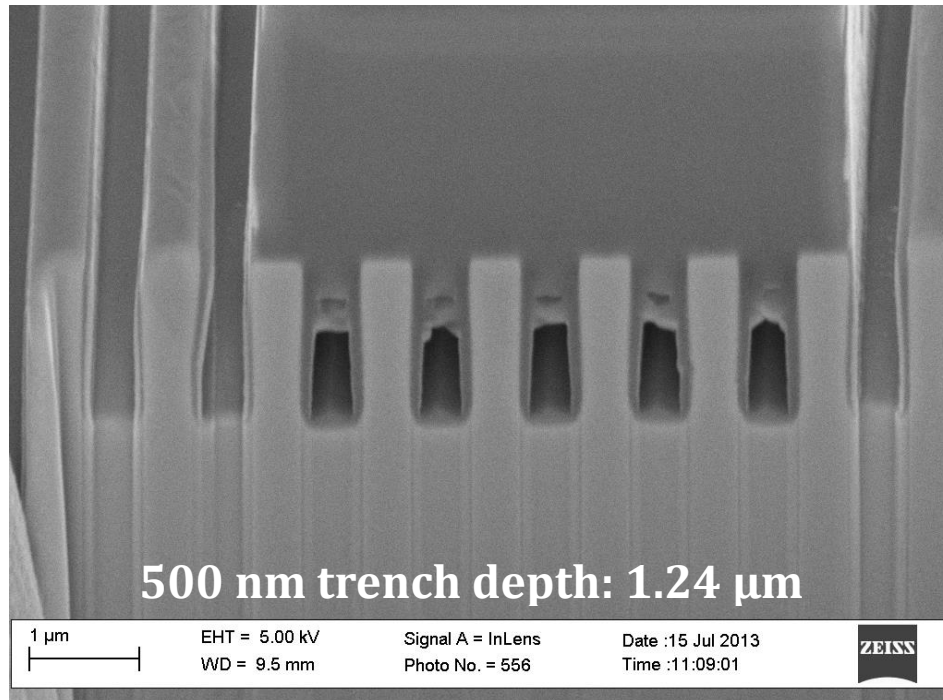


Figure 2-5. FIB cross-section of 500 nm gratings. Carbon deposited.

Feature Size (μm)	Etch Rate (μm/min)
50 – 0.5	1
0.4	0.83
0.3	0.75
0.2	0.64
0.15	0.59

Table 2- 1. Ti surface pattern size dependent etch rate.

lead to lateral etching with significant undercutting of the hard mask, as observed by Parker *et al.* (Parker *et al.* 2005). For this reason, Ar is omitted from the Ti surface pattern recipe.

Summarizing the improved etching recipe for sub-micron scale Ti surface patterning yields: 40 sccm Cl₂, 4 sccm O₂, 3.75 mTorr, 400 W ICP source, and 100 W sample RF power. Using FIB, a representative lot of our smallest Ti features etched with this recipe were cross-sectioned to view the profile and measure the depth with SEM (Figures 2-1 through 2-5). The etch rate is constant for 50 – 0.5 μm, but decreases gradually as the feature aspect ratio increases with smaller sizes (Table 2-1). This is most likely due to the ion scattering and collisions that are heightened with higher aspect ratios. Mask selectivity is ~ 30:1 (Ti:SiO₂), but due to the high incidence of ion scattering at the mask edge, there is increased mask recession, requiring a thicker mask.

2.7. Pattern Characterization

2.7.1. Scanning Electron Microscope

A scanning electron microscope (SEM) uses a beam of accelerated electrons to investigate or scan a surface of interest. When the beam hits a surface, electrons lose energy and signals from elastic scattering, inelastic scattering, and electromagnetic radiation are produced that can give information about the surface topography. Detection of the inelastic electron scattering, i.e. secondary electrons, is the most common imaging technique and is based on the angle at which the electrons strike the surface and rebound into the detector. At higher angles of incidence, more secondary electrons enter the

detector, which translates into a brighter signal and results in a 3D-like representation of the scanned surface. Since wavelengths of electrons and of visible light photons are $\sim 10^{-12}$ m and $\sim (4 - 7) \times 10^{-7}$ m, respectively (Halliday *et al.* 2006), a much higher resolution is achieved from an electron microscope than traditional optical microscopy. Hence, this is a vital tool in the investigation of sub-micron features.

2.7.2. Focused Ion Beam

In a system very similar to an SEM, a focused ion beam (FIB) images, sputters, or mills using a focused beam of ions. The ion source, typically gallium, is ionized by an electric field and accelerated toward a substrate by electrostatic lenses (Madou 2002). At lower beam currents, the ions that hit the surface generate secondary electrons that are detected and produce an image similar to an SEM; while higher beam currents are used for removal of substrate materials. Because, however, the FIB uses an ion beam for image generation, an SEM is still desired for characterization of samples that may be damaged by the ion bombardment.

For this work, the FIB was used in conjunction with SEM to investigate the profiles and depth of our sub-micron surface patterning. Unlike Si, which is a brittle material and can easily be cleaved to reveal feature profiles, Ti is ductile and must be precisely sectioned in a way that preserves the fidelity of the features. Focused ion beam milling provides this capability. To protect the surface of the features during FIB milling, FIB-assisted chemical vapor deposition can locally deposit a sacrificial layer over the site of interest and, depending on the size of the feature gaps, fill those as well. It was found

that carbon is the best material to use as a sacrificial layer because of the greater contrast it gives compared to the Ti in subsequent SEM imaging. This effect is most likely due to the two orders of magnitude difference in electrical resistivity of the two materials as compared to platinum, another popular sacrificial material (i.e. carbon as graphite: 0.006 ohm-cm; Ti: 0.0000554 ohm-cm; Platinum: 0.0000106 ohm-cm (MatWeb.com 2014)). Once protected, a cross section of the features of interest is milled to a smooth face and viewed under SEM. Representative views of our smallest feature sizes can be found in the Appendix G.

2.7.3. Atomic Force Microscopy

An atomic force microscope (AFM) consists of a cantilever with a sharp downward-facing tip that is used to scan a surface and gather image and measurement data beyond the nanoscale. The resolution of the tool is vertically constrained by the movement of the scanner and is typically sub-Angstrom while lateral resolution is a function of the radius of the probe tip and the overall shape of the object being measured as compared to that tip (Oliver 2008). As the tip is scanned across the surface it deflects the cantilever. A laser beam reflected off the cantilever captures deflections, which are directly proportional to the force on the tip. From this, information about the surface topography can be known. In this work, an AFM was used to determine substrate surface roughness in both pre- and post-processing phases.

3 CREATION AND EVALUATION OF SURFACE PATTERNING ON PLANAR TITANIUM

3.1. Introduction

It is now well-known that modulation of substrate topography within the micro- to nanoscale regime can profoundly influence cell-substrate interactions (Anselme and Biggerelle 2011; Bettinger *et al.* 2009; Biggs *et al.* 2010; Dvir *et al.* 2011; Sprague *et al.* 2012; Tay *et al.* 2011; Variola *et al.* 2011; Ventre *et al.* 2012; Wheeldon *et al.* 2011). Moreover, it is also well-known that surfaces with precisely-defined periodic topographies (hereafter referred to as “patterned” surfaces) can exert stronger influence than randomly-structured surfaces of comparable morphological length scales (e.g., surfaces with stochastic nanoscale roughness produced by acid etching, thin-film deposition, cold nanoparticle compaction, etc.) (Anselme and Biggerelle 2011; Bettinger *et al.* 2009; Biggs *et al.* 2010; Tay *et al.* 2011). Finally, it is becoming increasingly clear that anisotropically patterned surfaces (e.g., groove based gratings) afford opportunity for inducing desirable cellular responses (e.g., elongation and alignment) that are not possible with more isotropic surface patterns (e.g., hole or post arrays) (Anselme and Biggerelle 2011; Bettinger *et al.* 2009; Biggs *et al.* 2010; Tay *et al.* 2011). Consequently, this suggests that micro- to nanoscale anisotropic patterning may eventually provide a powerful new means for modulating cellular response to implantable devices.

One area of particular interest in this regard has been the modulation of endothelial cell (EC) response to polymeric vascular graft materials, where the ultimate goal has been to facilitate endothelialization over the graft surface and minimize cellular detachment. A number of recent *in vitro* studies have demonstrated that patterning of such materials with micrometer to sub-micrometer scale gratings can favorably affect EC responses such as

adhesion, proliferation, and morphology, among others (Barbucci *et al.* 2003; Bettinger *et al.* 2006; Bettinger *et al.* 2008; Biela *et al.* 2009; Brown *et al.* 2011; Di Rienzo *et al.* 2013; Franco *et al.* 2011; Gasiorowski *et al.*; Hwang *et al.* 2010; Jiang *et al.* 2002; Liliensiek *et al.* 2010; Morgan *et al.* 2012; Song *et al.* 2011; Uttayarat *et al.* 2008; Uttayarat *et al.* 2005; Zorlutuna *et al.* 2009). This, therefore, suggests promise for enhancing endothelialization *in vivo*. However, understanding of EC response to other patterned materials, such as Ti and Si, is limited. This represents an important knowledge gap, since patterning may provide means for enhancing the performance of other novel implantable microdevices based upon these materials (e.g., Ti-based pro-healing vascular stents (Gott *et al.* 2012), or Si₂ based wirelessly-controlled implantable drug delivery microchips (Farra *et al.* 2012)).

Herein, we begin to address this knowledge gap through the study of *in vitro* EC response on Ti and Si substrates with identically-patterned surfaces composed of groove-based gratings with groove widths ranging from 0.5 to 50 μm , grating pitch twice the groove width, and groove depth of 1.3 μm . Fabrication of these precisely defined patterned surfaces is enabled by both conventional Si micromachining techniques, as well as our novel Ti DRIE process (Aimi *et al.* 2004; Parker *et al.* 2005), which provides opportunity for machining of Ti at length scales well beneath that which is possible with other techniques (e.g., laser micromachining, microelectrodischarge machining, ultraprecision CNC, etc.). Using EA926 cells, a human EC variant, we show that cellular responses such as adhesion, proliferation, morphology, and athero-protective signaling are enhanced with decreasing pattern feature size for both materials; however, the magnitude of these responses is considerably larger on patterned Ti relative to comparably-patterned

Si. Collectively, these results suggest promise for sub-micrometer patterning as a new means for enhancing endothelialization and neovascularization for implantable microdevice applications.

3.2. Materials and Methods

3.2.1. Patterned Substrate Design

Figure 3-1 schematically illustrates the layouts of the patterned Ti and Si substrates used in this study, both of which share identical dimensions and patterning. One of the sub-patterns in each substrate is left unpatterned as a control, while the remainder are surface gratings consisting of periodic groove arrays with groove widths ranging from 0.5 to 50 μm , and grating pitch equal to twice the groove width (i.e., 1 grating pitch = groove width + ridge width). Each grating sub-pattern is orthogonally-oriented with respect to its neighbors, and is surrounded by a 100 μm wide unpatterned border (thus yielding 200 μm total width of unpatterned region between neighboring sub-patterns). Use of this substrate layout provides opportunity for simultaneous evaluation of a broad feature size range within the same substrate, and therefore, within the same cell culture conditions. In the current study, attention was focused specifically on the 0.5 μm , 0.75 μm , 50 μm , and unpatterned sub-patterns of each substrate.

3.2.2. Patterned Substrate Fabrication

Figure 3-2 outlines the fabrication processes for the patterned Ti and Si substrates. In both cases, polished substrates were first subjected to a standard solvent cleaning

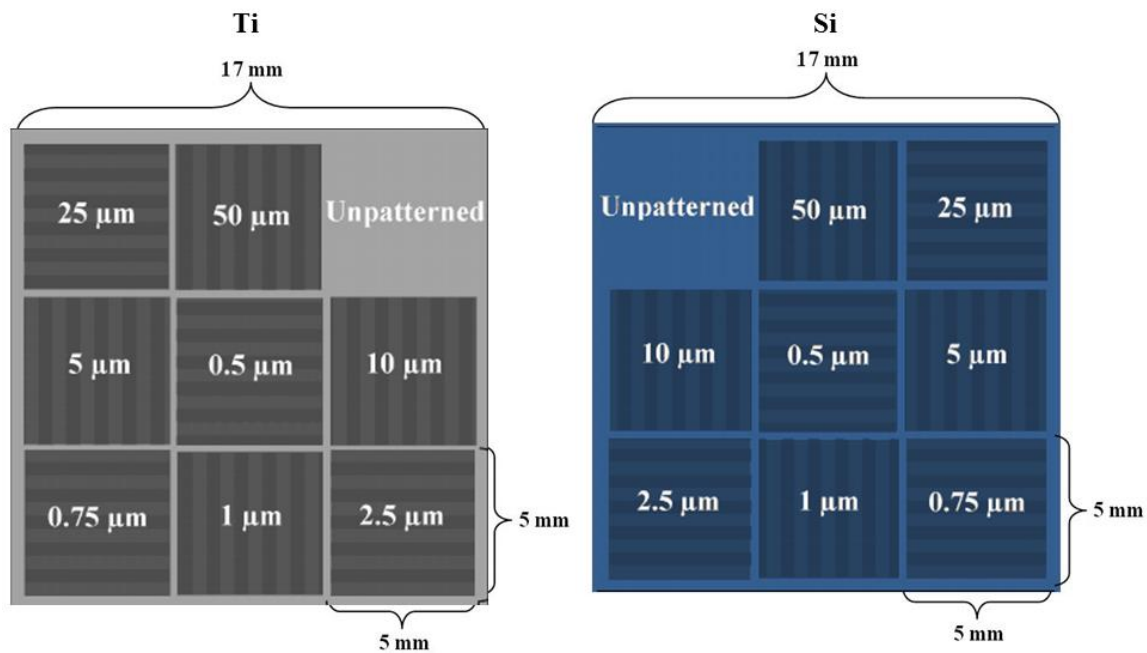


Figure 3-1. Schematics of the patterned Ti (left) and Si (right) substrates used in the current study. Each substrate is composed of an array of nine sub-patterns, one of which is left unpatterned to serve as a control, and the other eight of which consist of groove-based gratings with groove widths indicated in the schematic.

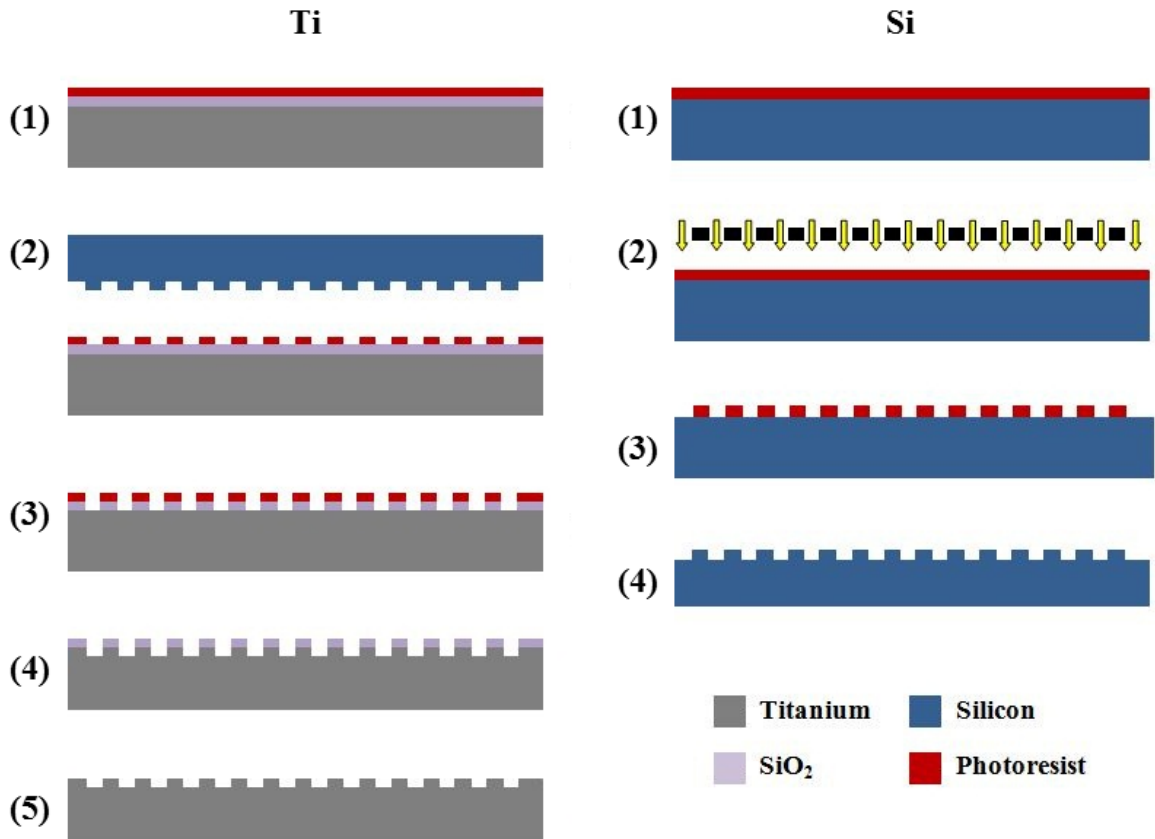


Figure 3-2. Fabrication processes for the patterned Ti (left) and Si (right) substrates. Patterned Ti substrate fabrication: 1) SiO₂ deposition by PECVD, followed by PR application; 2) Lithographic patterning via thermal NIL with patterned Si imprint master; 3) Pattern transfer to SiO₂ by F-based dry etching; 4) PR removal and Ti DRIE etch; and 5) Final SiO₂ removal by F-based dry etching. Patterned Si substrate fabrication: 1) PR application; 2) Lithographic exposure via projection lithography; 3) PR development and O₂ plasma descum; and 4) F-based dry etching and PR removal.

procedure consisting of sequential sonication in acetone and isopropanol, followed by rinsing in deionized (DI) water, and drying with N₂ gas.

For the patterned Ti substrate fabrication, polycrystalline, Grade 1, commercially-pure Ti substrates were used (99.6% Ti, 200 μm thickness; Tokyo Stainless Grinding). Following cleaning, an etch mask of 200 nm SiO₂ was deposited using PECVD (VLR, Unaxis). Photoresist was then applied by spin-coating (mr-I 7020, Micro Resist Technology). Afterwards, the PR was patterned using a Si imprint master and thermal NIL (NX2000, Nanonex). Oxygen-based dry etching was used to remove the residual PR layer at the base of the features after imprinting (E620-R&D, Panasonic Factory Solutions). This was followed by transfer of the PR patterns into the underlying SiO₂ etch mask by fluorine-based dry etching (E620-R&D). The mask patterns were then transferred to a depth of 1.3 μm into the underlying substrate using the modified version of the Ti DRIE process for nanoscale features. Finally, fluorine-based dry etching was used to remove the remaining etch mask.

For the patterned Si substrate fabrication, single crystal wafers were used (100 mm diameter, P/B doping, <1-0-0>, and 525±25 μm thickness; Silicon Quest International). Following cleaning, the wafers were dipped in buffered hydrofluoric acid, rinsed with DI, dried with N₂, and dehydration baked. The wafers were then primed with hexamethyldisilazane (HMDS), followed by PR spin-coating (AZ nLOF 5510, Clariant). After lithographic patterning using projection lithography (GCA Autostep 200 i-line Wafer Stepper, 3C Technical), the substrates were subjected to brief descuming by O₂ plasma (PE-IIA, Technics) to ensure complete removal of PR residues that may remain at

the base of the features after developing. The PR patterns were then transferred into the underlying Si substrate using fluorine-based dry etching (Plasmatherm SLR 770, Unaxis). Using this process, patterned Si substrates were produced for two purposes: 1) Substrates with grating depths of 1.3 μm were used for cell studies; and 2) Substrates with grating depths of 0.25 μm served as imprint masters in the fabrication of the patterned Ti substrates. For the latter, a coating of perfluorodecyltricholorsilane (FDTS) was applied using molecular vapor deposition (MVD 100E, Applied Microstructures) to minimize resist adhesion during imprinting.

3.2.3. Patterned Substrate Characterization

The fidelity and uniformity of the substrate patterning was characterized using SEM (SUPRA 55, Leo). Imaging was performed at 5 Kv accelerating voltage without need for application of conductive coatings on either substrate. Mean groove width, ridge width, and grating pitch for each sub-pattern were calculated based on measurements made at five different locations within each sub-pattern (i.e., center and four corners).

The depths of the larger gratings of both substrates were corroborated using a surface profilometer with 12 μm tip diameter stylus (Dektak 8, Veeco Metrology Group). The groove depths and profiles in the patterned substrates were characterized via cross sectioning and SEM imaging. Focused ion beam (FIB) milling was used to cross section the Ti substrates (CrossBeam XB1540, Carl Zeiss Microscopy), while cleaving was used to cross section the Si substrates. The depths of the larger gratings of both substrates were

corroborated using a surface profilometer with 12 μm tip diameter stylus (Dektak 8, Veeco Metrology Group).

The surface roughness of the patterned substrates was characterized using AFM (Dimension 3100, Nanoscope IIIa, Veeco Metrology Group). Commercially available Si nitride tips were used (tip radius of curvature < 10 nm, tip height = 14 – 16 μm , and spring constant = 1.2 – 6.4 $\text{N}\cdot\text{m}^{-1}$; Bruker AFM Probes). Imaging was performed in tapping mode with 1 Hz scan rate. Measurements were made within the middle of the ridge-tops for all gratings, well away from the ridge edges. For the 0.5 and 0.75 μm gratings, measurements were made over 0.20 μm x 0.20 μm areas (i.e., 0.04 μm^2 measurement area). For the 50 μm gratings and unpatterned sub-patterns, measurements were made over 0.53 μm x 0.53 μm areas (i.e., 0.28 μm^2 measurement area). Average roughness, root mean square roughness, and maximum roughness values for each sub-pattern were calculated based on measurements made at five different locations within each sub-pattern (i.e., center and four corners).

3.2.4. Endothelial Cell Culture

EA926 cells, a HEC variant, were obtained from ATCC (Manassas, VA). Cells were cultured using Dulbecco's modified Eagle's medium (DMEM, Lonza) and were supplemented with 10% FBS (Gibco) and antibiotics (Primocin, Invivogen). Freshly passaged cells were maintained in a humidified air incubator (5% CO_2 , 37°C).

3.2.5. Endothelial Cell Assays

Prior to all assays, the patterned substrates were subjected to standard solvent cleaning, followed by sterilization by autoclaving (121 °C for 35 min) and overnight UV exposure. Trypsinized HECs were seeded at a density of 22,000 cells/cm² on the patterned substrates and cultured for various durations (4 h, 1 d, 3 d, and 5 d), after which non-adherent cells were removed by rinsing twice in phosphate buffered solution (PBS). Cells that remained on the surface were visualized by fluorescent staining of nuclei to evaluate adhesion and proliferation response (Hoechst 33342, Life Technologies®), or the cellular membrane to evaluate substrate coverage (Rhodamine 123, Life Technologies®). Live/dead assays were also performed on surface-adhered cells using propidium iodide and 4',6-diamidino-2-phenylindole (Life Technologies®). Mean cell densities for each sub-pattern were calculated based on measurements made at five different locations within each sub-pattern (i.e., center and four corners).

3.2.6. Immunostaining

Endothelial cell morphology and cytoskeletal architecture were evaluated using immunostaining. After prescribed culture durations, non-adherent HECs were removed by PBS rinsing. Remaining HECs on the patterned substrates were fixed with 4% paraformaldehyde for 15 min, permeabilized with 0.2% Triton X-100 and 1 mg/ml BSA for 10 min, rinsed with PBS, and stained for 10 min with Alexa Fluor® 488 phalloidin (Life Technologies®) for F-actin, and Hoechst 33342 (Life Technologies®) for nuclei. The elongation and orientation of HECs on the patterned substrates were determined based on

measurements made on immunostained cells after 5 d culture. Using ImageJ[®], elongation was calculated as the ratio of major to minor cell axis lengths (as defined by the actin microfilament network), while orientation was characterized as the angular deviation between the cell major axis and the grating axis. Angular deviation for HECs on the unpatterned sub-patterns was determined relative to an arbitrary reference axis whose orientation was held fixed for each field of view the measurements were made over. Means were calculated based on measurements made at five different locations within each sub-pattern (i.e., center and four corners).

For phenotype and function studies, the expression of two EC markers, von Willebrand Factor (vWF) and vascular cell adhesion molecule-1 (VCAM-1), was characterized. vWF maintains homeostasis through binding to FVIII, platelet surface glycoproteins, and constituents of connective tissue. It also initiates platelet aggregation via binding to exposed structures of injured vessel walls at high arterial shear rates. Furthermore, it is thought to assist during platelet aggregation by bridging adjacent platelets at high shear rates. The function of vWF is strongly shear rate dependent, whereas fluid dynamic conditions, as well as mechanical forces, are crucial for the conformational transition of VWF to develop its interaction with endothelial matrix proteins, as well as platelets, in case of vessel injury (Mitsumata *et al.* 1993; Nerem *et al.* 1993). Essentially, vWF is considered an anti-thrombotic biomarker (Sakariassen *et al.* 1979). VCAM-1 plays an important role in both immune responses and in recruitment of lymphocytes, monocytes, leukocyte adhesion to sites of inflammation (OBrien *et al.* 1996). It appears to function as a leukocyte-endothelial cell migration molecule (Nagel *et*

al. 1994). Because of this, VCAM-1 is recognized as a significant biomarker of endothelial dysfunction (Davies *et al.* 1993; Hwang *et al.* 1997).

HECs were seeded at a density of 50,000 cells/cm² and cultured for 1 day. Substrates were then washed with PBS and adherent HECs were fixed and permeabilized in -20 °C methanol for 20 min. Substrates were then washed in PBS, incubated with blocking buffer (4 g BSA + 80 mL PBS + 150 µL Triton X 100) for 1 h, and incubated with 1:400 of rabbit polyclonal anti-vWF/VCAM-1 in antibody dilution buffer (4 g BSA + 40 mL PBS + 120 µL Triton X 100) overnight at 4 °C. Substrates were then rinsed in PBS and incubated with 1:1000 Texas Red[®] 598 donkey anti-rabbit secondary antibody for 1 h at 25 °C. Finally, nuclei were cross-stained using Hoechst 33342. Using ImageJ[®], protein expression per cell area was quantified by measuring the average fluorescence signal intensity within a cell and dividing this value by the area of the cell. Means were calculated based on measurements made on at least 10 cells per sub-pattern.

3.2.7. Fluorescent Imaging

Fluorescent imaging of HECs on the patterned substrates was performed using a fully apochromatic corrected stereomicroscope with 12.5:1 zoom (M125, Leica). Images were acquired with a 10X objective lens, binning of 4 x 4, gain of 8.0, and brightness of 1.2 was used for image acquisition. Stained cells were imaged using a Leica SP5 confocal microscope. Spot Imaging Software[®] and Leica SP5 LAS Software[®] were used for image acquisition, and images were processed using ImageJ[®] (v1.46, NIH).

3.2.8. Scanning Electron Microscopy of Cell-seeded Substrates

SEM imaging of HECs on the patterned substrates was also performed. Prior to imaging, cells were washed with PBS, fixed with 4% glutaraldehyde, and post-fixed with 0.5% OsO₄ for 1 h each. They were then dehydrated through a graded series of alcohols and dried in a critical point dryer (CPD 030, Balzer). Imaging was performed at 5 kV accelerating voltage without need for conductive coatings on either substrate type.

3.2.9. Cellular Morphology Quantification

The elongation and orientation of HECs on the patterned substrates were determined based on measurements made on immunostained cells after 5 d culture. Using ImageJ[®], elongation was calculated as the ratio of major to minor cell axis lengths, while orientation was characterized as the angular deviation between the cell major axis and the grating axis. Angular deviation for HECs on the unpatterned sub-patterns was determined relative to an arbitrary reference axis whose orientation was held fixed for each field of view the measurements were made over. Means were calculated based on measurements made at five different locations within each sub-pattern (i.e., center and four corners).

3.2.10. Statistical Analyses

All cell studies were repeated in triplicate. Statistical analyses were performed using single-factor ANOVA and commercially-available software packages (Excel[®], Microsoft; and SigmaPlot[®] 5.0, Systat Software).

3.3. Results

3.3.1. Patterned Substrate Characterization

Figure 3-3 shows representative SEM micrographs of the patterned Ti and Si substrates. Precisely defined and highly uniform patterning is observed on both substrates. This is further corroborated by the excellent agreement between the expected and measured grating groove widths, ridge widths, and pitches for each sub-pattern reported in Table 1. As discussed earlier, the Ti DRIE process is the only technique capable of producing such diminutive and precisely defined features within bulk Ti substrates.

Figure 3-4 shows cross section SEM micrographs of the 0.5 μm gratings on the patterned Ti and Si substrates. As can be seen, nearly identical gratings have been produced in both substrates. Moreover, groove profiles are observed to be nearly rectangular. Finally, identical groove depths of 1.3 μm are achieved for both substrates. Results from surface profilometry measurements of wider grooves elsewhere on the patterned substrates returned similar depths (data not shown), thus indicating a uniform groove depth across all sub-patterns on the Ti and Si substrates.

Table 2 reports AFM-based surface roughness measurements for the grating ridge-tops of the patterned Ti and Si substrates. Average roughness, R_a , represents the average height of the roughness irregularities, while root mean square roughness, R_{sq} , is more sensitive to low and high points, and maximum roughness, R_{max} , reports the largest aberrations. In all sub-patterns, R_a and R_{sq} are extremely small (i.e., ≤ 2 nm), thus suggesting that this should minimally influence cellular response.

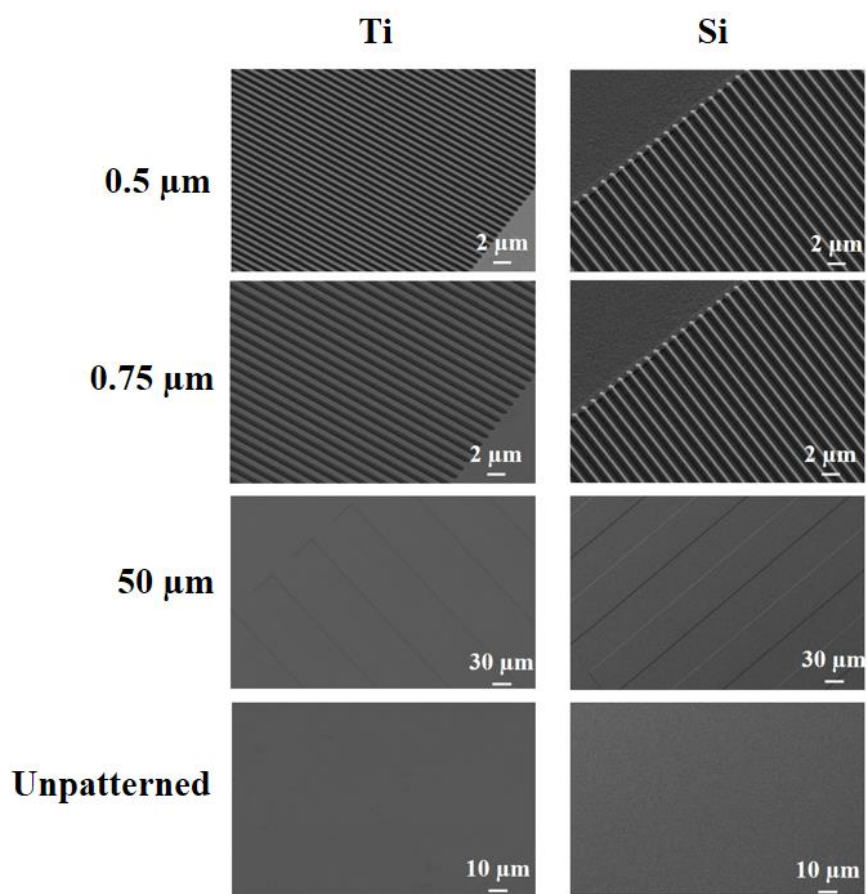


Figure 3-3. Scanning electron microscope micrographs of patterned Ti (left) and Si (right) substrates with 0.5 μm, 0.75 μm, and 50 μm gratings, as well as unpatterned control surfaces.

Feature Size	Ti			Si		
	0.5 μm	0.75 μm	50 μm	0.5 μm	0.75 μm	50 μm
Groove (μm)	0.498 \pm 0.003	0.748 \pm 0.000	50.0 \pm 0.0	0.501 \pm 0.002	0.747 \pm 0.000	50.0 \pm 0.0
Ridge (μm)	0.502 \pm 0.003	0.748 \pm 0.000	50.0 \pm 0.0	0.501 \pm 0.002	0.751 \pm 0.006	50.0 \pm 0.0
Pitch (μm)	1.000 \pm 0.000	1.500 \pm 0.004	100.0 \pm 0.0	1.000 \pm 0.001	1.510 \pm 0.000	100.0 \pm 0.1

Table 3-1. Scanning electron microscope measurements of sub-pattern feature dimensions on patterned Ti and Si substrates, including grating groove width, ridge width, and pitch (i.e. groove width + ridge width). Data = mean \pm standard deviation, n = 5.

Feature Size	Ti				Si			
	0.5 μm	0.75 μm	50 μm	unpatterned	0.5 μm	0.75 μm	50 μm	unpatterned
R_a (nm)	0.88 \pm 0.19	0.62 \pm 0.05	0.43 \pm 0.04	0.56 \pm 0.03	0.39 \pm 0.01	0.60 \pm 0.07	0.30 \pm 0.03	1.60 \pm 0.15
R_{sq} (nm)	1.15 \pm 0.18	0.77 \pm 0.28	0.56 \pm 0.05	0.74 \pm 0.06	0.52 \pm 0.01	0.91 \pm 0.22	0.40 \pm 0.07	2.01 \pm 0.19
R_{max} (nm)	10.48 \pm 4.23	5.06 \pm 0.41	7.89 \pm 2.19	7.05 \pm 1.08	5.30 \pm 1.58	11.56 \pm 2.38	5.21 \pm 1.63	14.23 \pm 1.27

Table 3-2. Atomic force microscope measurements of sub-pattern ridge-top surface roughness on patterned Ti and Si substrates, including average roughness (R_a), root mean square roughness (R_{sq}), and maximum roughness (R_{max}). Data = mean \pm standard deviation, n = 5.

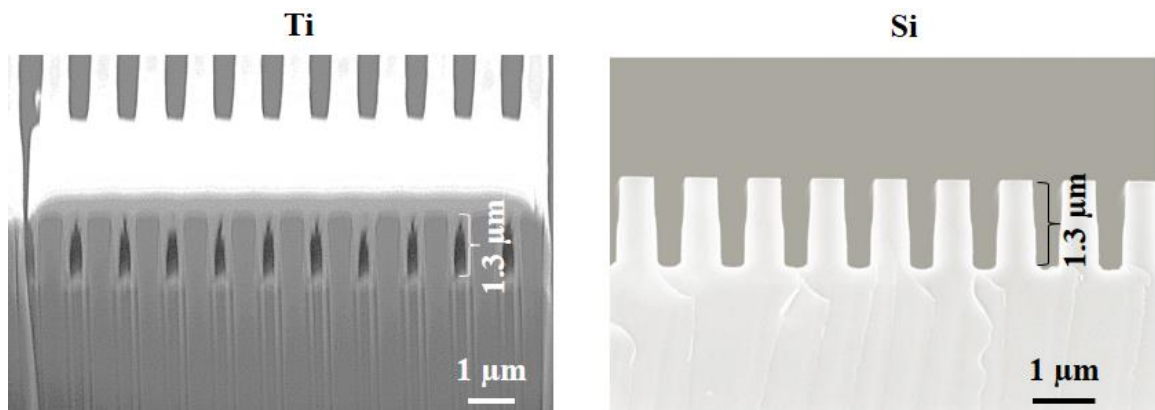


Figure 3-4. Scanning electron microscope micrographs of 0.5 μm grating sub-pattern cross sections from patterned Ti (left) and Si (right) substrates. The Ti grating was imaged in a tilted orientation, while the Si grating was imaged without tilt. The bright layer covering the upper foreground surface of the Ti grating is a Pt film deposited prior to focused ion beam milling. This film protected the underlying structures from sputtering-induced faceting during milling. The vertically-oriented contrast variations observed beneath the Ti grating are “curtain effect” artifacts produced by differential sputtering during milling.

3.3.2. Endothelial Cell Adhesion and Proliferation

Figure 3-5 shows HEC densities at various time points on the patterned Ti and Si substrates. At the 0 d time point (i.e. 30 min), we observe a trend of increasing adhesion with decreasing feature size on the patterned Ti substrates, and response on patterned Ti surfaces is generally greater than the unpatterned Ti control, e.g., HEC densities on the 0.5 μm Ti gratings are 2.32 times greater than unpatterned Ti. For the patterned Si substrates, similar size-dependent response is observed, e.g., HEC densities on the 0.5 μm Si gratings are 2 times greater than unpatterned Si. However, adhesion on patterned Si is generally lower than on comparably patterned Ti, e.g., HEC densities on the 0.5 μm Si gratings are 14 % lower than on 0.5 μm Ti gratings. Finally, adhesion on both patterned and unpatterned Ti and Si is greater than the tissue culture plastic control.

At latter time points (i.e., 1 d and onwards), Figure 3-5 shows that HEC proliferation increases with decreasing feature sizes on the patterned Ti substrates, and response on patterned Ti surfaces is greater than the unpatterned Ti control, e.g., at 5 d, HEC densities on the 0.5 μm Ti gratings are nearly 3 times greater than unpatterned Ti. A similar trend for the patterned Si substrates is also seen, e.g., at 5 d, HEC densities on the 0.5 μm Si gratings are 4.14 times greater than unpatterned Si. However, proliferation on patterned Si is generally lower than on patterned Ti at comparable time points and feature sizes, e.g., at 5 d, HEC densities on the 0.5 μm Si gratings are 28.26% lower than on the 0.5 μm Ti gratings. Finally, proliferation on patterned Ti and Si is generally greater than the tissue culture plastic control. For all time points and sub-patterns, live/dead assays

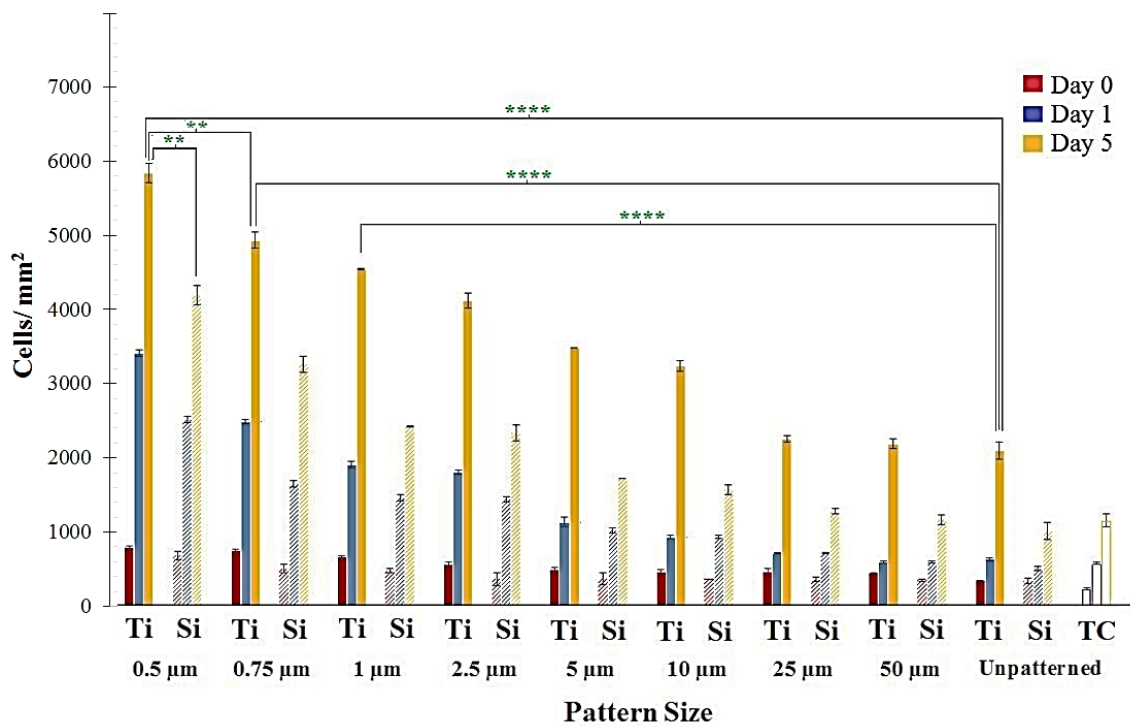


Figure 3-5. Human endothelial cell densities on patterned Ti and Si substrates and tissue culture plastic at varying time points ranging from 30 min (i.e. 0 days) to 5 days. Data = mean \pm SEM (**p = 0.01, ****p = 0.0001; unpaired samples T-test, n = 5).

indicate a maximum of 0.1% of dead cells on both Ti and Si substrates, thus confirming the viability of the adhered cells.

3.3.3. Endothelial Cell Morphology and Cytoskeletal Architecture

Figure 3-6 shows SEM micrographs of HECs on 0.5 μm gratings and unpatterned sub-patterns of both substrate materials after 1 d. Significant cellular elongation is observed on the Ti grating and alignment along the grating axis is clear. For the Si grating, significant cellular elongation is also seen, as is alignment with the grating axis. However, more favorable cellular morphology occurs on the Ti grating relative to the Si grating, as evidenced by greater flattening and spreading. Greater spreading is also seen on the unpatterned Ti relative to unpatterned Si surfaces.

Similar trends are observed at latter time points, as illustrated in Figure 3-7, which shows SEM micrographs of HECs on patterned Ti and Si substrates after 5 d. These images were taken at the boundary between the 0.5 μm and 50 μm sub-patterns, which are separated by a 200 μm wide unpatterned region, and are orthogonally oriented with respect to one another. Cellular elongation and alignment are again seen on the 0.5 μm gratings of both materials, with more favorable morphology and greater coverage on the 0.5 μm Ti grating. Moreover, the Ti micrograph clearly illustrates the spatial specificity of HEC response to the 0.5 μm Ti grating, as evidenced by the decreasing cell alignment and density with distance from the boundary of the 0.5 μm sub-pattern.

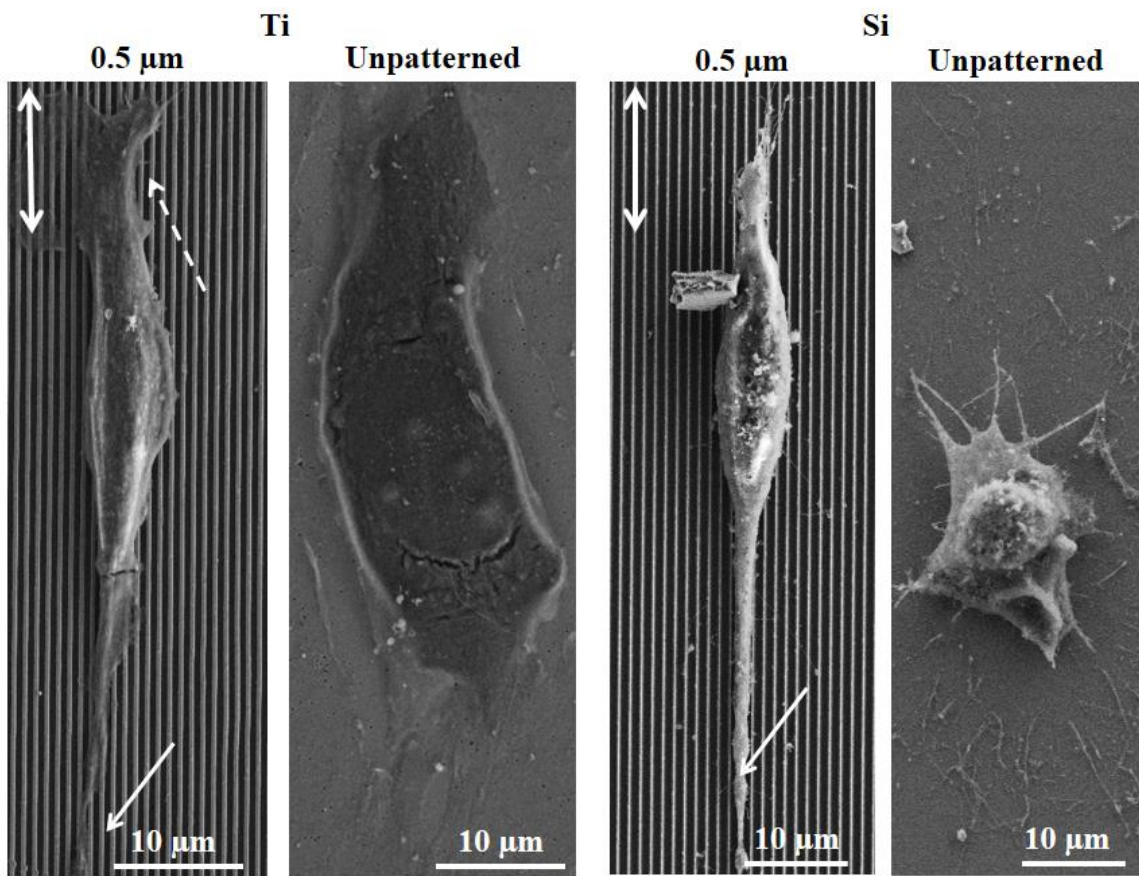


Figure 3-6. Scanning electron microscope micrographs of human endothelial cells after 1 day culture on 0.5 μm gratings and unpatterned sub-patterns of Ti (left) and Si (right) substrates. Arrows indicate filopodia and lamellopodia.

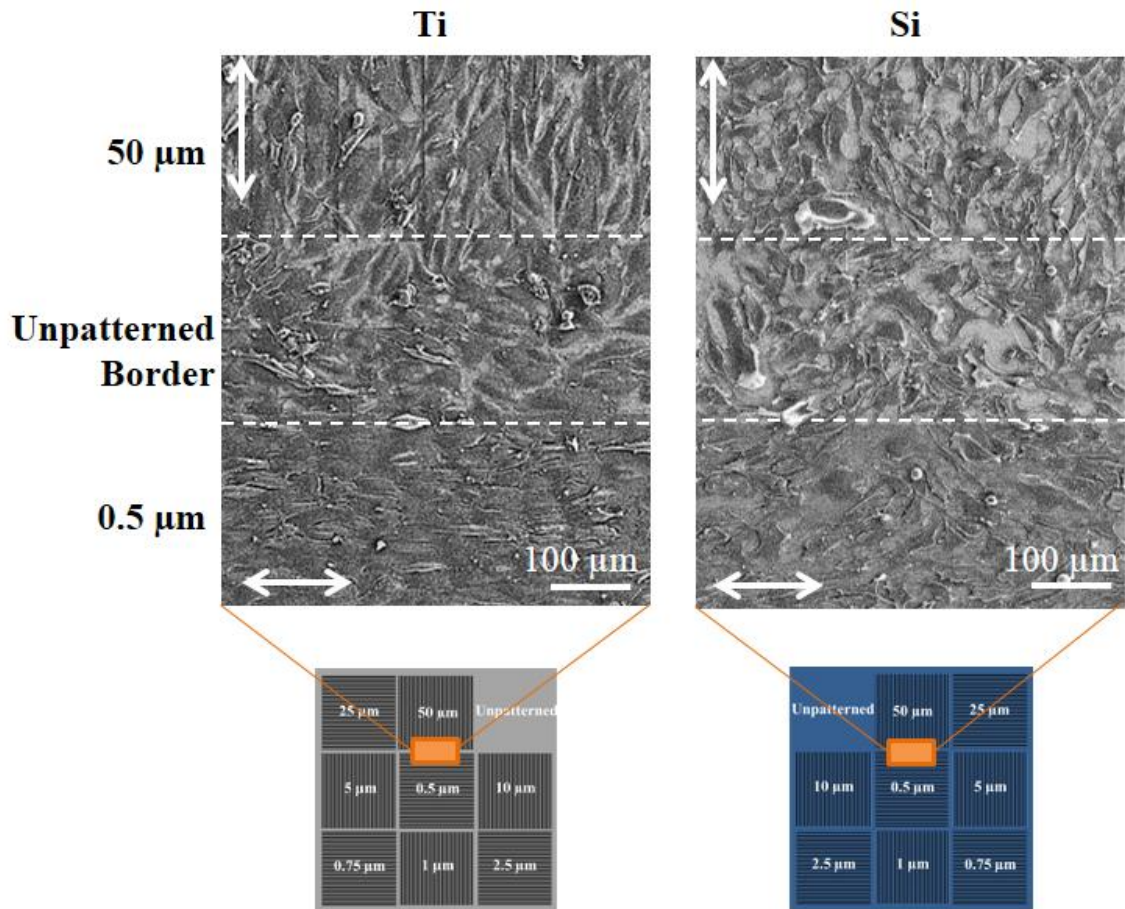


Figure 3-7. Scanning electron microscope micrographs of human endothelial cells after 5 day culture on patterned Ti (left) and Si (right) substrates. Each micrograph depicts a single field of view located at the boundary between the 0.5 μm and 50 μm grating sub-patterns, as illustrated in the schematics below the micrograph. Dotted lines indicate boundaries of the sub-patterns and double arrows indicate grating directions.

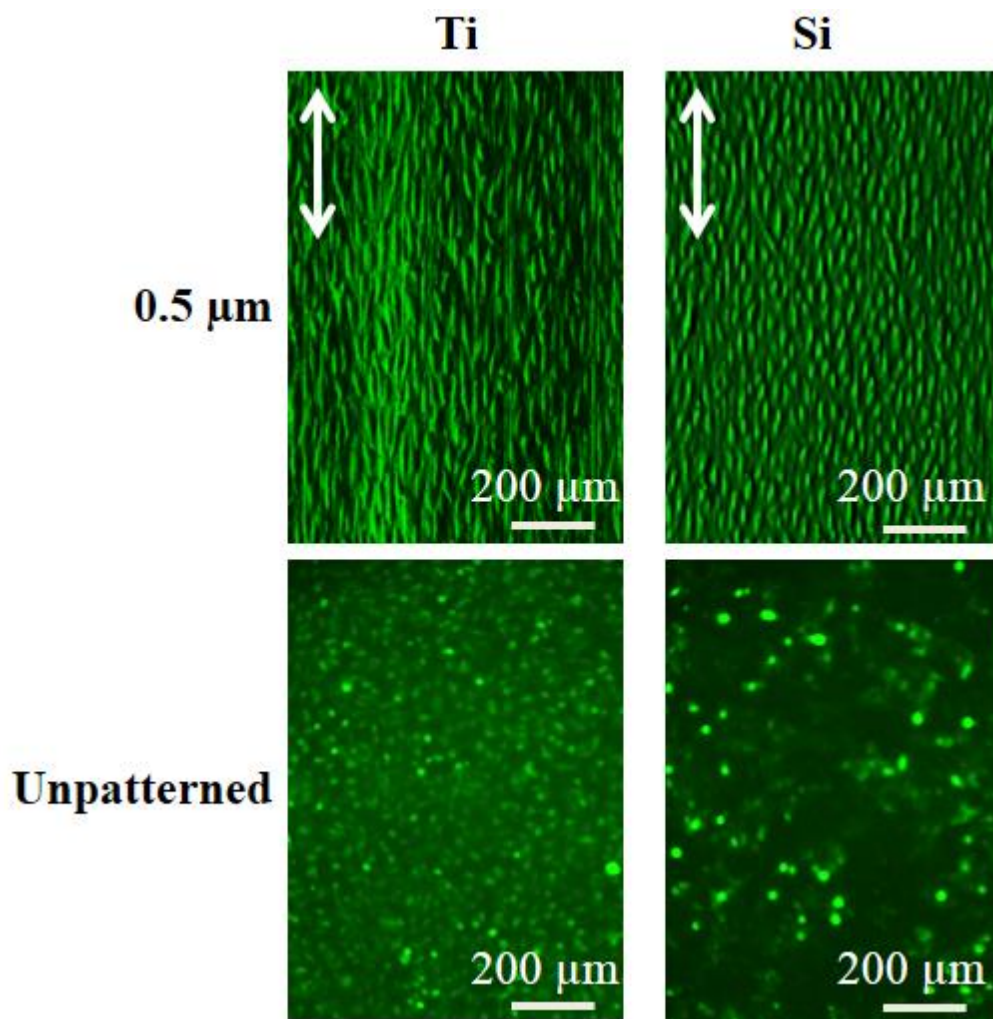


Figure 3-8. Fluorescent micrographs of human endothelial cells after 5 day culture on 0.5 μm gratings and unpatterned sub-patterns of Ti (left) and Si (right) substrates. Double arrows indicate grating direction.

Further evidence of the influence of sub-micrometer patterning and substrate material is provided by Figure 3-8, which shows fluorescence micrographs of HECs on 0.5 μm gratings and unpatterned sub-patterns of both substrate materials after 5 d. Strong elongation and alignment are observed on the Ti grating. Moreover, a nearly confluent HEC layer is observed on the Ti grating, while sparser coverage is seen on the unpatterned Ti. For the Si grating, increased elongation and alignment are also observed relative to the unpatterned Si control. However, HEC coverage on the Si grating is lower than the comparable Ti grating.

The influence of sub-micrometer patterning and substrate material on cytoskeletal architecture is illustrated in Figure 3-9, which shows HECs stained for nuclei and F-actin on 0.5 μm gratings and unpatterned sub-patterns of both substrate materials after 5 d. Strong cytoskeletal alignment is evident on the gratings of both materials, which is corroborated by the increasing cellular elongation ratios and decreasing angular deviations with decreasing feature size reported in Table 3. However, the microfilament network on the 0.5 μm Ti grating is observed to be more robust relative to the 0.5 μm Si grating, and greater elongation is seen on the Ti grating. Cytoskeletal alignment is not observed on the unpatterned controls for either substrate. This is further corroborated by the measured $\sim 45^\circ$ mean angular deviation on the unpatterned controls for either substrate, which is indicative of randomized cell orientation.

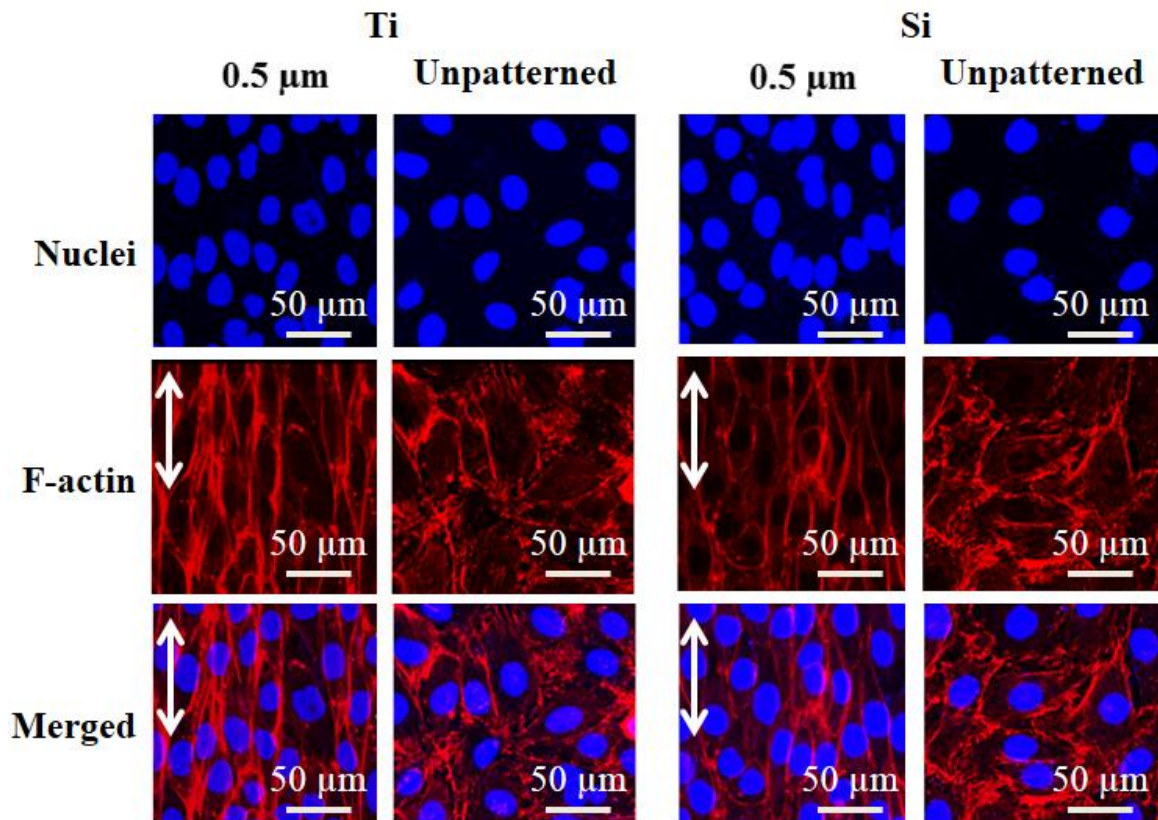


Figure 3-9. Confocal micrographs of human endothelial cells after 5 day culture on 0.5 μm gratings and unpatterned sub-patterns of Ti (left) and Si (right) substrates. Cells were immunostained using phalloidin (red) for cytoskeletal protein F-actin, and Hoechst 33342 (blue) for nuclei. Double arrows indicate grating direction.

	Ti				Si			
Feature Size	0.5 μm	0.75 μm	50 μm	unpatterned	0.5 μm	0.75 μm	50 μm	unpatterned
Elongation Ratio	5.62 \pm 1.23	4.79 \pm 0.93	3.49 \pm 0.88	2.89 \pm 0.85	3.52 \pm 0.60	2.03 \pm 0.34	2.37 \pm 0.79	2.87 \pm 0.82
Angular Deviation (degrees)	4.66 \pm 3.47	10.30 \pm 4.34	45.37 \pm 3.02	45.35 \pm 23.01	3.33 \pm 2.70	17.79 \pm 14.52	42.1 \pm 18.47	47.63 \pm 45.95

Table 3-3. Confocal microscopy measurements of human endothelial cell elongation ratio and angular deviation (from the grating axis) after 5 day culture on patterned Ti and Si substrates. Angular deviation on unpatterned sub-patterns was determined relative to an arbitrary reference axis that was held fixed for each field of view. Data = mean \pm standard deviation, n = 5.

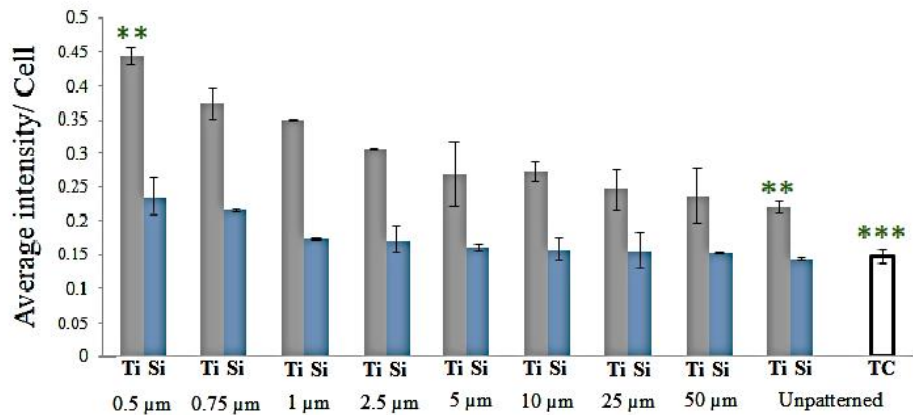
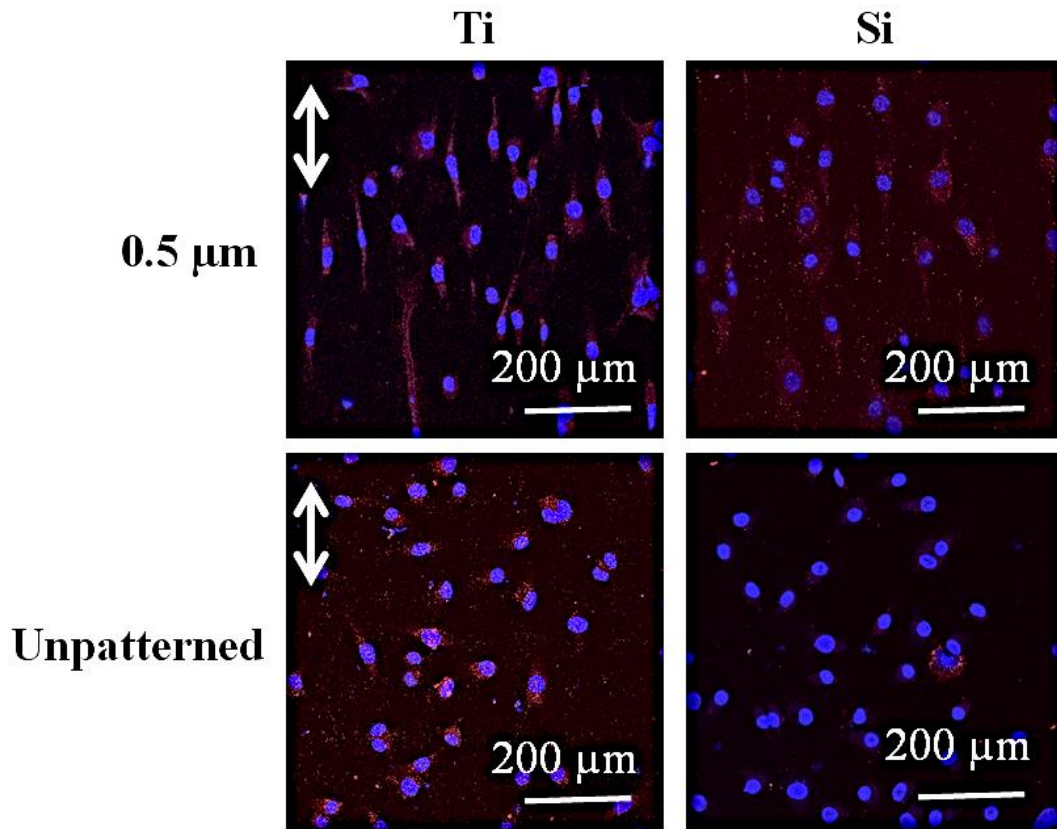


Figure 3-10a. Confocal micrographs and quantification of vWF expression (red), a human endothelial cell protein, after 1 day culture on 0.5 μm gratings and unpatterned sub-patterns of Ti and Si substrates, and tissue culture plastic. Nuclei (blue) were cross-stained using Hoechst 33342. Double arrows indicate grating direction. Data = mean \pm SEM (** $p = 0.01$, *** $p = 0.001$; unpaired samples T-test, $n = 10$).

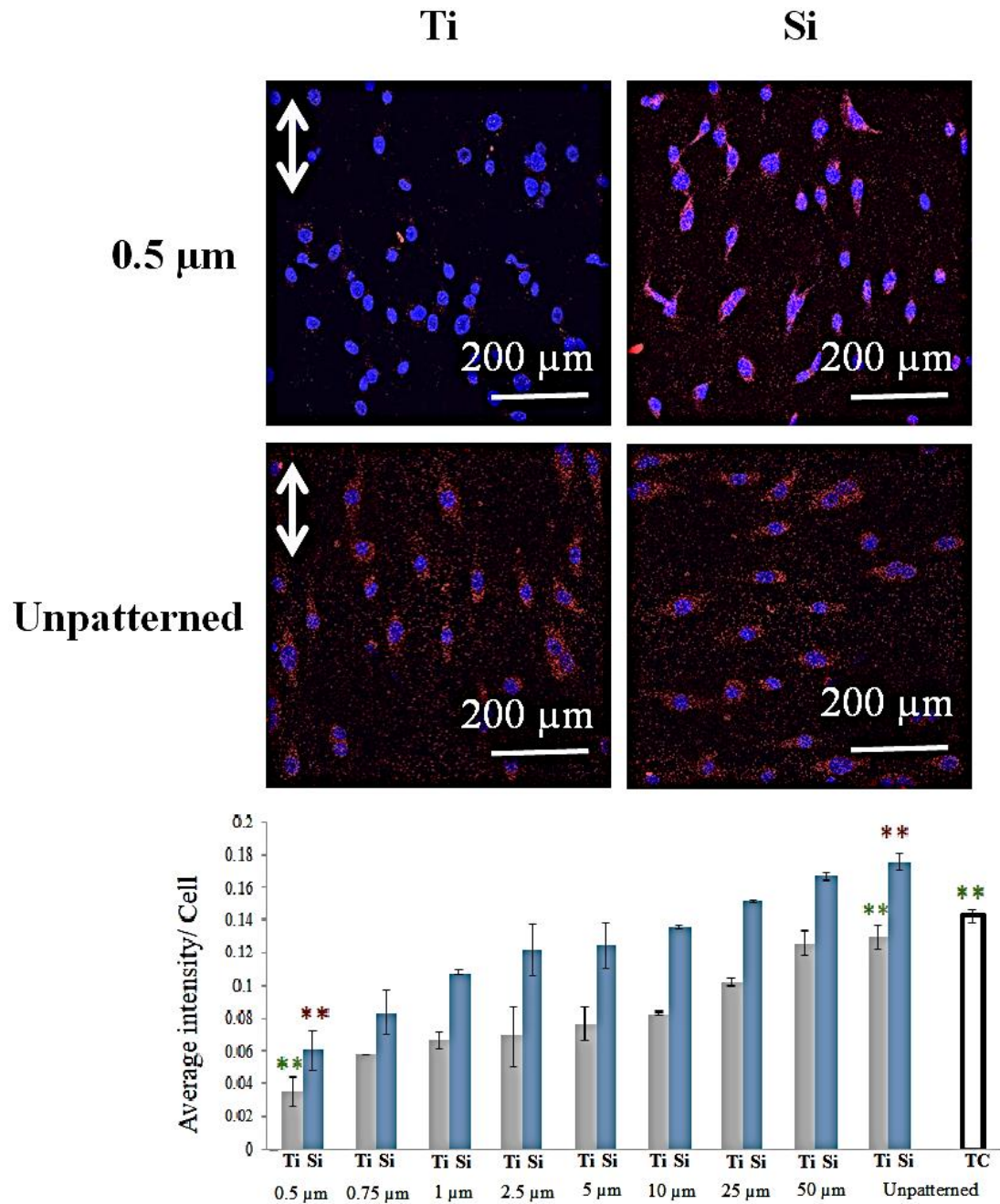


Figure 3-10b. Confocal micrographs and quantification of VCAM-1 expression (red), a human endothelial cell protein, after 1 day culture on 0.5 μm gratings and unpatterned sub-patterns of Ti and Si substrates, and tissue culture plastic. Nuclei (blue) were cross-stained using Hoechst 33342. Double arrows indicate grating direction. Data = mean ± SEM (**p = 0.01, ***p = 0.001; unpaired samples T-test, n = 10).

3.3.4. Endothelial Cell Function

Figures 3-10a and 3-10b show results for expression of two important EC markers, vWF and VCAM-1, on the patterned Ti and Si substrates. As discussed earlier, vWF is a functional marker expressed by ECs that plays a key role in homeostasis, whereas VCAM-1 is a marker for inflammation.

As shown in Figure 3-10a, vWF is uniformly distributed within the cytoplasm of HECs on the 0.5 μm gratings of both Ti and Si, but is more confined to the perinuclear regions on the unpatterned controls. Moreover, quantitative measurements show increasing expression with decreasing feature size on both Ti and Si patterned substrates, and response on the patterned surfaces is greater than their respective unpatterned controls, e.g., expression on the 0.5 μm Ti gratings is 2 times greater than unpatterned Ti. However, expression on patterned Si is considerably lower than on comparably patterned Ti, e.g., expression on the 0.5 μm Si gratings is 46 % lower than on 0.5 μm Ti gratings. Finally, expression on both patterned and unpatterned Ti and Si is generally greater than the tissue culture plastic control.

Figure 3-10b shows that expression of VCAM-1 is also feature size-dependent, although in a converse manner, with expression largely confined to the perinuclear regions in the 0.5 μm gratings of both Ti and Si, but more widely distributed on the unpatterned controls. Moreover, quantitative measurements show decreasing expression with decreasing feature size on both Ti and Si patterned substrates, and expression patterned surfaces is lower than the unpatterned controls, e.g., expression on the 0.5 μm Ti gratings is 3.6 times lower than unpatterned Ti. However, expression on patterned Si is higher than

on comparably patterned Ti, e.g., expression on the 0.5 μm Si gratings is 41 % higher than on 0.5 μm Ti gratings. Finally, expression on sub-micrometer patterned Ti and Si is lower than the tissue culture plastic control.

3.4. Discussion

The data presented herein demonstrate that EC response is enhanced with decreasing feature size on patterned Ti substrates down to 0.5 μm ; specifically, decreasing feature sizes are shown to promote greater adhesion, proliferation, and elongation, as well as a more athero-protective phenotype *in vitro*, which therefore suggests promise for facilitating the reestablishment of a functional endothelium *in vivo*. Moreover, the data show that patterning of Si substrates also elicits favorable trending in EC response with decreasing feature size into the sub-micrometer regime, albeit to a lesser extent than comparable Ti gratings. This therefore suggests that while topographical cueing can be used to promote enhanced EC response on both materials, their differing surface chemistries affect the ultimate magnitude of cellular response.

3.4.1. Endothelial Cell Response as a Function of Substrate Material and Topography

While exploration of the mechanisms underlying the differential EC response observed on comparably-patterned Ti and Si substrates is beyond the scope of the current study, one potential explanation could lie in the differing stiffnesses of these substrates. Studies have shown that ECs, like many adherent cells, are affected by variation in substrate stiffness. Typical responses include migration toward stiffer regions, as well as

increased adhesion and spreading with increasing substrate stiffness (Gray *et al.* 2003; Luetjering and Williams 2007; Ohya *et al.* 2005; Wallace *et al.* 2007; Yeung *et al.* 2005). However, our observations (e.g., Figure 3-6) show reduced spreading on the stiffer Si substrates ($E_{Ti} = 105$ GPa (Luetjering and Williams 2007) & $E_{Si} = 130 - 188$ GPa (Hopcroft *et al.* 2010)). Moreover, the stiffnesses of the current substrates are likely to be well-beyond the threshold for significant differential response, since their moduli greatly exceed those of the polymeric substrates used in previously reported studies (0.1 kPa – 2.5 MPa). Consequently, this suggests against substrate stiffness as a potential explanation in the current study.

An alternative, and perhaps more plausible explanation for the observed differential response, may lie in the differing adhesive ligand presentation on these materials. It is well known that adhesive ligands (e.g., R-G-D) presented by surface-adsorbed plasma proteins (e.g., fibrinogen and fibronectin) act as binding sites for transmembrane integrins. Moreover, it well known that the specific presentation of these ligands, in turn, depends upon the physicochemical properties of the substrate (Wheeldon *et al.* 2011). Finally, it has been recently shown that EC adhesion and spreading typically increase with increasing ligand density until saturation (Le Saux *et al.* 2011; Reinhart-King *et al.* 2005). Consequently, this suggests that adhesive ligand density and/or presentation is more favorable on Ti compared to Si (or more specifically, on the oxide surfaces thereon (Zuruzi *et al.* 2013)), as evidenced by the increase in cell density (Figure 3-5) and spreading (Figure 3-6), and athero-resistant signaling modulation (Figures 3-10a and 3-10b) observed on Ti relative to comparably-patterned Si. Studies are currently

underway to quantify differential plasma protein adsorption on patterned Ti and Si substrates, and determine how this affects the availability of R-G-D sites for binding of integrins such as alpha v beta iii ($\alpha_v\beta_{iii}$), which may play a crucial role in cell adhesion and behavior (Belvisi *et al.* 2005).

Regarding topography specifically, it is well-known that micro- to nano-scale topography can independently affect the amount, spatial distribution, and conformation of adsorbed proteins, as well as the composition of the adsorbed protein layer that forms during exposure to complex biological fluids (Luong-Van *et al.* 2013). Moreover, it has been recently shown that fibronectin adsorption is increased considerably on patterned Si substrates with deep submicrometer scale gratings when compared to planar controls (Elter *et al.* 2012; Salakhutdinov *et al.* 2008), as is the degree of native folding (Elter *et al.* 2012). This suggests that the enhanced EC responses observed in the current study may arise from increasing protein adsorption with decreasing features sizes, which provides increased protein-protein interactions that help stabilize native conformations against denaturation by protein-substrate interactions. However, the considerable differences in grating depth (i.e., 0.09 μm in (Elter *et al.* 2012; Salakhutdinov *et al.* 2008) vs. 1.3 μm in the current study) and profile (i.e., sinusoidal in (Elter *et al.* 2012) vs. rectangular in the current study) demonstrate the need for further studies to quantify protein adsorption and conformation on the current patterned Ti and Si substrates specifically.

3.4.2. Comparison to Previous Studies

Although the current study is the first to explore differential EC response on micrometer to sub-micrometer patterned Ti and Si substrates, it is instructive to compare our observations to those reported by others for polymeric substrates patterned with gratings of similar feature size. As in the current study, cellular alignment and elongation along the grating axis is reported in nearly all studies with features smaller than the dimensions of typical ECs (i.e., features < 20 μm) (Barbucci *et al.* 2003; Bettinger *et al.* 2006; Bettinger *et al.* 2008; Biela *et al.* 2009; Brown *et al.* 2011; Di Rienzo *et al.* 2013; Franco *et al.* 2011; Hwang *et al.* 2010; Jiang *et al.* 2002; Liliensiek *et al.* 2010; Morgan *et al.* 2012; Song *et al.* 2011; Uttayarat *et al.* 2008; Uttayarat *et al.* 2005). However, while increasing proliferation with decreasing groove width is observed in the current study, the opposite (Bettinger *et al.* 2008; Liliensiek *et al.* 2010) or minimal differential response (Uttayarat *et al.* 2005) has been reported in studies with patterned polymers. Moreover, while decreasing features sizes are shown to upregulate vWF and downregulate VCAM-1 expression in this study, minimal differential expression has been reported by others (Bettinger *et al.* 2008; Song *et al.* 2011). These differences may arise from a number of factors, including, among others: a) the relatively shallow nature of the grooves in those earlier studies (i.e., groove depth $\leq 1 \mu\text{m}$ vs. 1.3 μm for the current study); b) the different cell types used (i.e., human umbilical vein ECs, human endothelial progenitor cells, & bovine aortic ECs vs. HECs in the current study); c) the differing substrate surface chemistries and mechanical properties (e.g., polyurethane, cyclic olefin copolymer, polydimethylsiloxane, etc. vs. Ti & Si in the current study); and/or d) the absence of

substrate pre-treatment prior to cell seeding in the current study (i.e., neither oxygen plasma treatment, nor pre-incubation with fibronectin, collagen, BSA, etc. were used in the current study).

3.4.3. Implications for Ti- and Si-based Implantable Microdevices

The favorable trending of EC response with decreasing feature size in the current study suggests promise for use of patterning as a means for improving the safety, efficacy, and performance of novel Ti- and Si-based implantable microdevices. For example, within the context of vascular stents, the observed enhancement of proliferation and athero-protective phenotype *in vitro* suggests potential for use of patterning to accelerate endothelialization and healing *in vivo*. This could therefore provide means for addressing a lingering safety concern associated with current drug-eluting stents, namely late-stent thrombosis resulting from delayed healing (Garg and Serruys 2010). Indeed, first evidence demonstrating this potential *in vivo* was recently reported by Sprague *et al.*, who showed that endothelialization was accelerated on stents patterned with 15 μm groove width gratings (Sprague *et al.* 2012). However, since the current study demonstrates favorable trending of EC response with decreasing feature size into the sub-micrometer realm, this suggests potential for even further improvement. We have recently demonstrated the fabrication of the first sub-micrometer patterned stents that will eventually provide capability for evaluating this potential *in vivo* (Gott *et al.* 2012).

It is also conceivable that patterning-induced enhancement of EC response could provide means for facilitating greater neovascularization on Si-based wirelessly-controlled

implantable drug delivery microchips (Farra *et al.* 2012). As reported by Bettinger *et al.*, sub-micrometer patterning of a polymeric substrate can promote the formation of EC-based supercellular band structures that facilitate the subsequent formation of capillary tubes roughly aligned with the grating axis (Bettinger *et al.* 2008). As such, potential may exist for using patterning to guide capillary tube formation towards the reservoir openings on the surface of drug delivery microchips. Although further studies are required to validate this conjecture, this suggests potential for facilitating the establishment of a direct connection to the surrounding vasculature for applications where rapid systemic delivery is required. Moreover, the observation in the current study of greater EC response on patterned Ti relative to patterned Si suggests the potential superiority of Ti for such devices.

4 TITANIUM STENT CREATION AND INTEGRATION WITH SUB-
MICROMETER SCALE SURFACE PATTERNING

4.1. Introduction

Vascular stents are millimeter-scale, cage-like devices used to reestablish the patency of stenosed blood vessels (i.e. vessels narrowed by disease or dysfunction). Stents have found use in many applications, one of the most common of which is percutaneous coronary intervention, where they enable restoration of flow in coronary arteries narrowed by chronic accumulation of atherosclerotic plaque. In such applications, stents provide a less invasive alternative to other revascularization procedures, such as bypass grafting. This has been achieved through use of a catheter-based deployment approach, wherein a crimped (i.e. collapsed) stent mounted on a deflated balloon catheter is introduced into the body through a small incision to access the vasculature. The stent is then guided intravascularly to the target lesion and deployed by balloon inflation, which dilates the vessel, compresses the plaque, and expands the stent into juxtaposition with the vessel's inner wall. Plastic deformation allows the stent to maintain its shape and position within the vessel after the balloon is deflated and withdrawn, thus enabling the stent to serve as a permanent scaffold against vascular recoil.

Despite the success of coronary stenting, adverse physiological responses, such as restenosis and late stent thrombosis (LST), remain challenges to safety and efficacy. As a review, restenosis is often seen in BMS and is characterized by luminal re-narrowing produced by vascular smooth muscle cell hyperproliferation in response to implantation-induced injury. Drug-eluting stents suppress restenosis via controlled release of antiproliferative or immunosuppressive drugs from a polymer coating applied to the stent. However, growing evidence indicates greater potential for LST in DES than BMS. While

incidence is low (< 5%), fatality can be as high as 45% (McFadden *et al.* 2004). Although the mechanism is not fully understood, delay of healing caused by drug elution may play a significant role (Virmani *et al.* 2004). This inhibits reestablishment of the endothelium, the native vessel lining, thus increasing potential for LST. Since platelet aggregation is the basis of LST, current mitigation strategies rely on oral dual antiplatelet therapies (DAPT), such as aspirin and clopidogrel. However, clopidogrel is ineffective for ~25% of patients (Gurbel *et al.* 2003; Lau *et al.* 2004) and may interact adversely with other common drugs (O'Donoghue *et al.* 2009). Moreover, poor patient compliance is common with oral therapies, and is implicated in increased risk of death for those on DAPTs (Spertus *et al.* 2006). Taken together, this provides impetus for developing new strategies that facilitate, rather than delay healing, and also minimize reliance upon pharmacological intervention.

As reported earlier, rational design of surface topography may provide a new means for addressing these issues via modulation of cell-substrate interactions. Specifically, using our novel Ti DRIE technique (Aimi *et al.* 2004; Parker *et al.* 2005), we demonstrated the fabrication of planar Ti substrates patterned with precisely-defined gratings composed of periodic arrays of grooves, with groove widths ranging from 50 μm at the largest, to 0.5 μm at the smallest, the latter of which lie well beyond the reach of other metallic micromachining methods. Our *in vitro* studies evaluating endothelial cell response to these substrates demonstrated that decreasing feature sizes promoted: a) increased adhesion and proliferation; b) cellular morphology reminiscent of the native endothelium; and c) increased atheroprotective biomolecule expression (Lu *et al.* 2008; Vandrangi *et al.* 2012). Collectively, these results provide early evidence supporting a new

therapeutic paradigm in vascular stenting, where rationally-designed surface patterning facilitates healing, thus providing potential for complementing, or replacing, current pharmacological interventions.

However, while our initial results suggest promise, *in vitro* studies on planar substrates provide only limited utility with regard to predicting cellular response *in vivo*. Consequently, evaluation in more physiologically-relevant contexts is required, i.e., those that provide exposure to the complex multicellular milieu, flow-induced shear, and tissue-device interactions present *in vivo*. This necessitates development of means for moving beyond planar substrates to three-dimensional devices, since this will enable juxtaposition of patterned surfaces within the vascular wall in a manner consistent with conventional stents. Furthermore, since our earlier studies were resolution-limited to 0.5 μm minimum feature size, extension of our Ti DRIE capability to the deep sub-micrometer realm (i.e. $\ll 0.5 \mu\text{m}$) is required to evaluate the ultimate limits of favorable cellular response scaling with decreasing feature size. We recently reported preliminary results from efforts focused on achieving these objectives (Gott *et al.* 2012). Herein, we expand upon these results and detail further advancements in the design, fabrication, simulation, and mechanical testing of vascular stents with rationally-designed, deep sub-micrometer scale surface patterning.

4.2. Materials and Methods

4.2.1. Design Considerations

Stents are typically manufactured via laser-based micromachining of thin-wall tubular forms. However, this technique does not provide sufficient resolution for deep

sub-micrometer scale patterning (Martinez and Chaikof 2011), thus necessitating exploration of other alternatives. Our Ti DRIE technique now provides potential for achieving such features, and doing so in a material of direct relevance to vascular stenting. However, the inherently planar nature of this technique precludes its use for direct patterning of non-planar structures such as stents.

This limitation has been circumvented in the current work through use of an innovative approach originally developed by Takahata and Gianchandani (Takahata and Gianchandani 2004). In this approach, planar stent forms are transformed into the desired cylindrical geometry via threading of a balloon catheter through the device, followed by balloon inflation to expand device structures out of the original substrate plane. Using this approach, Takahata and Gianchandani demonstrated the fabrication of stainless steel stents with mechanical response comparable to commercially-available stents. However, it is important to note that the microelectrodischarge machining process they used for the fabrication of their planar stent forms does not provide sufficient resolution for deep sub-micrometer scale surface patterning (Murali and Yeo 2004), thus precluding its use here.

Figure 4-1 shows a schematic representation of a small section of the Ti-based planar stent form developed in the current work, which consists of transverse cross-bands connected by longitudinal sidebeams spanning the length of the stent. The cross-bands are comprised of a series of s-shaped involute structures whose deformation is intended to yield a cylindrical stent. As illustrated in Figure 4-2, the planar stent form (Figure 4-2a) is transformed into a compact cylindrical geometry by first manually threading a tapered needle through the structure to deform the cross-bands above and beneath the substrate

plane (Figure 4-2b). As the needle is further advanced, the stent begins to match the cylindrical profile of the needle. The needle is advanced until the diameter of the stent matches that of a conventional deflated balloon catheter (~1.6 mm). Finally, the stent is mounted onto the balloon catheter (Figure 4-2c), after which it is ready for deployment using conventional angioplasty techniques.

For the purposes of the current work, which sought to demonstrate preliminary proof-of-concept, the balloon-mounted Ti stents were deployed into 3 mm inner diameter polyvinyl chloride (PVC) mock arteries lubricated with silicone oil (Fisherbrand Clear PVC tubing, Fisher Scientific, Waltham, MA). A commercial inflation device (INDEFLATOR PLUS 20, Guidant, Santa Clara, CA) was used to pressurize the balloon catheters to 12 atm, which is within the typical range used for conventional stent deployment. During inflation, the stents underwent plastic deformation via bending, rotation, and torsion of the cross-bands and side-beams, thus allowing large deformations without exceeding the tensile strength of the material. The deployed stents were then released from the mock artery by soaking in acetone, which caused swelling of the PVC. Figure 4-2d shows a digital micrograph of a deployed Ti stent removed from the mock artery. The micrograph demonstrates that expansion produces the desired cylindrical stent geometry consisting of circumferentially-oriented cross-bands connected by longitudinal side-beams.

4.2.2. Finite Element Analysis

Elastoplastic finite element analysis (FEA) was used to simulate: a) the stent deployment process; and b) the subsequent mechanical testing of the deployed stent via

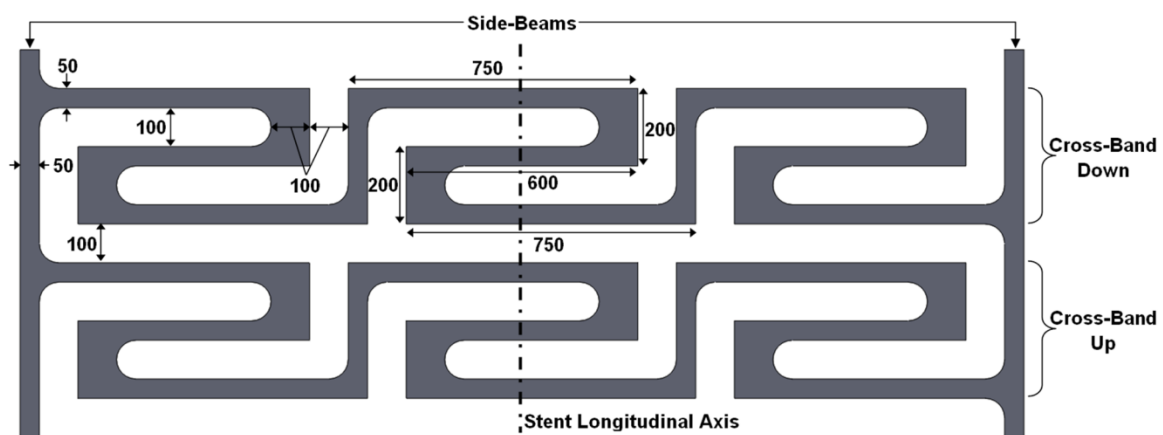


Figure 4-1. Schematic depiction of a portion of the planar stent form design. All units in micrometers.

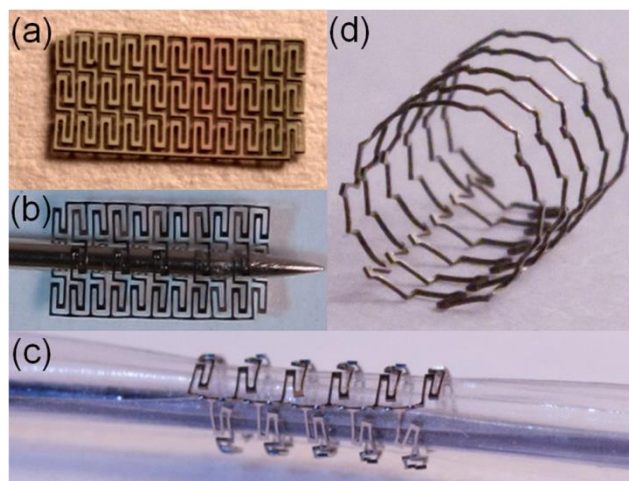


Figure 4-2. Digital micrographs of the Ti stent transformation process: a) Planar stent form deep etched through an 80 μm thick Ti substrate; b) Initial phase of tapered needle threading process to transform the planar stent form into a compact cylindrical geometry for balloon mounting; c) Balloon-mounted stent; and d) Ti stent after deployment into a mock artery via balloon inflation (stent removed from mock artery for image).

uniaxial radial compression. These simulations were performed in order to corroborate experimental observations in the current work, as well as expedite future design improvement efforts. Both simulations were performed using a commercial FEA package (Femap with NX Nastran Advanced Nonlinear, Siemens PLM, Cypress, CA).

For the purposes of this preliminary study, a bilinear material model was assumed, as was isotropic hardening. Relevant material properties used for Grade 1 commercially-pure Ti (CP-Ti) included: Young's modulus = 103 GPa, Poisson's ratio = 0.34, density = 4.51 g/cm³, and yield strength = 170 MPa (Gerhard *et al.* 1994). A tabulated value for tangent modulus could not be found in the literature, thus an estimated value of 297 MPa was used in both simulations. This value was based upon the average slope of the stress-strain curve within the plastic deformation regime. For both simulations, the stent geometry was simplified to a single pair of upper and lower cross-bands to reduce computation time, and results were normalized accordingly. The same mesh was used for all simulations, and consisted of 4077 brick elements and 7668 nodes. Additionally, constraining moments were applied at the free ends of the side-beams to prevent rotation induced by the longitudinal offset between the upper and lower cross-bands. Finally, to allow evaluation of both material and design contributions to mechanical response, simulations were also performed for stents with identical design and dimensions, but made from 304 stainless steel (304 SS). Material properties used for these simulations included: Young's modulus = 193 GPa, Poisson's ratio = 0.27, density = 8 g/cm³, yield strength = 207 MPa, and tangent modulus = 692 MPa (Callister 2007; Takahata and Gianchandani 2004).

For the stent deployment simulation, the balloon was modeled as a cylinder located within the lumen of the mounted stent. In order to simplify the analysis, the initial configuration of the stent was assumed to be cylindrical and stress-free with cross-bands oriented as shown in Figure 4-2c. While this ignored the plastic deformation produced during the threading process, this was expected to have only minor effect on the simulations, since the majority of plasticity produced during threading is localized to the side-beams, and the majority of plasticity produced during subsequent deployment is localized to the cross-bands. During deployment, frictionless contact was assumed and the balloon was modeled with rigid-contact thin shell elements. Since the intent of these simulations was simply to assess the stent's mechanical response under imposed displacement produced by an idealized balloon wall, this was presumed to be an acceptable simplification. The balloon diameter was incrementally increased until the outer diameter of the stent reached 3 mm (to simulate deployment into a vessel with matching inner diameter).

For the mechanical testing simulation, the final expanded stent from the deployment simulation was used as the initial device configuration (without the balloon). Two parallel plates were situated above and below the stent to simulate the compression platens of a uniaxial radial compression test. During compression, frictionless contact was assumed and the platens were modeled with rigid plate elements. Since the intent of these simulations was simply to assess the stent's mechanical response under imposed displacement produced by idealized platens, this was presumed to be an acceptable simplification. The separation distance between the plates was incrementally decreased

until 1.5 mm total displacement was applied to the stent (i.e. half the original deployed diameter). Extraction of load-displacement data from the simulation allowed determination of radial stiffness and overall mechanical response of the stents.

4.2.3. Fabrication

As discussed earlier, evaluation of rationally-designed, deep sub-micrometer scale surface patterning in physiologically-relevant contexts requires the development of means for: a) creating cylindrical stents from micromachined planar Ti foils; and b) deep sub-micrometer scale surface patterning of Ti. The combination of our Ti DRIE capability with the geometric transformation approach described by Takahata and Gianchandani allowed realization of the former. However, until recently, realization of the latter was precluded by the resolution limits of the projection lithography instrument used in our earlier studies (GCA Autostep 200 i-line Wafer Stepper, 3C Technical, Gilbert, AZ; 0.5 μm resolution). This limitation was circumvented in the current study by migration to a new projection lithography instrument which provided higher resolution (PAS 5500/300 DUV Stepper, ASML, The Netherlands; 0.15 μm resolution). However, direct lithographic patterning of Ti substrates using this tool was precluded by their sub-optimal surface roughness ($R_a \sim 2 \text{ nm RMS}$). This limitation was addressed through the use of thermal NIL with Si imprint masters fabricated using the new projection lithography instrument. Thermal NIL was selected for this application on the basis of its superior tolerance of poor surface quality, as well as the opportunity it provides for facile, large-area patterning, which is a key consideration for eventual clinical and commercial translation. Using NIL,

grating-based PR patterns were defined with groove widths as small as 0.15 μm , and grating pitch twice the groove width (i.e. equal lines and space patterns).

The imprint masters were fabricated using 500 μm thick single crystal Si wafers, which possessed sufficiently low surface roughness ($R_a \sim 0.2$ nm RMS) for achieving the ultimate resolution of the new projection lithography instrument. The substrates were first were solvent cleaned by sequential ultrasonic agitation in acetone and isopropanol, followed by DI water rinsing and N_2 drying. They were then dehydration baked, followed by application of HMDS as an adhesion promoter. Afterwards, PR was applied via spin-coating (AZ nLOF 5510, Clariant, Muttenz, Switzerland), followed by photolithographic patterning. Fluorine-based dry etching was used to transfer the patterns into the underlying Si (Plasmatherm SLR 770 ICP, Unaxis, St. Petersburg, FL; Process conditions: 19 mT chamber pressure, 825 W ICP source power, 15 W substrate power, 54 sccm C_4F_8 , 26 sccm SF_6 , 20 sccm Ar, and 10°C lower electrode temperature), followed by removal of the residual resist by solvent cleaning. To minimize resist adhesion during the subsequent imprinting processes, a monolayer of FDTS was applied to the Si masters using molecular vapor deposition (MVD 100E, Applied Microstructures, Inc., San Jose, CA; Process conditions: 23°C chamber temperature, 600 s reaction time of H_2O and FDTS).

Once the Si imprint masters were completed, the fabrication process for the surface patterned Ti stents was initiated. Double-side polished 80 μm thick Grade 1 CP-Ti foil substrates (99.6% Ti, Tokyo Stainless Grinding Co., Ltd, Japan) were selected to provide sufficient thickness for the stent struts. As shown in Figure 4-3, the fabrication consisted of both front- and back-side processes, beginning with surface patterning on the

front-side (Steps 1-4), followed by stent strut pattern definition from the back-side (Steps 5-9), thus producing a surface patterned planar stent form ready for threading and balloon-mounting.

The front-side surface patterning process began with solvent cleaning of the substrates, followed by ICP PECVD of a 0.2 μm thick SiO_2 etch mask (VLR, Unaxis, St. Petersburg, FL; Process conditions: 15 mT chamber pressure, 400 W ICP source power, 5 W substrate power, 5.9 sccm 100% SiH_4 , 20 sccm Ar, 10 sccm O_2 , and 100°C lower electrode temperature). The substrates were then subjected to oxygen plasma cleaning in preparation for lithographic patterning (PE-IIA, Technics, San Jose, CA; Process conditions: 300 mT chamber pressure and 100 W substrate power). Afterwards, a thermoplastic resist was applied via spin-coating (mr-I 7020, Micro Resist Technology, Germany). The resist was then patterned using the Si imprint masters and thermal NIL (NX2000, Nanonex, Inc., Monmouth, NJ; Process conditions: 140°C / 10 min imprint temperature and time). After imprinting, the residual resist layer at the trench-bottoms was removed by oxygen-based dry etching (E620-R&D, Panasonic Factory Solutions, Japan; Process conditions: 3.75 mT chamber pressure, 75 W ICP source power, 65 W substrate power, and 49 sccm O_2). The resist pattern was then transferred into the underlying SiO_2 by fluorine-based dry etching (E620-R&D; Process conditions: 3.75 mT chamber pressure, 900 W ICP source power, 50 W substrate power, 20 sccm CHF_3 , and 20 sccm CF_4). Afterwards, the substrates were solvent cleaned to remove residual resist, followed by transfer of the mask oxide pattern into the underlying Ti substrate to a depth of 0.8 μm or greater using a modified Ti DRIE process (E640, Panasonic Factory Solutions; Process

conditions: 3.75 mT chamber pressure, 400 W ICP source power, 100 W substrate power, 40 sccm Cl₂, and 4 sccm O₂). Finally, residual mask oxide was removed using fluorine-based dry etching.

Once the front-side surface patterning was completed, the planar stent pattern was defined from the back-side of the substrate. First, ICP PECVD was used to deposit a 4.2 μm thick SiO₂ etch mask. The substrates were then dehydration baked, followed by HMDS priming. Afterwards, PR was applied via spin-coating (AZnLOF 2070, Clariant, Muttenz, Switzerland). The resist was then patterned using contact lithography (MJB 3 UV400, Suss MicroTec, Germany). The resist pattern was transferred into the underlying SiO₂ by fluorine-based dry etching, followed by solvent cleaning to remove residual resist. Transfer of the mask oxide pattern through the underlying Ti substrate was then performed using a modified Ti DRIE process (E620-R&D; Process conditions: 15 mT chamber pressure, 400 W ICP source power, 100 W substrate power, 100 sccm Cl₂, 5 sccm Ar, and 1 sccm O₂). Finally, residual mask oxide was removed using fluorine-based dry etching (E620-R&D; Process conditions: 7.5 mT chamber pressure, 600 W ICP source power, 50 W substrate power, 50 sccm SF₆, and 10 sccm Ar).

4.2.4. Mechanical Testing

The primary function of a stent is to serve as a mechanical scaffold that prevents vascular recoil or collapse after balloon-induced dilation. Consequently, radial stiffness is a key performance metric to characterize with regard to mechanical response. While a

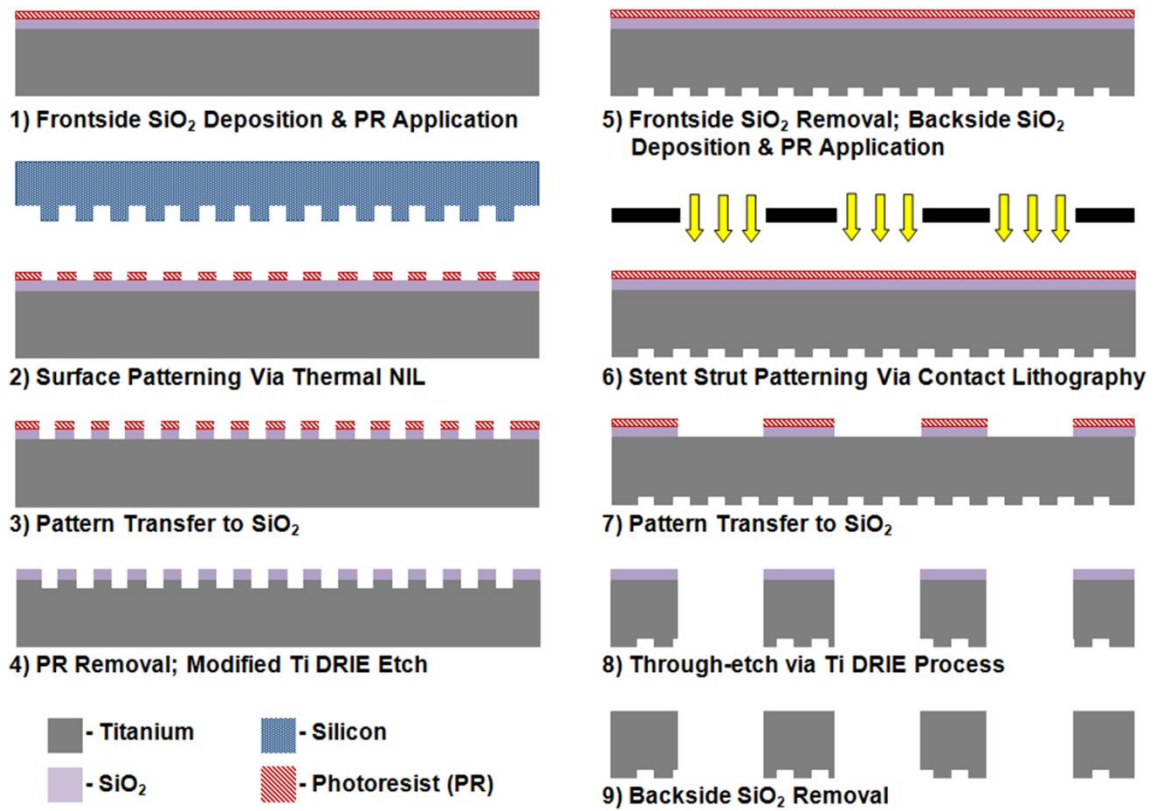


Figure 4-3. Fabrication process flow for surface-patterned planar Ti stent forms.

number of techniques have been developed to measure radial stiffness (e.g., (Duda *et al.* 2000; Dyet *et al.* 2000; Flueckiger *et al.* 1994; Rieu *et al.* 1999)), uniaxial radial compression was selected for the current study, due to its simplicity. Although this technique fails to capture the full complexity of the loading state and constraints experienced by stents *in vivo*, it allows relative comparison between different stent types, thus providing means for preliminary evaluation of the surface patterned Ti stents.

The uniaxial radial compression testing was performed using a low-force universal testing system (ElectroForce 3100, Bose Corporation, Framingham, MA). Testing was performed under displacement control and load response was recorded. Stents were loaded at 2 $\mu\text{m/s}$ until 1.5 mm total displacement was achieved (i.e. half the original deployed diameter), after which they were unloaded. The stents were closely monitored during testing to ensure no slippage occurred. Varying orientations for stent loading were explored (i.e. location of the side-beams was varied with respect to the loading axis), although there was no significant difference in observed response.

4.3. Results

4.3.1. Fabrication

Figure 4-4 shows representative SEM micrographs of a 0.15 μm groove width grating defined in a planar Ti substrate. The high fidelity of pattern transfer is evident (Figure 4-4a), as is the uniformity over large areas (Figure 4-4b). Interestingly, the grain structure of the underlying polycrystalline substrate is also clearly evident in Figure 4-4b. This arises from slight preferential etching of the grain boundary regions in the trench

floors of the grating pattern; however, it is important to note that this does not affect the fidelity or integrity of the grating ridges themselves.

Figure 4-5 shows various SEM micrographs of a deployed Ti stent with 0.75 μm groove width surface patterning. Good deployment uniformity is evident, as are the smooth vertical sidewalls produced by the Ti DRIE process. Significant plasticity is observed in portions of the cross-bands and side-beams (Figures 4-5b and 4-5c); however, there are no obvious instances of cracking or tensile failure. Interestingly, there is clear evidence of preferential plasticity in presumably favorably-oriented grains within the struts (Figure 4-5c), as well as surface slip and/or twinning traces (Figure 4-5d). Finally, there is no evidence that surface patterning serves as an initiation site for strut cracking or tearing during deployment, even in locations of severe deformation (Figure 4-5d). Moreover, minimal surface pattern damage is observed across the stent, and there is only minor and highly localized pattern perturbation in areas of severe deformation (Figure 4-5d).

4.3.2. FEA Simulation and Mechanical Testing

Figure 4-6 shows a representative von Mises stress plot from the FEA simulation of the Ti stent deployment, which is in good agreement with experimental observations. Specifically, the deformed shape (Figure 4-6b) closely follows that of actual deployed stents (e.g. Figures 4-2d & 4-5a). Moreover, the locations of maximum stress in the cross-bands correlate well with the locations of maximum deformation in the actual deployed stents (Figure 4-5c). Finally, the simulation returns maximum stresses below the tensile

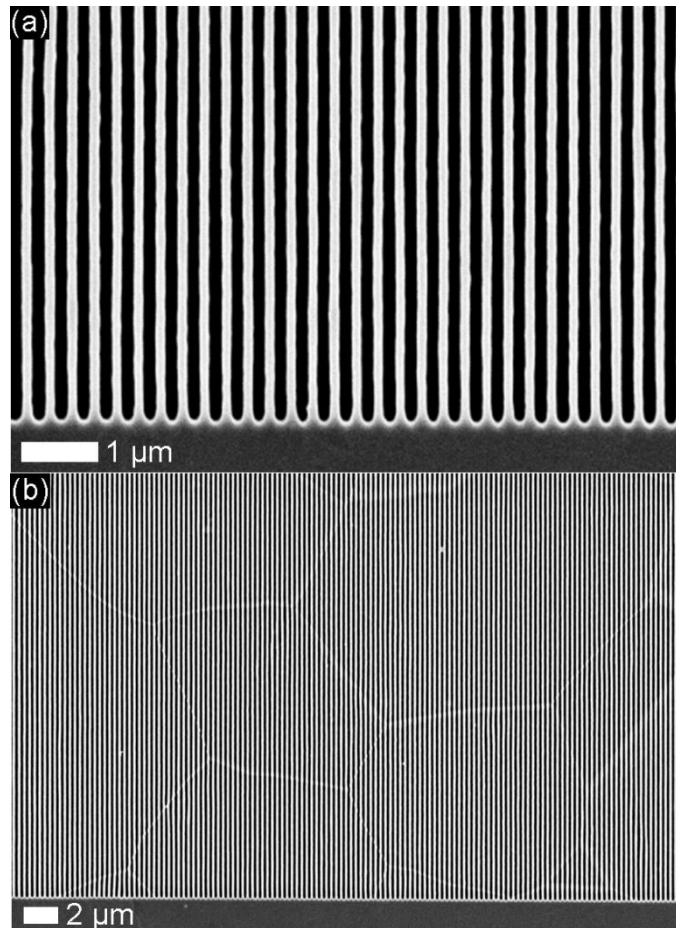


Figure 4-4. SEM micrographs of 0.15 μm groove width grating defined in a planar Ti substrate by Ti DRIE: a) High magnification; b) Low magnification. Grating pitch is 0.3 μm and groove depth is 0.8 μm .

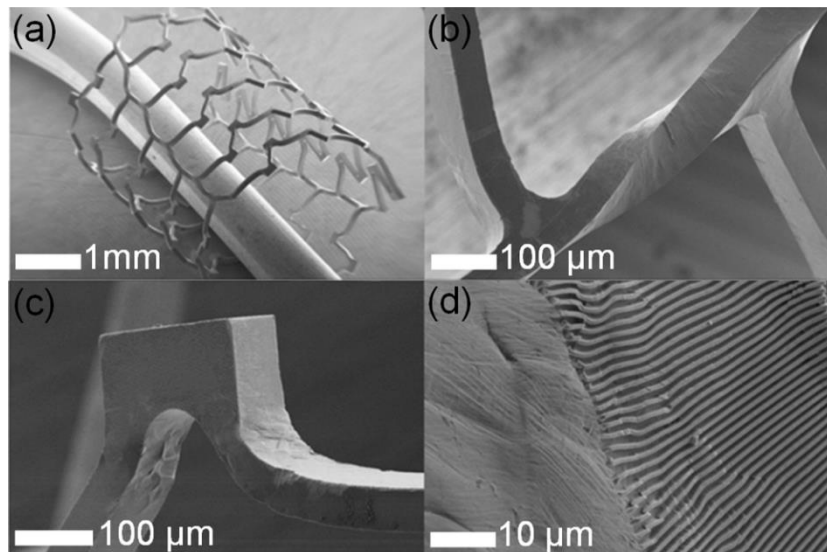


Figure 4-5. SEM micrographs of a balloon-deployed, surface-patterned Ti stent produced by Ti DRIE: a) Full stent; b) Torsionally deformed side-beam and adjoining cross-bands; c) Region of severe cross-band deformation; and d) 0.75 μm groove width surface patterning in a heavily deformed region.

strength of the material (240 MPa (Gerhard *et al.* 1994)), consistent with the experiments (i.e., there were no instances of strut fracture observed in any of the stents deployed in this study).

The load-displacement data from the uniaxial radial compression testing is shown in Figure 4-7. Data for experiments (solid symbols) and FEA-based simulations (open symbols) are included. Experimental data is also included for a commercial stainless steel stent deployed to identical diameter and tested in the same manner. In each case, the load is normalized by the stent's longitudinal length to allow direct comparison between different designs. The data show that deformation response for all stents is characterized by an initially stiff elastic regime (Figure 4-7 inset), followed by an extensive plastic regime. The smooth, continuous nature of the experimental curves confirms the absence of slippage during testing.

As can be seen in Figure 4-7, there is good agreement between the simulated and measured responses for the Ti stents, thus providing initial validation of the simulation and its underlying assumptions. However, there is subtle softening in the simulation of the Ti stents upon the onset of plasticity, which results in deviation from the measured response over the initial portion of the plastic deformation regime (i.e. from ~ 0.1 mm to 0.4 mm displacement). Moreover, the simulated hardening within the intermediate to latter stages of the plastic deformation regime (i.e. ~0.4 mm onwards) slightly underestimates that which is observed experimentally. Finally, it is also interesting to note that the simulated response of the 304 SS stent with identical design as the Ti stent displays the expected

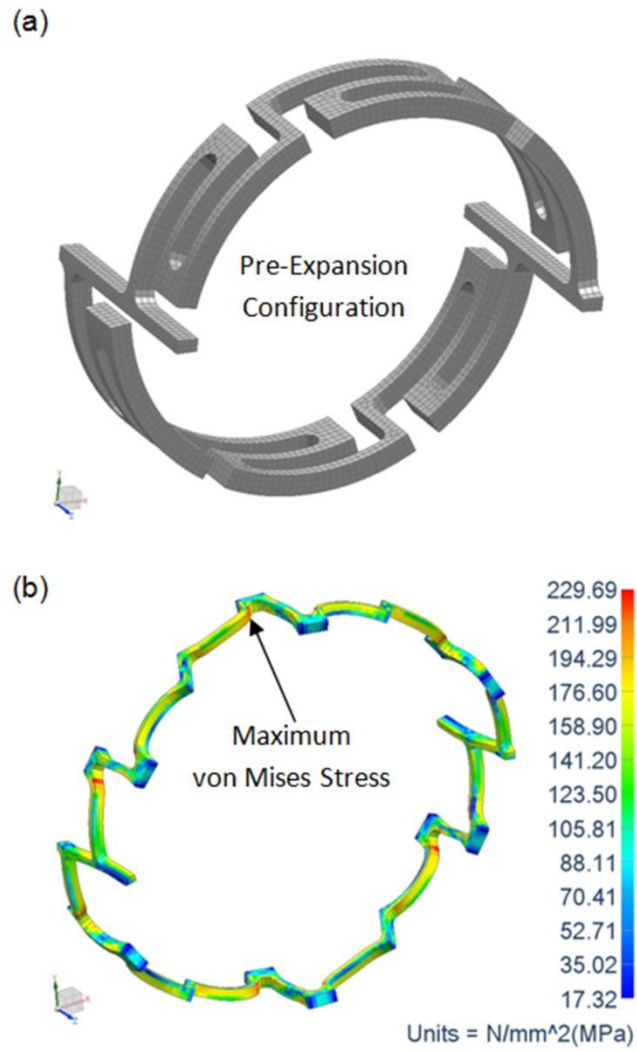


Figure 4-6. Elastoplastic FEA simulation of stent deployment: a) Initial configuration; and b) Von Mises stress plot of deployed device.

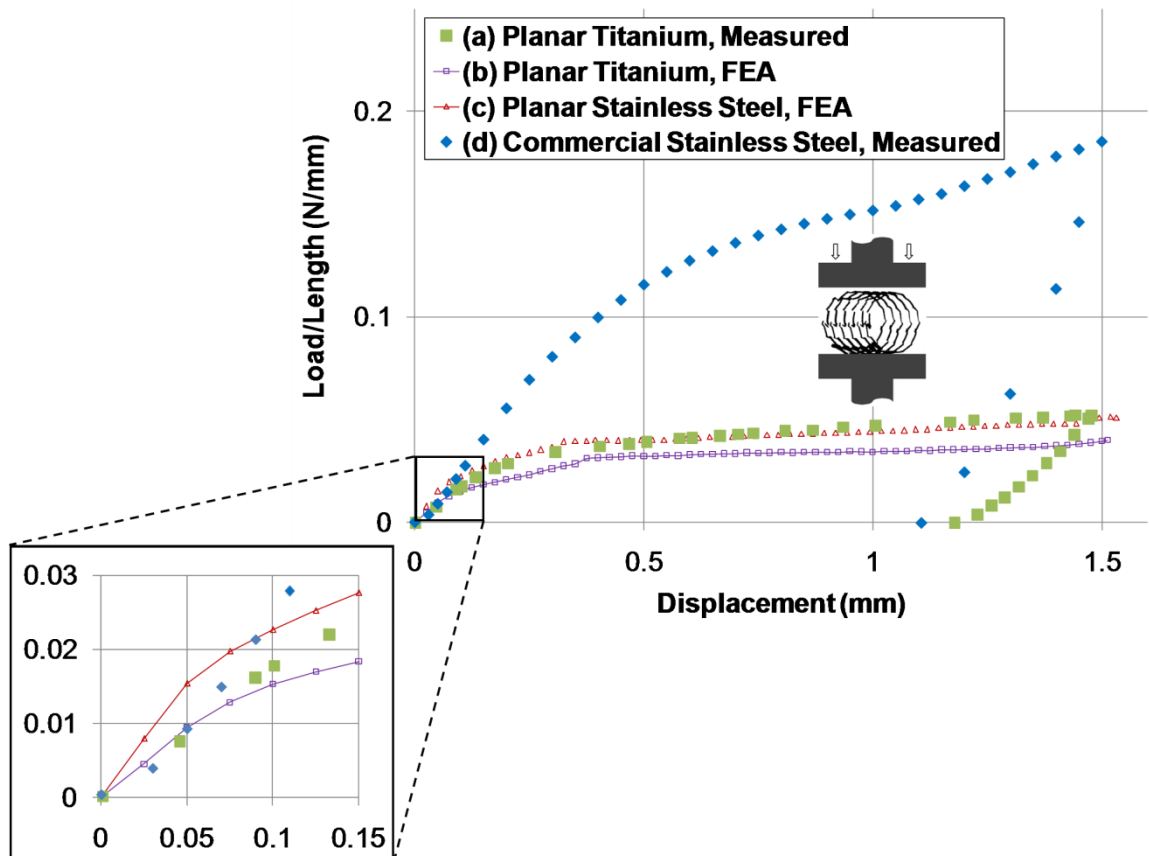


Figure 4-7. Normalized load-displacement data for mechanical testing and FEA-based simulation of deployed stents under uniaxial radial compression: a) Ti stent, measured; b) Ti stent, FEA; c) 304 SS stent, FEA; and d) Commercial stainless steel stent, measured. Inset: Magnified view of elastic deformation regime. Note: Stents in a), b), & c) share identical design and dimensions.

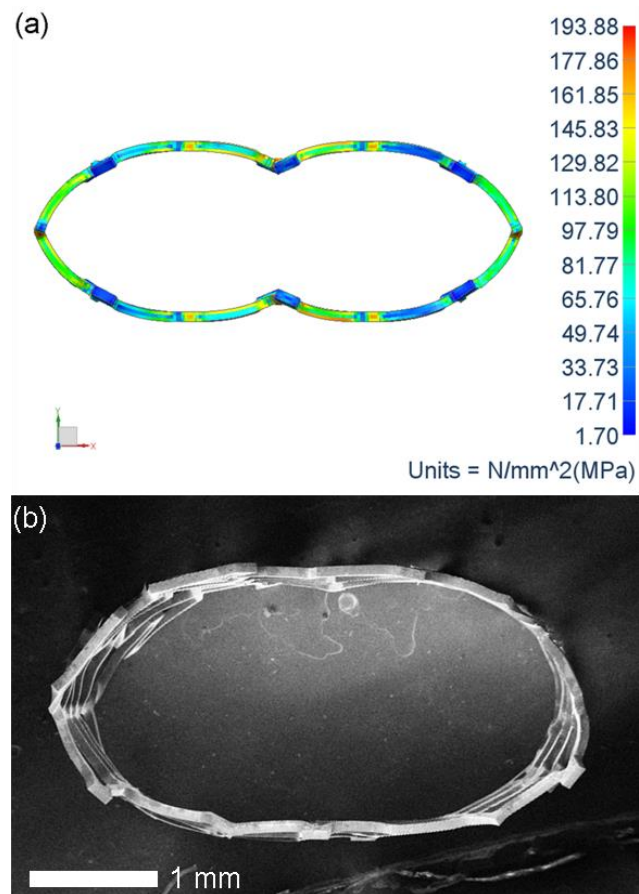


Figure 4-8. Deformation response of deployed Ti stent after 1.5 mm uniaxial radial compression: a) Longitudinal view of FEA simulation; and b) Longitudinal view SEM micrograph of tested stent.

increased stiffness in the elastic regime (Figure 4-7 inset), but rather similar plastic response subsequently.

The simulated and experimentally observed deformation response of the Ti stent under uniaxial radial compression is presented in Figure 4-8. As can be seen, there is good agreement with experimental observations. The simulated deformed shape (Figure 4-8a) generally follows that observed experimentally (Figure 4-8b), and the maximum stresses are well below the tensile strength of Ti (i.e., there were no instances of strut fracture observed during mechanical testing of any of the stents in this study). However, the buckling in the vicinity of the platen contacts predicted by the simulations was not observed experimentally. In the simulations, the onset of this buckling coincided with the onset of plasticity, thus causing the aforementioned softening relative to the experimental response within the initial portion of the plastic regime in Figure 4-7.

4.4. Discussion

4.4.1. Deep Sub-Micrometer Scale Surface Patterning

The 0.15 μm groove width patterns demonstrated in Figure 4-4 are the smallest features achieved to date using our Ti DRIE technique. This represents a significant advancement beyond the 0.5 μm resolution limit of our earlier studies (Gott *et al.* 2012; Lu *et al.* 2008; Vandrangi *et al.* 2012). Moreover, this further extends the minimum feature size capability of our technique well beyond that of other metallic micromachining methods, most of which are limited to minimum feature sizes in excess of a few tens of micrometers.

As discussed earlier, the importance of surface patterning at the deep sub-micrometer scale lies in the favorable trending observed in our previous *in vitro* studies (Lu *et al.* 2008; Vandrangi *et al.* 2012), which suggested potential for further enhancement of cellular response with continuing feature size reduction below 0.5 μm . The exact mechanism for this favorable scaling is still unclear. However, one possible explanation may lie in the increasing similarity of such surface patterns to the topography presented by the native basement membrane. Since this specialized extracellular matrix is typically composed of collagen fibrils with diameters ranging from 260 – 410 nm (Bozec *et al.* 2007), this suggests that even greater gains may be possible with further reduction of surface pattern feature sizes to these dimensions. In a parallel effort, we are currently evaluating endothelial cell response on deep sub-micrometer scale patterned Ti substrates to test this hypothesis. Results from these studies will be the focus of a forthcoming report.

4.4.2. Surface Patterned Balloon-Deployable Ti Stents

As discussed previously, the current effort was also motivated by the desire to develop means for eventually assessing vascular cell response to surface patterning in more physiologically-relevant contexts (e.g., *in vitro* organ cultures, where surface patterned stents are deployed into freshly harvested artery segments, followed by culture in a perfusion system). The surface patterned stents demonstrated here represent the first attempt to develop a device platform that will provide such capability, and do so in a manner consistent with conventional vascular stents. This is a key distinction, since: a) most studies exploring the effect of micro- and nanoscale topography on vascular cells

have been limited to *in vitro* cultures on planar substrates; and b) the few *in vivo* studies that have been reported (Dibra *et al.* 2005; Wieneke *et al.* 2003), have focused on stents with randomly structured nanoscale topographies, which were found to have only minimal impact on restenosis mitigation.

The lack of demonstrable benefit provided by randomly nanostructured surfaces *in vivo* would seem to discourage further study. However, it is important to recognize that the stents developed in the current effort possess highly anisotropic, grating-based topographies with precisely-defined feature size, depth, and morphology (hence the designation patterned surfaces). This distinguishes them from randomly nanostructured surfaces, which typically possess relatively isotropic features with large variation in size, depth, and morphology. The importance of such distinction is manifold. First, numerous *in vitro* studies have shown that patterned surfaces may elicit more desirable cellular responses than randomly structured surfaces with features of comparable length scale (Bettinger *et al.* 2009). Second, enhanced endothelialization has been reported on stainless steel stents with microscale grooved surfaces (12 – 15 μm groove width range), relative to stents with smooth surfaces (Fuss *et al.* 2001). When coupled with our own *in vitro* studies demonstrating enhanced endothelial response on sub-micrometer scale gratings relative to larger microscale gratings (Lu *et al.* 2008; Vandrangi *et al.* 2012), this suggests potential for even greater endothelialization on sub-micrometer scale patterned stents *in vivo*. Finally, as discussed earlier, our own studies have also shown that sub-micrometer gratings can induce more native endothelial morphology relative to larger microscale gratings, as well as promote increased atheroprotective biomolecule expression (Lu *et al.*

2008; Vandrangi *et al.* 2012). This is particularly important, since this suggests potential for recapitulating more native endothelial functionality as well, which is crucial for ensuring long-term stenting success. It is not yet known whether such favorable responses will translate to *in vivo* settings; however, the surface patterned stents developed in the current effort will eventually enable such studies to be performed.

4.4.3. Mechanical response

The feasibility of the surface patterned Ti stent fabrication process and deployment scheme is demonstrated herein. However, the mechanical testing data (Figure 4-7) show that the performance of our current stents does not match that of the commercial stainless steel stent. While this suggests need for further improvement, it is important to note that the radial strength of our Ti stents is comparable to that of recently reported polymeric stents, which have shown satisfactory mechanical performance in early clinical trials (Onuma and Serruys 2011). Moreover, the similarity of the FEA-simulated behavior of our Ti stents and the 304 SS stents of identical design and dimensions indicates that design, rather than material is the primary limitation. This, therefore, suggests ample opportunity for future design improvement, should the need arise.

5 TITANIUM STENT DESIGN IMPROVEMENT

5.1. Introduction

The fabrication of planar titanium stents with sub-micrometer scale surface patterning has demonstrated the capability of novel Ti DRIE processes to explore a new stenting platform to promote rapid reendothelialization. Under radial stiffness testing, an indicator of a stent's ability to main patency, design is shown to be the limiting factor when comparing planar Ti stents to commercial stainless steel stents (e.g. commercial stents possessed twice the radial stiffness). While this may not be problematic, as previously mentioned, because radial strengths are similar to those reported for polymeric stents (Onuma and Serruys 2011), a better understanding of how design affects the range of mechanical responses possible in Ti stents will aid in our long-term goal to develop a new stenting paradigm. Herein, we consider planar stent designs using our FEA models to investigate higher radial stiffness responses previously barred by material limitations.

5.2. Materials and Methods

5.2.1. Design Considerations

For a stent undergoing radial compressions, a hollow cylinder is the stiffest shape that can be achieved while still allowing unimpeded flow of blood through the lumen. Several ratchet-type designs (Onuma and Serruys 2011) have taken hold of this concept by using slide-and-lock mechanisms to change the diameter of coiled stents without plastic deformation. This aids in limiting recoil or separation of the stent from the vessel wall and locks struts in place that are oriented circumferentially for higher radial stiffness. The sliding aspects of these designs, however, prevent their use for our Ti stents because of the

likelihood of inflicting damage to the surface patterning. Integrating a locking device in-plane, then, not only preserves surface patterning, but benefits from increased radial stiffness of the circumferentially-oriented and locked struts.

Figure 5-1 shows a schematic representation of a small section of the Ti-based planar stent very similar to the layout of our involute stent in that it consists of transverse cross-bands connected by longitudinal sidebeams spanning the length of the stent. The primary difference is the cross-band links, which are a series of longitudinally-elongated hexagons, each encompassing a locking mechanism comprised of a deformation guide and complementary hooks. A similar method to Figure 4-2 is used, where the planar stent form is transformed into a cylindrical geometry by first manually threading a tapered needle through the structure to deform the cross-bands above and beneath the substrate plane and open the stent for mounting on a balloon catheter.

A commercial inflation device (INDEFLATOR PLUS 20, Guidant, Santa Clara, CA) was used to pressurize the stent-mounted balloon catheters to 12 atm, which is within the typical range used for conventional stent deployment. During inflation, the hexagon is plastically deformed such that its outer components are circumferentially aligned, bringing the hooks in contact with each other and locking the stent into the desired stent diameter, which for this study is 3 mm. Also, the stents as a whole underwent plastic deformation via bending, rotation, and torsion of the cross-bands and side-beams, thus allowing large deformations without exceeding the tensile strength of the material.

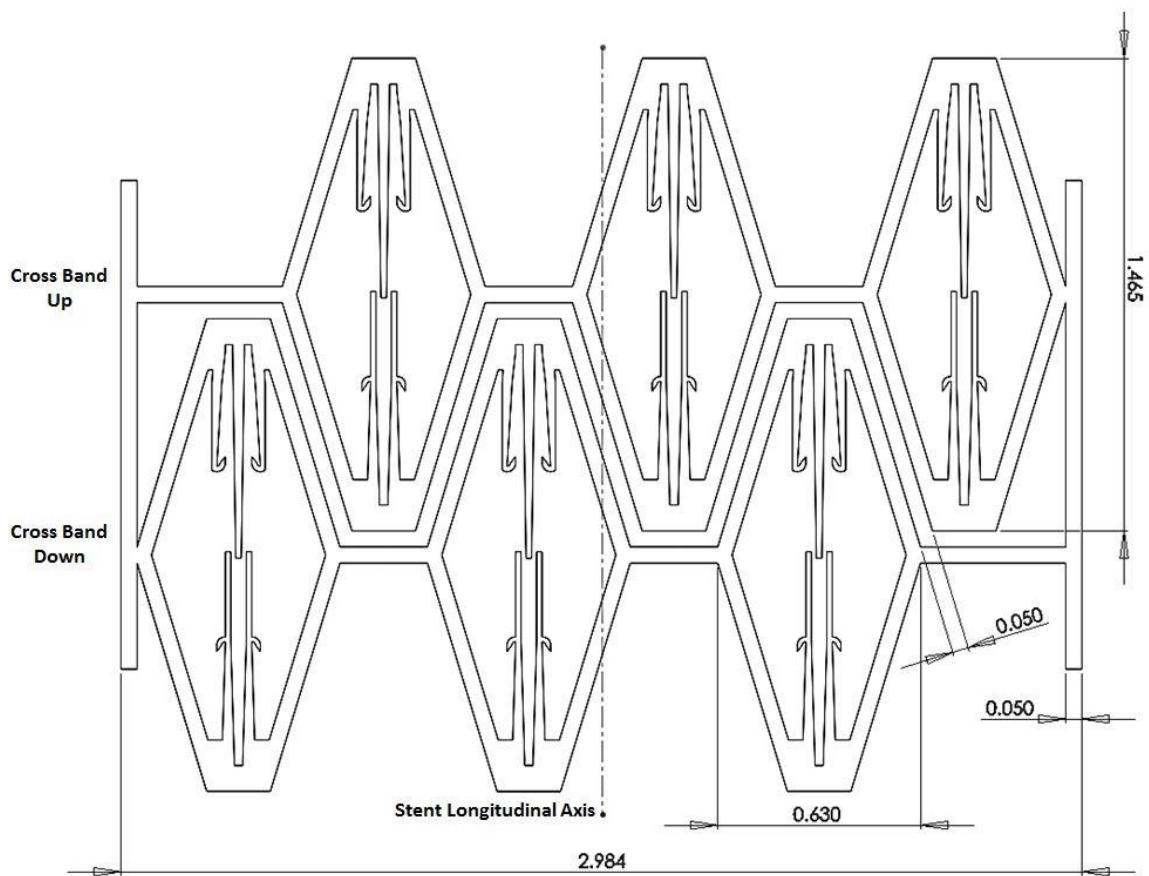


Figure 5-1. Schematic depiction of a portion of the planar hex stent design. All units in millimeters

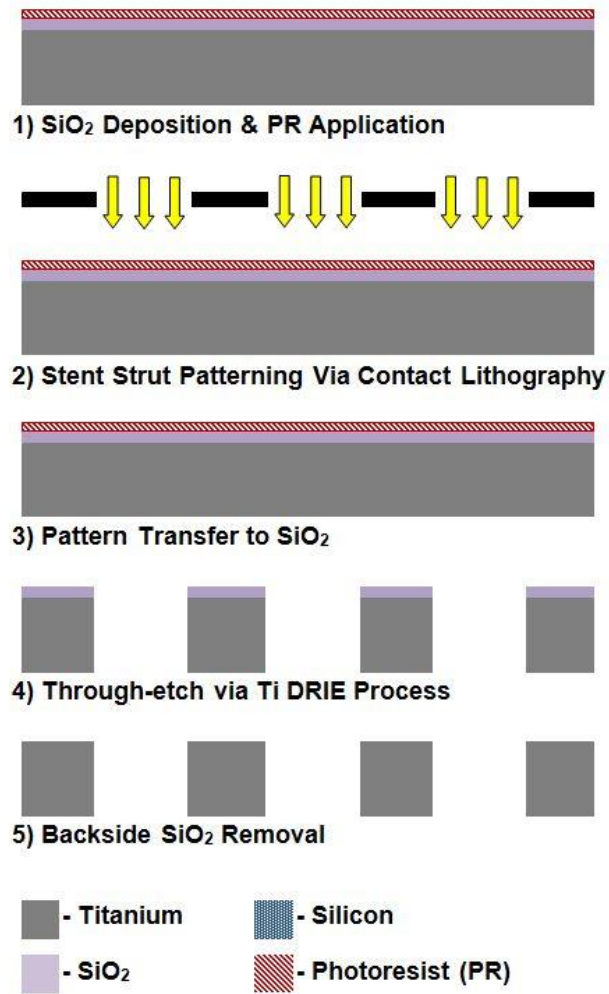


Figure 5-2. Fabrication process flow for surface-patterned planar Ti stent forms.

5.2.2. Fabrication

Using our recently developed Ti DRIE processes the hex design stents were created in double-side polished 80 μm thick Grade 1 CP-Ti foil substrates (99.6% Ti, Tokyo Stainless Grinding Co., Ltd, Japan). This foil thickness was chosen for being within the range of current stents (Garg and Serruys 2010). As shown in Figure 5-3, the fabrication consisted of contact lithography and Ti DRIE and produces a planar stent form ready for threading and balloon-mounting. No surface patterning was added to this effort as in previous studies because of the focus of this work is solely on stent design as it is related to radial stiffness response.

Processing (Figure 5-2) began with solvent cleaning of the substrates, followed by ICP PECVD deposition of a 4.2 μm thick SiO_2 etch mask. The substrates were then dehydration baked, followed by HMDS priming. Afterwards, PR was applied via spin-coating (AZnLOF 2070, Clariant, Muttenz, Switzerland). The resist was then patterned using contact lithography (MJB 3 UV400, Suss MicroTec, Germany). The resist pattern was transferred into the underlying SiO_2 by fluorine-based dry etching (E620-R&D; Process conditions: 37.5 mT chamber pressure, 900 W ICP source power, 100 W substrate power, 40 sccm CHF_3), followed by solvent cleaning to remove residual resist. Transfer of the mask oxide pattern through the underlying Ti substrate was then performed using a modified Ti DRIE process (E620-R&D; Process conditions: 15 mT chamber pressure, 400 W ICP source power, 100 W substrate power, 100 sccm Cl_2 , 5 sccm Ar, and 1 sccm O_2). Finally, residual mask oxide was removed using fluorine-based dry etching (E620-R&D;

Process conditions: 7.5 mT chamber pressure, 600 W ICP source power, 50 W substrate power, 50 sccm SF₆, and 10 sccm Ar).

5.2.3. Finite Element Analysis

Elastoplastic FEA was used to simulate: a single link comparison of between Ti locking hex, Ti involute, and L605 cobalt-chromium (CoCr) commercial stent designs. Previously, we used uniaxial compression testing to experimentally test the mechanical response of Ti involute stents relative to commercially available stents. While this is a viable method, it does not truly capture the more complex loading situations present in the body as would radial compression, which is now a standard in stent testing. Also, as uniaxial loading basically measures the bending stiffness in concentrated areas 90° from the parallel compression platens, it would not accurately engage hooks and testing the locking mechanisms in a meaningful way. In the absence of an experimental method available to us that can uniformly radially compress the stents, single links of the stent designs were evaluated in a way that mimics the deformations they would experience under radial compression. From this, a relative measure of resistance to radial force can be made for each design.

All simulations were performed using a commercial FEA package (Femap with NX Nastran Advanced Nonlinear, Siemens PLM, Cypress, CA). Using a bilinear material model, our previous study of stent uniaxial compression closely approximated the elastic response, but deviated when nearing and entering the plastic region. To better approximate the mechanical response, tensile tests were performed to collect stress-strain data from the

80 μm DSP Grade 1 Ti. Results applying the new material properties to our previous involute design showed improvement over the bilinear model, with agreement in elastic and plastic region with the experimental (see Appendix G). Hence, this material curve was applied to our Ti design simulations. For the L605 CoCr commercial stent, a bilinear material model was assumed with the following properties: Young's modulus = 243 GPa; Poisson's ratio = 0.3; density = 9.1 g/cm^3 ; yield strength = 500 MPa; ultimate tensile strength = 1000 MPa (O'Brien *et al.* 2010). A tabulated value for tangent modulus could not be found in the literature, thus an estimated value of 1.965 GPa was used. This value was based upon the average slope of the stress-strain curve within the plastic deformation regime.

For all simulations, the stent geometry was simplified to a single link within a cross-band. Both Ti involute and hex design dimensions were reproduced in Femap as shown in Figures 4-1 and 5-1. Since commercial stent design is largely proprietary, the commercial stent link dimensions were measured and reproduced for simulation to the best of our ability. Both Ti stent and the commercial stent designs consisted of 3 links per 180° of stent circumference. This, as well as the fact that all stents were 80 μm thick, made for easy link-to-link comparisons.

For each single link, deployment (from its crimped geometry to the equivalent of a 3 mm diameter stent) and compression were simulated by fixing one link end and applying a uniaxial prescribed displacement to the free end. Because the commercial stent has a smaller crimped diameter, it requires a larger displacement to reach 3 mm. Similar mesh densities were used for all simulations, and consisted of four hex elements through

the thickness. Additionally, frictionless contact was assumed for the hex stent. Extraction of load-displacement data from the simulation by summing the nodal forces on the free link end allowed determination of radial stiffness and overall mechanical response of the stents.

5.3. Results and Discussion

5.3.1. Fabrication

Figure 5-3 shows SEM micrographs of the successful fabrication and deployment of a Ti hex stent. The anisotropic nature of our Ti DRIE processes is especially noticed in the definition of the hooks, where lateral etching of smaller features would be apparent. Figure 5-3b illustrates the ability to use conventional angioplasty techniques to deploy planar stents to the correct shape and diameter, with the inset highlighting the ability of the guides to lead the complementary hooks to engage. Depending on how the stent was handled, however, some of the stent hooks would not pair with each other, so further work should be done to improve the locking mechanism robustness and tracking.

5.3.2. FEA Mechanical Response

Table 5-1 qualitatively shows the different stages of link deformation during the FEA analysis (initial configuration, deployment, and compression), while Figures 5-4 and 5-5 quantitatively summarizes the deployment and compression mechanical response for each stent design. As was established in previous studies, the involute has a much lower

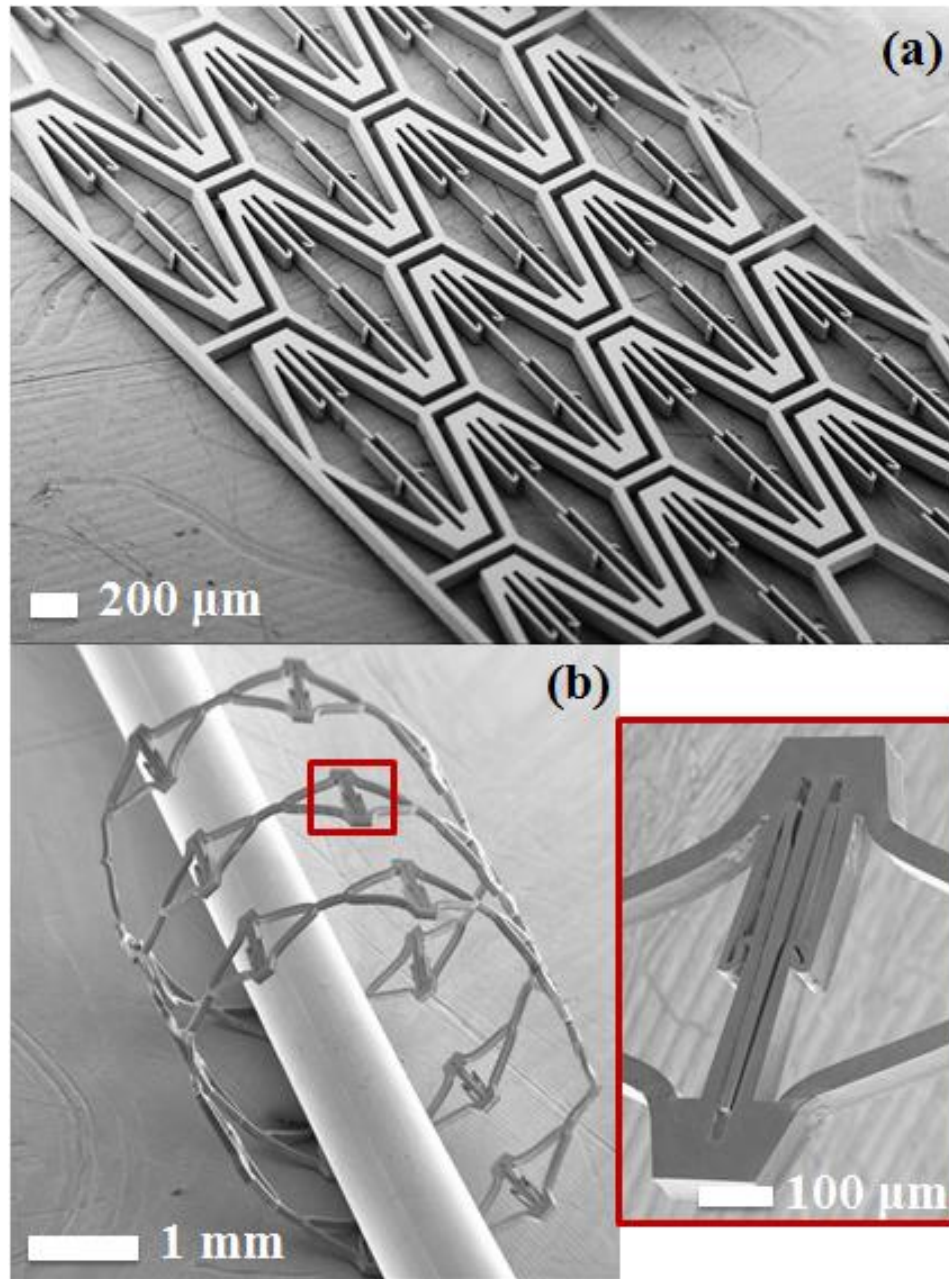


Figure 5-3. SEM micrographs of the Ti hex stent transformation after fabrication: a) Planar hex stent deep etched through an 80 μm thick Ti substrate; b) Hex stent after balloon deployment to 3 mm diameter, inset: higher magnification of single hex link showing locking hooks.


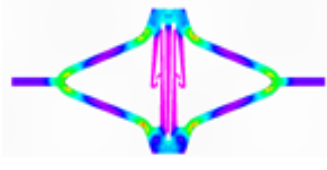
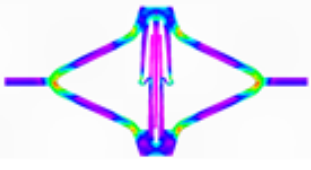

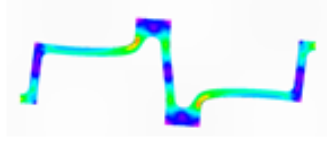


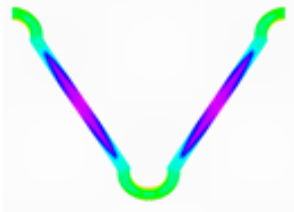
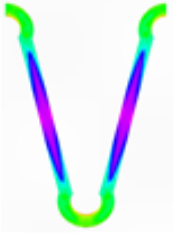
	Initial Configuration	Deployment	Compression
Ti Hex Stent			
Ti Involute Stent			
L605 CoCr Commercial Stent			

Table 5-1. Representation of the progressive link deformation during FEA.

Deployment Response for Single Link

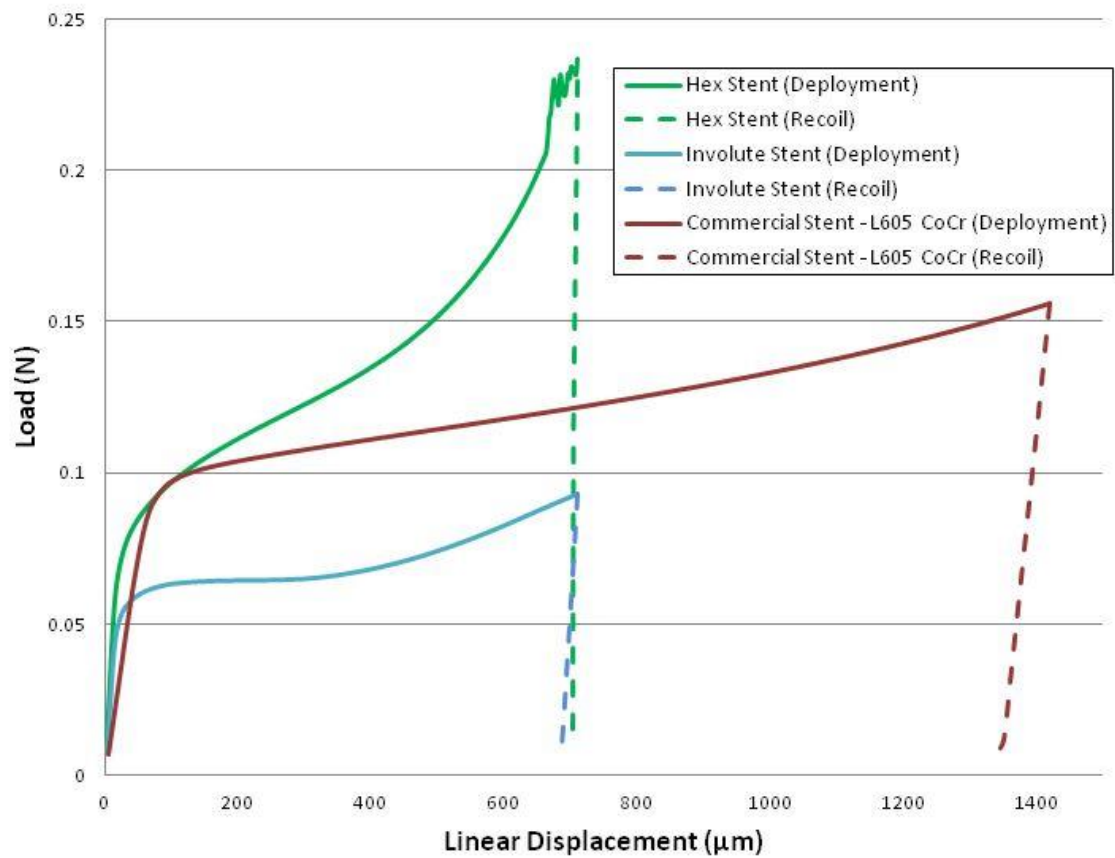


Figure 5-4. FEA deployment response for single link of Ti hex, Ti involute, and commercial stent designs.

Compression Response for Single Link

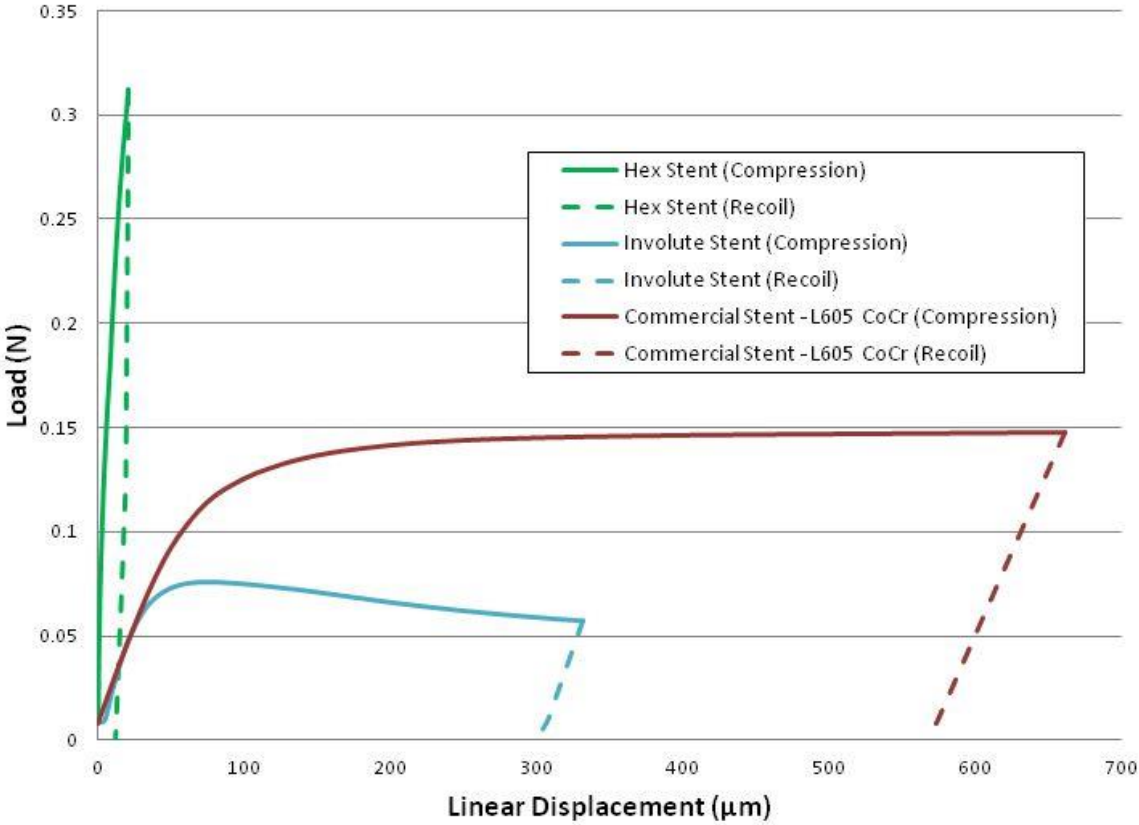


Figure 5-5. FEA compression response for single link of Ti hex, Ti involute and commercial stent designs.

yield point and softer response than the commercial stent during deployment and compression. The hex, however, has a comparable yield point to the commercial during deployment and requires higher forces as the hooks move past each other to engage. Also, the hex has a significantly higher stiffness than the commercial stent upon compression, as this represents the stent physically locked into place by the hooks. Each had differing amounts of recoil, but the trends were the same: After Deployment: {hex ($\sim 7 \mu\text{m}$), involute ($\sim 19 \mu\text{m}$), and commercial ($\sim 69 \mu\text{m}$)} and After Compression: {hex ($\sim 9 \mu\text{m}$), involute ($\sim 24 \mu\text{m}$), and commercial ($\sim 79 \mu\text{m}$)}. Stiffness, indicated by the slope of the initial linear region, is slightly lower for the commercial stent during deployment and may be due to the assumed bilinear model or the simplicity of commercial geometry. Despite this unexpected result, the overwhelmingly stiffer response from the hex stent during compression suggests that it would still meet, if not exceed the stiffness of the commercial stent.

We have now shown feasibility of the Ti hex stent design through fabrication, and, with FEA, the potential for in-plane locking mechanisms to boost the radial stiffness of Ti stents to surpass that of commercial stents. From the recoil data, we can see that the hex design minimizes the elastic recoil over the other two designs, which would help prevent separation of the stent from the vessel wall. The hex design compression results represent one stiffness extreme and it is presumed that if a lower stiffness is desired, some combination of hooks or arrangement of hook spacing would allow for a lower or progressive stiffness result. Overall, this result is very encouraging as it provides one step closer to our long-term goal of a pro-healing Ti stent design.

6 CONCLUSIONS

The fabrication of precisely-defined, grating-based patterns on planar bulk Ti and Si substrates with groove widths ranging from 0.5 – 50 μm is demonstrated. *In vitro* studies evaluating HEC adhesion, proliferation, morphology, and functionality on these substrates have shown favorable trending of cellular response with decreasing feature size on the patterned Ti substrates. These studies have also shown that patterning similarly enhances HEC response on Si substrates, although to a lesser extent than comparably-patterned Ti. Collectively, these results looking into the cell-substrate interaction suggest promise for using sub-micrometer topographic patterning to enhance the safety, efficacy, and performance of implantable microdevices based on these substrate materials. Moreover, these results particularly highlight the potential superiority of sub-micrometer patterned Ti for such applications, thus motivating the development of smaller surface patterning and its integration with vascular stenting.

In light of this, the design, fabrication, simulation, and mechanical testing of the first balloon-deployable, metallic vascular stents with rationally-designed, deep sub-micrometer scale surface patterning is reported. These devices were motivated by the potential embodied in surface patterning to address lingering safety and efficacy concerns associated with current coronary stents. Their realization was made possible through integration of our novel Ti DRIE capability with previously reported techniques for transforming micromachined planar structures into cylindrical stents, as well as the significant advancement of the minimum feature size capability of the Ti DRIE process itself to yield 0.15 μm width features. Elastoplastic FEA models created to simulate both stent deployment and uniaxial radial compression show good agreement with experiments,

thus providing opportunity for expediting future design improvement. While these efforts represent key steps towards our long-term goal of developing a new paradigm for coronary stents, the potential prohealing capabilities afforded by surface patterning may benefit other stent-based applications as well (e.g., revascularization of stenosed carotid, renal, & peripheral arteries; repair of abdominal aortic, thoracic aortic, & neurovascular aneurysms; and transcatheter aortic valve replacement). This, therefore, suggests potential for considerable impact in the field of vascular intervention.

With the developed elastoplastic models and the introduction of new Ti foil stress-strain data to replace the bilinear approximations, stent designs with novel locking mechanisms are explored in order to increase the radial stiffness upon compression. Side-by-side FEA comparisons of the Ti involute, Ti locking hex, and CoCr commercial stent designs show significantly higher resistive forces for the Ti locking hex when compressing a single link. Based on the accuracy of our previous models to estimate experimental results, it is likely higher simulation forces will translate into higher experimental radial stiffness for the Ti locking hex design. Toward this, the Ti DRIE capability enabled the fabrication of the Ti locking hex stents and efforts to test them are underway.

6.1. Recommendations for Future Work

Despite the promising results demonstrated in the current study, it is important to briefly acknowledge potential limitations of this study, and the surface patterned stent concept in general. First, it is clear that further evaluation of the mechanical response is

required to accurately model expected conditions *in vivo* (e.g., uniform rather than uniaxial radial compression testing). This is especially true for the locking hex stent, to accurately test the locking mechanisms. Second, since pulsatile vessel dilation *in vivo* may subject a typical stent to upwards of 10^7 loading cycles over its service life, it is important to consider the potential for surface patterning to act as an initiation site for fatigue-based failure. Testing under physiologically-relevant conditions will be required to accurately assess this risk. However, stresses under such conditions are likely to be far lower than the fatigue strength, which is typically on the order of half the tensile strength (Niinomi 1998), thus suggesting that this may not be a significant concern. Lastly, while minimal damage to the surface patterning was observed here, this is an important issue that must be studied further. However, it is conceivable that deep sub-micrometer scale surface patterns may possess enhanced resistance to plasticity, due to their diminutive dimensions. This hypothesis is based upon recent studies that have demonstrated flow stresses significantly exceeding the bulk yield strength for Ti structures with sub-micrometer scale dimensions (Sun *et al.* 2011; Yu *et al.* 2012; Yu *et al.* 2010).

Additional refinements may also help improve agreement of the FEA simulations with the current experimental data, thus further facilitating any future design efforts. For example, use of a finer mesh could reduce potential for excessive localization of plasticity within a few large elements. While this would come at the expense of increased computation time, this could resolve the anomalous buckling-induced softening that is currently predicted by the simulation within the initial portion of the plastic deformation regime.

Further cell studies are also needed to pinpoint the best groove dimensions to promote healing. This work has shown that there is an increasing favorable response from ECs with decreasing feature size down to 0.5 μm , but due to time constraints extension of those studies to our smaller features was precluded. As such, similar EC studies should be continued on Ti patterning down to 0.15 μm to assess the plateau of the positive response (expected to be around the size of collagen fibrils that comprise the extracellular matrix, e.g. 260 – 410 nm (Bozec *et al.* 2007)). Also, to assess the interactions of vascular smooth muscle cells to this feature size range in a monoculture as well as a competitive co-culture environment with ECs would give insight into the cell-cell and cell-topography interactions that could aid in designing stent topography to mitigate restenosis.

BIBLIOGRAPHY

- Aimi, M. F., Rao, M. P., Macdonald, N. C., Zuruza, A. S., and Bothman, D. P., "High-Aspect-Ratio Bulk Micromachining of Titanium," *Nature Materials*, vol. 3, pp. 103-105, Feb 2004.
- Anselme, K. and Bigerelle, M., "Role of Materials Surface Topography on Mammalian Cell Response," *International Materials Reviews*, vol. 56, pp. 243-266, Jul 2011.
- Asahara, T., Bauters, C., Pastore, C., Kearney, M., Rossow, S., Bunting, S., Ferrara, N., Symes, J. F., and Isner, J. M., "Local-Delivery of Vascular Endothelial Growth-Factor Accelerates Reendothelialization and Attenuates Intimal Hyperplasia in Balloon-Injured Rat Carotid-Artery," *Circulation*, vol. 91, pp. 2793-2801, Jun 1995.
- Balamurugan, A., Rajeswari, S., Balossier, G., Rebelo, A. H. S., and Ferreira, J. M. F., "Corrosion Aspects of Metallic Implants - an Overview," *Materials and Corrosion-Werkstoffe Und Korrosion*, vol. 59, pp. 855-869, Nov 2008.
- Balasundaram, G. and Webster, T. J., "A Perspective on Nanophase Materials for Orthopedic Implant Applications," *Journal of Materials Chemistry*, vol. 16, pp. 3737-3745, 2006.
- Barbucci, R., Pasqui, D., Wirsén, A., Affrossman, S., Curtis, A., and Tetta, C., "Micro and Nano-Structured Surfaces," *Journal of Materials Science-Materials in Medicine*, vol. 14, pp. 721-725, Aug 2003.
- Belvisi, L., Riccioni, T., Marcellini, M., Vesce, L., Chiarucci, I., Efrati, D., Potenza, D., Scolastico, C., Manzoni, L., Lombardo, K., Stasi, M. A., Orlandi, A., Ciucci, A., Nico, B., Ribatti, D., Giannini, G., Presta, M., Carminati, P., and Pisano, C., "Biological and Molecular Properties of a New Alpha(V)Beta(3)/Alpha(V)Beta(5) Integrin Antagonist," *Molecular Cancer Therapeutics*, vol. 4, pp. 1670-1680, Nov 2005.
- Bettinger, C. J., Langer, R., and Borenstein, J. T., "Engineering Substrate Topography at the Micro- and Nanoscale to Control Cell Function," *Angewandte Chemie-International Edition*, vol. 48, pp. 5406-5415, 2009.
- Bettinger, C. J., Orrick, B., Misra, A., Langer, R., and Borenstein, J. T., "Micro Fabrication of Poly (Glycerol-Sebacate) for Contact Guidance Applications," *Biomaterials*, vol. 27, pp. 2558-2565, Apr 2006.

- Bettinger, C. J., Zhang, Z. T., Gerecht, S., Borenstein, J. T., and Langer, R., "Enhancement of in Vitro Capillary Tube Formation by Substrate Nanotopography," *Advanced Materials*, vol. 20, pp. 99-+, Jan 2008.
- Biela, S. A., Su, Y., Spatz, J. P., and Kemkemer, R., "Different Sensitivity of Human Endothelial Cells, Smooth Muscle Cells and Fibroblasts to Topography in the Nano-Micro Range," *Acta Biomaterialia*, vol. 5, pp. 2460-2466, Sep 2009.
- Biggs, M. J. P., Richards, R. G., and Dalby, M. J., "Nanotopographical Modification: A Regulator of Cellular Function through Focal Adhesions," *Nanomedicine-Nanotechnology Biology and Medicine*, vol. 6, pp. 619-633, Oct 2010.
- Bjorkerud, S. and Bondjers, G., "Arterial Repair and Atherosclerosis after Mechanical Injury .5. Tissue Response after Induction of a Large Superficial Transverse Injury," *Atherosclerosis*, vol. 18, pp. 235-255, 1973.
- Bozec, L., van der Heijden, G., and Horton, M., "Collagen Fibrils: Nanoscale Ropes," *Biophysical Journal*, vol. 92, pp. 70-75, Jan 2007.
- Brown, A., Burke, G., and Meenan, B. J., "Modeling of Shear Stress Experienced by Endothelial Cells Cultured on Microstructured Polymer Substrates in a Parallel Plate Flow Chamber," *Biotechnology and Bioengineering*, vol. 108, pp. 1148-1158, May 2011.
- Brunette, D. M., *Titanium in Medicine: Material Science, Surface Science, Engineering, Biological Responses, and Medical Applications*: Springer, 2001.
- Bryukhanov, A. A., Voitenko, A. F., Usov, V. V., and Chernyi, A. A., "Anisotropy of the Elastic and Strength Properties of Cold-Rolled Copper Sheets," *Strength of Materials*, vol. 11, pp. 914-917, Aug. 1979.
- Burton, R. H. and Smolinsky, G., "Ccl4 and Cl-2 Plasma-Etching of Iii-V-Semiconductors and the Role of Added O-2," *Journal of the Electrochemical Society*, vol. 129, pp. 1599-1604, 1982.
- Buttiglieri, S., Pasqui, D., Migliori, M., Johnstone, H., Affrossman, S., Sereni, L., Wratten, M. L., Barbucci, R., Tetta, C., and Camussi, G., "Endothelization and Adherence of Leucocytes to Nanostructured Surfaces," *Biomaterials*, vol. 24, pp. 2731-2738, Jul 2003.
- Callister, W. D., *Materials Science and Engineering: An Introduction*: John Wiley & Sons, 2007.

- Carlstrom, C. F., van der Heijden, R., Karouta, F., van der Heijden, R. W., Salemink, H. W. M., and van der Drift, E., "Cl-2/O-2-Inductively Coupled Plasma Etching of Deep Hole-Type Photonic Crystals in Inp," *Journal of Vacuum Science & Technology B*, vol. 24, pp. L6-L9, Jan-Feb 2006.
- Choudhary, S., Berhe, M., Haberstroh, K. M., and Webster, T. J., "Increased Endothelial and Vascular Smooth Muscle Cell Adhesion on Nanostructured Titanium and CoCrMo," *International Journal of Nanomedicine*, vol. 1, pp. 41-49, 2006.
- Chung, T. W., Liu, D. Z., Wang, S. Y., and Wang, S. S., "Enhancement of the Growth of Human Endothelial Cells by Surface Roughness at Nanometer Scale," *Biomaterials*, vol. 24, pp. 4655-4661, Nov 2003.
- Clowes, A. W., Collazzo, R. E., and Karnovsky, M. J., "Morphologic and Permeability Study of Luminal Smooth-Muscle Cells after Arterial Injury in Rat," *Laboratory Investigation*, vol. 39, pp. 141-150, 1978.
- Coburn, J. W. and Winters, H. F., "Conductance Considerations in the Reactive Ion Etching of High Aspect Ratio Features," *Applied Physics Letters*, vol. 55, pp. 2730-2732, Dec 1989.
- Dalby, M. J., Riehle, M. O., Johnstone, H., Affrossman, S., and Curtis, A. S. G., "In Vitro Reaction of Endothelial Cells to Polymer Demixed Nanotopography," *Biomaterials*, vol. 23, pp. 2945-2954, Jul 2002.
- Danner, D. A. and Hess, D. W., "The Reaction of Atomic and Molecular Chlorine with Aluminum," *Journal of Vacuum Science & Technology a-Vacuum Surfaces and Films*, vol. 4, pp. 748-748, May-Jun 1986.
- Davies, M. J., Gordon, J. L., Gearing, A. J. H., Pigott, R., Woolf, N., Katz, D., and Kyriakopoulos, A., "The Expression of the Adhesion Molecules Icam-1, Vcam-1, Pecam, and E-Selectin in Human Atherosclerosis," *Journal of Pathology*, vol. 171, pp. 223-229, Nov 1993.
- Di Rienzo, C., Jacchetti, E., Cardarelli, F., Bizzarri, R., Beltram, F., and Cecchini, M., "Unveiling Lox-1 Receptor Interplay with Nanotopography: Mechanotransduction and Atherosclerosis Onset," *Scientific Reports*, vol. 3, p. 8, Jan 2013.
- Dibra, A., Kastrati, A., Mehilli, J., Pache, J., von Oepen, R., Dirschinger, J., and Schomig, A., "Influence of Stent Surface Topography on the Outcomes of Patients Undergoing Coronary Stenting: A Randomized Double-Blind Controlled Trial," *Catheterization and Cardiovascular Interventions*, vol. 65, pp. 374-380, Jul 2005.

- Dubey, A. K. and Yadava, V., "Laser Beam Machining - a Review," *International Journal of Machine Tools & Manufacture*, vol. 48, pp. 609-628, May 2008.
- Duda, S. H., Wiskirchen, J., Tepe, G., Bitzer, M., Kaulich, T. W., Stoeckel, D., and Claussen, C. D., "Physical Properties of Endovascular Stents: An Experimental Comparison," *Journal of Vascular and Interventional Radiology*, vol. 11, pp. 645-654, May 2000.
- Dvir, T., Timko, B. P., Kohane, D. S., and Langer, R., "Nanotechnological Strategies for Engineering Complex Tissues," *Nature Nanotechnology*, vol. 6, pp. 13-22, Jan 2011.
- Dyet, J. F., Watts, W. G., Ettles, D. F., and Nicholson, A. A., "Mechanical Properties of Metallic Stents: How Do These Properties Influence the Choice of Stent for Specific Lesions?," *Cardiovascular and Interventional Radiology*, vol. 23, pp. 47-54, Jan-Feb 2000.
- Edell, D. J., Toi, V. V., McNeil, V. M., and Clark, L. D., "Factors Influencing the Biocompatibility of Insertable Silicon Microshafts in Cerebral-Cortex," *Ieee Transactions on Biomedical Engineering*, vol. 39, pp. 635-643, Jun 1992.
- Edelman, E. R. and Rogers, C., "Pathobiologic Responses to Stenting," *American Journal of Cardiology*, vol. 81, pp. 4E-6E, Apr 1998.
- Elter, P., Lange, R., and Beck, U., "Atomic Force Microscopy Studies of the Influence of Convex and Concave Nanostructures on the Adsorption of Fibronectin," *Colloids and Surfaces B-Biointerfaces*, vol. 89, pp. 139-146, Jan 2012.
- Farra, R., Sheppard, N. F., McCabe, L., Neer, R. M., Anderson, J. M., Santini, J. T., Cima, M. J., and Langer, R., "First-in-Human Testing of a Wirelessly Controlled Drug Delivery Microchip," *Science Translational Medicine*, vol. 4, p. 10, Feb 2012.
- Fishman, J. A., Ryan, G. B., and Karnovsky, M. J., "Endothelial Regeneration in Rat Carotid-Artery and Significance of Endothelial Denudation in Pathogenesis of Myointimal Thickening," *Laboratory Investigation*, vol. 32, pp. 339-351, 1975.
- Flueckiger, F., Sternthal, H., Klein, G. E., Aschauer, M., Szolar, D., and Kleinhapfl, G., "Strength, Elasticity, and Plasticity of Expandable Metal Stents - in-Vitro Studies with 3 Types of Stress," *Journal of Vascular and Interventional Radiology*, vol. 5, pp. 745-750, Sep-Oct 1994.

- Franco, D., Klingauf, M., Bednarzik, M., Cecchini, M., Kurtcuoglu, V., Gobrecht, J., Poulidakos, D., and Ferrari, A., "Control of Initial Endothelial Spreading by Topographic Activation of Focal Adhesion Kinase," *Soft Matter*, vol. 7, pp. 7313-7324, 2011.
- Fuss, C., Sprague, E. A., Bailey, S. R., and Palmaz, J. C., "Surface Micro Grooves (Mg) Improve Endothelialization Rate in Vitro and in Vivo," *Journal of the American College of Cardiology*, vol. 37, pp. 70A-70A, Feb 2001.
- Garg, S. and Serruys, P. W., "Coronary Stents: Current Status," *Journal of the American College of Cardiology*, vol. 56, pp. S1-S42, Aug 2010.
- Gasiorowski, J. Z., Liliensiek, S. J., Russell, P., Stephan, D. A., Nealey, P. F., and Murphy, C. J., "Alterations in Gene Expression of Human Vascular Endothelial Cells Associated with Nanotopographic Cues," *Biomaterials*, vol. 31, pp. 8882-8888, Dec.
- Gerhard, W., Boyer, R., and Collings, E. W., *Materials Properties Handbook: Titanium Alloys*. Ohio: Asm International, 1994.
- Gott, S. C., Jabola, B. A., Xu, G., and Rao, M. P., "Vascular Stents with Rationally-Designed Surface Patterning," in *IEEE Engineering in Medicine & Biology Society* San Diego, CA, 2012.
- Gray, D. S., Tien, J., and Chen, C. S., "Repositioning of Cells by Mechanotaxis on Surfaces with Micropatterned Young's Modulus," *Journal of Biomedical Materials Research Part A*, vol. 66A, pp. 605-614, Sep 2003.
- Gurbel, P. A., Bliden, K. P., Hiatt, B. L., and O'Connor, C. M., "Clopidogrel for Coronary Stenting: Response Variability, Drug Resistance, and the Effect of Pretreatment Platelet Reactivity," *Circulation*, vol. 107, pp. 2908-2913, June 17, 2003 2003.
- Halliday, D., Resnick, R., and Walker, J., *Fundamentals of Physics, 6th Ed*: Wiley India Pvt. Limited, 2006.
- Haudenschild, C. C. and Schwartz, S. M., "Endothelial Regeneration .2. Restitution of Endothelial Continuity," *Laboratory Investigation*, vol. 41, pp. 407-418, 1979.
- Hirai, Y., Yoshida, S., and Takagi, N., "Defect Analysis in Thermal Nanoimprint Lithography," *Journal of Vacuum Science & Technology B*, vol. 21, pp. 2765-2770, Nov-Dec 2003.

- Hopcroft, M. A., Nix, W. D., and Kenny, T. W., "What Is the Young's Modulus of Silicon?," *Journal of Microelectromechanical Systems*, vol. 19, pp. 229-238, Apr 2010.
- Hwang, S. J., Ballantyne, C. M., Sharrett, A. R., Smith, L. C., Davis, C. E., Gotto, A. M., and Boerwinkle, E., "Circulating Adhesion Molecules Vcam-1, Icam-1, and E-Selectin in Carotid Atherosclerosis and Incident Coronary Heart Disease Cases - the Atherosclerosis Risk in Communities (Aric) Study," *Circulation*, vol. 96, pp. 4219-4225, Dec 1997.
- Hwang, S. Y., Kwon, K. W., Jang, K. J., Park, M. C., Lee, J. S., and Suh, K. Y., "Adhesion Assays of Endothelial Cells on Nanopatterned Surfaces within a Microfluidic Channel," *Analytical Chemistry*, vol. 82, pp. 3016-3022, Apr 2010.
- Jiang, X. Y., Takayama, S., Qian, X. P., Ostuni, E., Wu, H. K., Bowden, N., LeDuc, P., Ingber, D. E., and Whitesides, G. M., "Controlling Mammalian Cell Spreading and Cytoskeletal Arrangement with Conveniently Fabricated Continuous Wavy Features on Poly(Dimethylsiloxane)," *Langmuir*, vol. 18, pp. 3273-3280, Apr 2002.
- Kathuria, Y. P., "Laser Microprocessing of Metallic Stent for Medical Therapy," *Journal of Materials Processing Technology*, vol. 170, pp. 545-550, Dec 2005.
- Kirchengast, M. and Munter, K., "Endothelin and Restenosis," *Cardiovascular Research*, vol. 39, pp. 550-555, Sep 1998.
- Lau, W. C., Gurbel, P. A., Watkins, P. B., Neer, C. J., Hopp, A. S., Carville, D. G. M., Guyer, K. E., Tait, A. R., and Bates, E. R., "Contribution of Hepatic Cytochrome P450 3a4 Metabolic Activity to the Phenomenon of Clopidogrel Resistance," *Circulation*, vol. 109, pp. 166-171, January 20, 2004 2004.
- Le Saux, G., Magenau, A., Boecking, T., Gaus, K., and Gooding, J. J., "The Relative Importance of Topography and Rgd Ligand Density for Endothelial Cell Adhesion," *Plos One*, vol. 6, p. 13, Jul 2011.
- Liliensiek, S. J., Wood, J. A., Yong, J. A., Auerbach, R., Nealey, P. F., and Murphy, C. J., "Modulation of Human Vascular Endothelial Cell Behaviors by Nanotopographic Cues," *Biomaterials*, vol. 31, pp. 5418-5426, Jul 2010.
- Lu, J., Rao, M. P., MacDonald, N. C., Khang, D., and Webster, T. J., "Improved Endothelial Cell Adhesion and Proliferation on Patterned Titanium Surfaces with Rationally Designed, Micrometer to Nanometer Features," *Acta Biomaterialia*, vol. 4, pp. 192-201, Jan 2008.

- Lu, J., Rao, M. P., MacDonald, N. C., and Webster, T. J., Boston, MA: Materials Research Society Fall Meeting, 2007.
- Luetjering, G. and Williams, J. C., *Titanium*: Springer, 2007.
- Luong-Van, E., Rodriguez, I., Low, H. Y., Elmouelhi, N., Lowenhaupt, B., Natarajan, S., Lim, C. T., Prajapati, R., Vyakarnam, M., and Cooper, K., "Review: Micro- and Nanostructured Surface Engineering for Biomedical Applications," *Journal of Materials Research*, vol. 28, pp. 165-174, Jan 2013.
- Mackay, J., Mensah, G. A., Mendis, S., and Greenlund, K., *The Atlas of Heart Disease and Stroke*: World Health Organization, 2004.
- Madou, M. J., *Fundamentals of Microfabrication: The Science of Miniaturization, Second Edition*: Taylor & Francis, 2002.
- Martinez, A. W. and Chaikof, E. L., "Microfabrication and Nanotechnology in Stent Design," *Wiley Interdisciplinary Reviews-Nanomedicine and Nanobiotechnology*, vol. 3, pp. 256-268, May-Jun 2011.
- Marx, S. O., Totary-Jain, H., and Marks, A. R., "Vascular Smooth Muscle Cell Proliferation in Restenosis," *Circulation-Cardiovascular Interventions*, vol. 4, pp. 104-111, Feb 2011.
- MatWeb.com, 2014.
- McFadden, E. P., Stabile, E., Regar, E., Cheneau, E., Ong, A. T. L., Kinnaird, T., Suddath, W. O., Weissman, N. J., Torguson, R., Kent, K. M., Pichard, A. D., Satler, L. F., Waksman, R., and Serruys, P. W., "Late Thrombosis in Drug-Eluting Coronary Stents after Discontinuation of Antiplatelet Therapy," *Lancet*, vol. 364, pp. 1519-1521, Oct 2004.
- Miller, D. C., Thapa, A., Haberstroh, K. M., and Webster, T. J., "Endothelial and Vascular Smooth Muscle Cell Function on Poly(Lactic-Co-Glycolic Acid) with Nano-Structured Surface Features," *Biomaterials*, vol. 25, pp. 53-61, Jan 2004.
- Mitsumata, M., Fishel, R. S., Nerem, R. M., Alexander, R. W., and Berk, B. C., "Fluid Shear-Stress Stimulates Platelet-Derived Growth-Factor Expression in Endothelial-Cells," *American Journal of Physiology*, vol. 265, pp. H3-H8, Jul 1993.
- Morgan, J. T., Wood, J. A., Shah, N. M., Hughbanks, M. L., Russell, P., Barakat, A. I., and Murphy, C. J., "Integration of Basal Topographic Cues and Apical Shear

- Stress in Vascular Endothelial Cells," *Biomaterials*, vol. 33, pp. 4126-4135, Jun 2012.
- Murali, M. and Yeo, S. H., "Rapid Biocompatible Micro Device Fabrication by Micro Electro-Discharge Machining," *Biomedical Microdevices*, vol. 6, pp. 41-45, Mar 2004.
- Muthukrishnan, A. M., Amberiadis, K., and ElshabiniRiad, A., "Characterization of Titanium Etching in Cl-2/N-2 Plasmas," *Journal of the Electrochemical Society*, vol. 144, pp. 1780-1784, May 1997.
- Nagel, T., Resnick, N., Atkinson, W. J., Dewey, C. F., and Gimbrone, M. A., "Sheer Stress Selectively up-Regulates Intercellular-Adhesion Molecule-1 Expression in Cultured Human Vascular Endothelial-Cells," *Journal of Clinical Investigation*, vol. 94, pp. 885-891, Aug 1994.
- Nazneen, F., Herzog, G., Arrigan, D. W. M., Caplice, N., Benvenuto, P., Galvin, P., and Thompson, M., "Surface Chemical and Physical Modification in Stent Technology for the Treatment of Coronary Artery Disease," *Journal of Biomedical Materials Research Part B-Applied Biomaterials*, vol. 100B, pp. 1989-2014, Oct 2012.
- Nerem, R. M., Harrison, D. G., Taylor, W. R., and Alexander, R. W., "Hemodynamics and Vascular Endothelial Biology," *Journal of Cardiovascular Pharmacology*, vol. 21, pp. S6-S10, 1993.
- Neyt, M., Van Brabandt, H., Devriese, S., and De Laet, C., "Cost-Effectiveness Analyses of Drug Eluting Stents Versus Bare Metal Stents: A Systematic Review of the Literature," *Health Policy*, vol. 91, pp. 107-120, Jul 2009.
- Niinomi, M., "Mechanical Properties of Biomedical Titanium Alloys," *Materials Science and Engineering a-Structural Materials Properties Microstructure and Processing*, vol. 243, pp. 231-236, Mar 1998.
- O'Brien, B. J., Stinson, J. S., Larsen, S. R., Eppihimer, M. J., and Carroll, W. M., "A Platinum-Chromium Steel for Cardiovascular Stents," *Biomaterials*, vol. 31, pp. 3755-3761, May 2010.
- O'Donoghue, M. L., Braunwald, E., Antman, E. M., Murphy, S. A., Bates, E. R., Rozenman, Y., Michelson, A. D., Hautvast, R. W., Ver Lee, P. N., Close, S. L., Shen, L., Mega, J. L., Sabatine, M. S., and Wiviott, S. D., "Pharmacodynamic Effect and Clinical Efficacy of Clopidogrel and Prasugrel with or without a Proton-Pump Inhibitor: An Analysis of Two Randomised Trials," *The Lancet*, vol. 374, pp. 989-997, 2009/9/25/ 2009.

- O'Brien, K. D., McDonald, T. O., Chait, A., Allen, M. D., and Alpers, C. E., "Neovascular Expression of E-Selectin, Intercellular Adhesion Molecule-1, and Vascular Cell Adhesion Molecule-1 in Human Atherosclerosis and Their Relation to Intimal Leukocyte Content," *Circulation*, vol. 93, pp. 672-682, Feb 1996.
- Ohya, S., Kidoaki, S., and Matsuda, T., "Poly(N-Isopropylacrylamide) (Pnipam)-Grafted Gelatin Hydrogel Surfaces: Interrelationship between Microscopic Structure and Mechanical Property of Surface Regions and Cell Adhesiveness," *Biomaterials*, vol. 26, pp. 3105-3111, Jun 2005.
- Oliver, R. A., "Advances in Afm for the Electrical Characterization of Semiconductors," *Reports on Progress in Physics*, vol. 71, p. 37, Jul 2008.
- Onuma, Y. and Serruys, P. W., "Bioresorbable Scaffold the Advent of a New Era in Percutaneous Coronary and Peripheral Revascularization?," *Circulation*, vol. 123, pp. 779-797, Feb 2011.
- Parker, E. R., Thibeault, B. J., Aimi, M. F., Rao, M. P., and MacDonald, N. C., "Inductively Coupled Plasma Etching of Bulk Titanium for Mems Applications," *Journal of the Electrochemical Society*, vol. 152, pp. C675-C683, 2005.
- Rao, M. P., Lu, J., Aguilar, H. P., and MacDonald, N. C., "Rationally-Designed Surface Nanopatterning: A Potentially New Means for Enhancing Safety & Efficacy of Vacular Stents," in *Solid-State Sensors, Actuators, and Microsystems Workshop* Hilton Head Island, SC, 2008.
- Rao, M. P., Lu, J., Aguilar, H. P., and MacDonald, N. C., "Rationally-Designed Surface Nanopatterning: A Potentially New Means for Enhancing Safety & Efficacy of Vacular Stents," in *Solid-State Sensors, Actuators, and Microsystems Workshop*, Hilton Head Island, SC, 2008.
- Reinhart-King, C. A., Dembo, M., and Hammer, D. A., "The Dynamics and Mechanics of Endothelial Cell Spreading," *Biophysical Journal*, vol. 89, pp. 676-689, Jul 2005.
- Rieu, R., Barragan, P., Masson, C., Fuseri, J., Garitey, V., Silvestri, M., Roquebert, P., and Sainsous, J., "Radial Force of Coronary Stents: A Comparative Analysis," *Catheterization and Cardiovascular Interventions*, vol. 46, pp. 380-391, Mar 1999.
- Roger, V. L., Go, A. S., Lloyd-Jones, D. M., Adams, R. J., Berry, J. D., Brown, T. M., Camethon, M. R., Dai, S., de Simone, G., Ford, E. S., Fox, C. S., Fullerton, H. J., Gillespie, C., Greenlund, K. J., Hailpem, S. M., Heit, J. A., Ho, P. M., Howard, V.

- J., Kissela, B. M., Kittner, S. J., Lackland, D. T., Lichtman, J. H., Lisabeth, L. D., Makuc, D. M., Marcus, G. M., Marelli, A., Matchar, D. B., McDermott, M. M., Meigs, J. B., Moy, C. S., Mozaffarian, D., Mussolino, M. E., Nichol, G., Paynter, N. P., Rosamond, W. D., Sorlie, P. D., Stafford, R. S., Turan, T. N., Turner, M. B., Wong, N. D., and Wylie-Rosett, J., "Heart Disease and Stroke Statistics-2011 Update a Report from the American Heart Association," *Circulation*, vol. 123, pp. E18-E209, Feb 2011.
- Sakariassen, K. S., Bolhuis, P. A., and Sixma, J. J., "Human-Blood Platelet-Adhesion to Artery Subendothelium Is Mediated by Factor-Viii-Vonwillebrand Factor Bound to the Subendothelium," *Nature*, vol. 279, pp. 636-638, 1979.
- Salakhutdinov, I., VandeVord, P., Palyvoda, O., Matthew, H., Tatagiri, G., Handa, H., Mao, G., Auner, G. W., and Newaz, G., "Fibronectin Adsorption to Nanopatterned Silicon Surfaces," *Journal of Nanomaterials*, p. 5, 2008.
- Schmidt, S., Horch, K., and Normann, R., "Biocompatibility of Silicon-Based Electrode Arrays Implanted in Feline Cortical Tissue," *Journal of Biomedical Materials Research*, vol. 27, pp. 1393-1399, Nov 1993.
- Senturia, S. D., *Microsystem Design*: Springer US, 2005.
- Song, K. H., Kwon, K. W., Song, S., Suh, K. Y., and Doh, J., "Dynamics of T Cells on Endothelial Layers Aligned by Nanostructured Surfaces," *Biomaterials*, vol. 33, pp. 2007-2015, Mar 2011.
- Spertus, J. A., Kettelkamp, R., Vance, C., Decker, C., Jones, P. G., Rumsfeld, J. S., Messenger, J. C., Khanal, S., Peterson, E. D., Bach, R. G., Krumholz, H. M., and Cohen, D. J., "Prevalence, Predictors, and Outcomes of Premature Discontinuation of Thienopyridine Therapy after Drug-Eluting Stent Placement: Results from the Premier Registry," *Circulation*, vol. 113, pp. 2803-2809, June 20, 2006 2006.
- Sprague, E. A., Tio, F., Ahmed, S. H., Granada, J. F., and Bailey, S. R., "Impact of Parallel Micro-Engineered Stent Grooves on Endothelial Cell Migration, Proliferation, and Function an in Vivo Correlation Study of the Healing Response in the Coronary Swine Model," *Circulation-Cardiovascular Interventions*, vol. 5, pp. 499-507, Aug 2012.
- Sun, Q. Y., Guo, Q., Yao, X., Xiao, L., Greer, J. R., and Sun, J., "Size Effects in Strength and Plasticity of Single-Crystalline Titanium Micropillars with Prismatic Slip Orientation," *Scripta Materialia*, vol. 65, pp. 473-476, Sep 2011.

- Takahata, K. and Gianchandani, Y. B., "A Planar Approach for Manufacturing Cardiac Stents: Design, Fabrication, and Mechanical Evaluation," *Journal of Microelectromechanical Systems*, vol. 13, pp. 933-939, Dec 2004.
- Tay, C. Y., Irvine, S. A., Boey, F. Y. C., Tan, L. P., and Venkatraman, S., "Micro-/Nano-Engineered Cellular Responses for Soft Tissue Engineering and Biomedical Applications," *Small*, vol. 7, pp. 1361-1378, May 2011.
- Tengvall, P. and Lundstrom, I., "Physico-Chemical Considerations of Titanium as a Biomaterial," *Clinical Materials*, vol. 9, pp. 115-134, 1992.
- Uttayarat, P., Chen, M., Li, M., Allen, F. D., Composto, R. J., and Lelkes, P. I., "Microtopography and Flow Modulate the Direction of Endothelial Cell Migration," *American Journal of Physiology-Heart and Circulatory Physiology*, vol. 294, pp. H1027-H1035, Feb 2008.
- Uttayarat, P., Toworfe, G. K., Dietrich, F., Lelkes, P. I., and Composto, R. J., "Topographic Guidance of Endothelial Cells on Silicone Surfaces with Micro- to Nanogrooves: Orientation of Actin Filaments and Focal Adhesions," *Journal of Biomedical Materials Research Part A*, vol. 75A, pp. 668-680, Dec 2005.
- Vandragi, P., Gott, S. C., Rodgers, V. G. J., and Rao, M. P., "Comparative Endothelial Adhesion and Proliferation on Rationally Designed Nanopatterned Titanium and Silicon," 2012.
- Variola, F., Brunski, J. B., Orsini, G., de Oliveira, P. T., Wazen, R., and Nanci, A., "Nanoscale Surface Modifications of Medically Relevant Metals: State-of-the Art and Perspectives," *Nanoscale*, vol. 3, pp. 335-353, 2011.
- Ventre, M., Causa, F., and Netti, P. A., "Determinants of Cell-Material Crosstalk at the Interface: Towards Engineering of Cell Instructive Materials," *Journal of the Royal Society Interface*, vol. 9, pp. 2017-2032, Sep 2012.
- Virmani, R., Guagliumi, G., Farb, A., Musumeci, G., Grieco, N., Motta, T., Mihalecik, L., Tespili, M., Valsecchi, O., and Kolodgie, F. D., "Localized Hypersensitivity and Late Coronary Thrombosis Secondary to a Sirolimus-Eluting Stent: Should We Be Cautious?," *Circulation*, vol. 109, pp. 701-705, February 17, 2004 2004.
- Wallace, C. S., Strike, S. A., and Truskey, G. A., "Smooth Muscle Cell Rigidity and Extracellular Matrix Organization Influence Endothelial Cell Spreading and Adhesion Formation in Coculture," *American Journal of Physiology-Heart and Circulatory Physiology*, vol. 293, pp. H1978-H1986, Sep 2007.

- Wheeldon, I., Farhadi, A., Bick, A. G., Jabbari, E., and Khademhosseini, A., "Nanoscale Tissue Engineering: Spatial Control over Cell-Materials Interactions," *Nanotechnology*, vol. 22, p. 16, May 2011.
- Wi, J. S., Wilson, R. J., White, R. M., and Wang, S. X., "Gradual Pressure Release for Reliable Nanoimprint Lithography," *Journal of Vacuum Science & Technology B*, vol. 29, p. 3, May 2011.
- Wieneke, H., Dirsch, O., Sawitowski, T., Gu, Y. L., Brauer, H., Dahmen, U., Fischer, A., Wnendt, S., and Erbel, R., "Synergistic Effects of a Novel Nanoporous Stent Coating and Tacrolimus on Intima Proliferation in Rabbits," *Catheterization and Cardiovascular Interventions*, vol. 60, pp. 399-407, Nov 2003.
- Yeung, T., Georges, P. C., Flanagan, L. A., Marg, B., Ortiz, M., Funaki, M., Zahir, N., Ming, W. Y., Weaver, V., and Janmey, P. A., "Effects of Substrate Stiffness on Cell Morphology, Cytoskeletal Structure, and Adhesion," *Cell Motility and the Cytoskeleton*, vol. 60, pp. 24-34, Jan 2005.
- Yota, J., Hander, J., and Saleh, A. A., "A Comparative Study on Inductively-Coupled Plasma High-Density Plasma, Plasma-Enhanced, and Low Pressure Chemical Vapor Deposition Silicon Nitride Films," *Journal of Vacuum Science & Technology a-Vacuum Surfaces and Films*, vol. 18, pp. 372-376, Mar-Apr 2000.
- Yu, Q., Li, S. Z., Minor, A. M., Sun, J., and Ma, E., "High-Strength Titanium Alloy Nanopillars with Stacking Faults and Enhanced Plastic Flow," *Applied Physics Letters*, vol. 100, p. 4, Feb 2012.
- Yu, Q., Shan, Z. W., Li, J., Huang, X. X., Xiao, L., Sun, J., and Ma, E., "Strong Crystal Size Effect on Deformation Twinning," *Nature*, vol. 463, pp. 335-338, Jan 2010.
- Zorlutuna, P., Rong, Z., Vadgama, P., and Hasirci, V., "Influence of Nanopatterns on Endothelial Cell Adhesion: Enhanced Cell Retention under Shear Stress," *Acta Biomaterialia*, vol. 5, pp. 2451-2459, Sep 2009.
- Zuruqi, A. S., Yeo, Y. H., Monkowski, A. J., Ding, C. S., and MacDonald, N. C., "Superhydrophilicity on Microstructured Titanium Surfaces Via a Superficial Titania Layer with Interconnected Nanoscale Pores," *Nanotechnology*, vol. 24, p. 8, Jun 2013.

APPENDIX

Appendix A – Substrate Preparation

Before deposition or lithography on the substrate can be started, the as-received Ti and Si need to be cleaned and prepared. Whenever possible it is prudent to wear appropriate gloves and a mask, and keep all substrates covered in a clean sample holder when not actively processing to avoid dust or other particles getting to the substrate surface. Each time before processing, it is also wise to solvent clean all the implements to be used (e.g. tweezers, aluminum/glass dishes, etc.) or to blow them off with N₂ (e.g. pipettes, syringes, or filters, etc.) to ensure no cross-contamination. Rinse each of these compatible with solvent cleans in acetone, methanol, isopropanol, and DI water, followed by N₂ gun or absorbent wipe drying (Note: It is important not to pour acetone into a dish that is not completely dry because when water and acetone mix, they form a white film that can stick to the substrate and be difficult to remove). To ensure that nothing is transferred from the work surface to the substrate, place all items to be used on non-shedding wipes. Also, thoroughly clean each hotplate with razor blade and appropriate solvents (e.g. EBR or equivalent) before use. The outcome and success of processing is greatly dependent on the cleanliness and attention to detail during each successive processing step.

Titanium Foils (200 μm for Pattern Studies)

1. Cut foil with sharp scissors into 2 $\frac{3}{4}$ " x 2 $\frac{3}{4}$ ". Trim corner tips by $\frac{1}{2}$ " so that the foil will easily fit onto a 100 mm Si wafer (this is important for subsequent deposition steps).
2. Peel off white film protecting mirror-finish polished Ti. Only single-side polished (SSP) foils are needed for this thickness. Reverse unpolished side has a hazy rolled finish.
3. Place foil flat, with polished side up, in a clean and appropriately-sized glass dish and amply cover with solvent. Do not double-up foils or polished surface will be scratched.
4. Sonicate for 3 min each in acetone and isopropanol at highest frequency and intensity and follow with a 3 min rinse in DI water. Make sure have enough acetone in the dish to prevent evaporation and drying out at any point. The remaining residue is impossible to remove.
5. Place DI water-rinsed foil on a clean absorbent wipe and dry with N_2 gun.

Titanium Foils (80 μm for Stents)

1. Cut with sharp scissors into 1 $\frac{1}{4}$ " by 1 $\frac{1}{4}$ " square.
2. Peel off white film protecting polished Ti. Double-side polished (DSP) foils are needed for this thickness.
3. Place foil flat, in an aluminum dish and amply cover with solvent. Do not use a glass dish or double up the foils or the polished surfaces will be scratched.

4. Sonicate for 3 min each in acetone and isopropanol at highest frequency and intensity and follow with a 3 min rinse in deionized water (DI). Make sure have enough acetone in the dish to prevent evaporation and drying out at any point. The remaining residue is impossible to remove.
5. Place DI water-rinsed foil on a clean absorbent wipe and dry both sides of the foil with N₂ gun.

Silicon Wafer (100 mm diameter and 500 μm thick)

1. Place SSP Si wafer, with polished side up, flat in a glass dish.
2. Sonicate for 3 min each in acetone and isopropanol at highest frequency and intensity and follow with a 3 min rinse in deionized water (DI). Make sure have enough acetone in the dish to prevent evaporation and drying out at any point. The remaining residue is impossible to remove.
3. Place DI water-rinsed wafer on a clean absorbent wipe and dry with N₂ gun.
4. O₂ plasma clean (Technics/PE-IIA) for 1 min at 100 W substrate power and 300 mT chamber pressure (Or 2 min at 350°C with Gasonics/Aura 2000-LL Downstream Asher).
5. Pour enough hydrofluoric acid (HF) into a plastic dish to cover a wafer. Be sure to wear appropriate acid gloves, apron, and face shield during all processing with HF.

6. Use plastic tweezers to place wafer into HF for 1 min. This will remove all remaining contaminants and has been shown to reduce surface roughness after Si DRIE etching.
7. Rinse wafer with DI water and dry with N₂ gun.

Silicon for Laser Interference Lithography

1. Diamond scribe a Si wafer into 1" x 1" pieces.
2. Perform steps 2-7 for '*Silicon Wafer (100 mm diameter and 500 μm thick)*'

Appendix B – Deposition (ICP PECVD)

For subsequent Ti etching, deposition of a hard mask is needed to increase selectivity between the mask and the Ti, and to prevent the PR from affecting the quality of the Ti etch. A hard mask is not needed for most Si processes, due to its high selectivity/compatibility with PR during etching. The following processes were performed on an ICP PECVD (VLR, Unaxis, St. Petersburg, FL; Process conditions: 15 mT chamber pressure, 400 W ICP source power, 5 W substrate power, 5.9 sccm 100% SiH₄, 20 sccm Ar, 10 sccm O₂, and 100°C lower electrode temperature)

Titanium Foils (200 μm for Pattern Studies)

1. Center Ti substrate on unpolished side of SSP Si carrier wafer, ensuring the foils will not interfere with mechanical clamps. No need to adhere foil to wafer with oil, grease, or tape.
2. Using above process conditions, deposit 0.2 μm SiO₂ on surface

Titanium Foils (80 μm for Stents) – Patterned Side

1. Place up to four Ti foils at a time on the unpolished side of SSP Si carrier wafer, ensuring the foils do not interfere with mechanical clamps. No need to adhere foil to wafer with oil, grease, or tape.
2. Using above process conditions, deposit 0.2 μm SiO₂ on surface.

Titanium Foils (80 μm for Stents) – Through Etch Side

Ti foils that have been previously patterned on one side need to be mounted on Si carriers with patterned side down to prevent any deposition on the patterns while preparing for through etching the opposing side.

1. Prepare Si carriers slightly undersized from the 1 1/4" x 1 1/4" Ti foils by diamond scribe (so that burrs on Ti from cutting can overhang). Use the standard solvent cleans outlined in Appendix A.
2. Cut a piece of double-sided thermally conductive adhesive tape (9882, 3M, St. Paul, MN) to cover the Si.
3. Remove one side of the tape's protective film, exposing the adhesive. With adhesive side facing the Si carrier, use a razor blade to advance the tape onto the Si and prevent any air pockets. Trim remaining tape around Si carrier with razor blade.
4. Remove protective film from remaining side of tape. Center foil over tape with patterned side facing down and firmly press foil down into tape with a non-shedding wipe, beginning on one side of foil and advancing across, to prevent air pocket formation.
5. Place up to four Ti foils mounted on Si carriers on the unpolished side of SSP Si carrier wafer, ensuring the foils do not interfere with mechanical clamps. No need to adhere foil to wafer with oil, grease, or tape.
6. Using above process conditions, deposit 4.2 μm SiO_2 on surface.

7. If air pockets form between the foil and Si wafer (evidenced by a raised surface), soak samples in acetone until the foils release from the Si carriers, perform standard solvent cleans as specified in Appendix A, and follow steps 2-4 to remount.

Si Substrates for Laser Interference Lithography

1. Place up to four 1" x 1" Si substrates at a time on the unpolished side of SSP Si carrier wafer, ensuring the foils do not interfere with mechanical clamps. No need to adhere the Si to the carrier wafer with oil, grease, or tape.
2. Using above process conditions, deposit 0.2 μm SiO_2 on surface.

Appendix C – Lithography

Before beginning any lithography, the following steps must be completed, regardless of the substrate type or lithographic method:

1. Dehydrate substrate at 110°C-135°C for 5 min shortly before next process steps to improve adhesion of resist. Thoroughly clean the hotplate with razor blade and appropriate solvents (e.g. EBR or equivalent) before use.
2. O₂ plasma clean (Technics/PE-IIA or similar tool) for 1 min at 100 W substrate power and 300 mT chamber pressure (Forgo this step on Si wafers to be used with stepper).
3. Wet an absorbent wipe with acetone and clean an appropriately-sized vacuum chuck for the spinner. The vacuum portion of the chuck should be smaller than your substrate to avoid any resist getting sucked into the vacuum system.
4. Center your substrate on the clean vacuum chuck and turn on vacuum.
5. Use N₂ gun to blow any dust or particles from the substrate surface while starting the spin of your sample. This has the twofold advantage of ensuring the vacuum chuck is operational and has adequate vacuum to hold the substrate before applying resist, and it aids in migrating dust particles that may have been stirred up from the spinner when using the N₂ gun.

Contact Lithography

Contact lithography (MJB 3 UV400, Suss MicroTec, Germany) is used for defining the stent design on Ti.

1. Pipette enough hexamethyldisilazane (HMDS) to coat the surface and let sit for 30 s. If HMDS comes from a common source, use a syringe and filter to reduce particles.
2. Spin HMDS at 3000 RPM for 30 s.
3. Allow HMDS vapors to dissipate from the spinner for 1 min.
4. Pipette enough AZnLOF 2070 to cover the substrate surface. Cut end of clean pipette off for a larger hole and facile resist delivery.
5. Remove all bubbles using another pipette to prevent uneven resist coating.
6. Spin AZnLOF 2070 at 2500 for 30 s (~ 7.5 μm thick resist).
7. While waiting 5 min for the resist to settle, leave the substrate on the vacuum chuck and use a clean razor blade to remove the edge bead. Bring razor down parallel to the edge of the substrate and scrape off the resist. Repeat for all four sides, wiping off resist from the blade after each side.
8. Soft bake for 8 min at 100°C and let cool before exposing.
9. Check backside of substrate for particles or resist residue. If present, use acetone and swab to remove before proceeding to exposure.
10. Center wafer on MJB 3 vacuum chuck and align mask pattern to shoot at the center of the substrate. Take care that all sides of the mask pattern to be transferred are within the boundaries of the resist on the substrate.
11. Expose for 25 s.
12. Remove wafer from MJB 3 and let sit for 5-10 min while resist reactions are occurring.

13. Post-exposure bake for 1 min at 110°C.
14. Develop for 1 min 30 s in MIF 300. Place substrate in a plastic basket to aid in stirring the sample during the entire develop time.
15. Rinse with DI water and dry with N₂ at ≤ 20 psi.
16. Check under microscope for feature definition and add more time if needed before the hard bake.
17. Hard bake for 2 min at 115°C.
18. O₂ plasma descum for 20s at 300 mT and 100W.

Lithographic Techniques for Sub-Micron Patterning of Titanium

Stepper UV Lithography

Different UV systems were used to increase the resolution of our patterns as they became available. As a result, the GCA 200 i-line Wafer Stepper (0.5 μm resolution) was used in conjunction with a 9 pattern mask to create down to 0.5 μm features; and the ASML PAS 5500/300 DUV Stepper (0.15 μm resolution) was used in conjunction with a 16 pattern mask to create down to 0.15 μm features. The process for each tool is addressed below. For both systems, Si wafers are the substrate of choice.

GCA 200 i-line Wafer Stepper (0.5 μm resolution)

Results in a 3x3 array of 9-pattern gratings.

1. Pipette enough hexamethyldisilazane (HMDS) to coat the surface and let sit for 30 s. If HMDS comes from a common source, use a syringe and filter to reduce particles.
2. Spin HMDS at 3000 RPM for 30 s.
3. Allow HMDS vapors to dissipate from the spinner for 1 min.
4. Pipette enough AZnLOF 5510 to cover the substrate surface.
5. Remove all bubbles using another pipette to prevent uneven resist coating.
6. Spin AZnLOF 5510 at 3000 RPM for ($\sim 1 \mu\text{m}$ thick resist).
7. Soft Bake at 90°C for 1 min.
8. Check backside of substrate for particles or resist residue. If present, use acetone and swab to remove before proceeding to exposure. This is especially important for the stepper, as any backside-of-substrate contaminants can cause major lithography issues.
9. Use N_2 gun to blow off any particles on the vacuum chuck before mounting.
10. Expose for 0.28 s with a 10 focus offset. This is a good starting point, but due to the inherent drift in the tool, a focus/offset array will need to be performed before each run. The focus can be incremented by 5 and the exposure by 0.01.
11. Post-exposure bake for 2 min at 110°C .
12. Develop for 2 min in 300 MIF with constant agitation (preferably using a cassette carrier).

13. Rinse with gentle DI water (make sure water flow does not come directly on features) and dry with N₂ at ≤ 20 psi.
14. Check under microscope for feature definition and add more time if needed before the hard bake.
15. Hard bake for 2 min at 115°C.
16. O₂ plasma descum for 20s at 300 mT and 100W.

ASML PAS 5500/300 DUV Stepper (0.15 μ m resolution)

Results in a 2x2 array of 16-pattern gratings.

1. Pipette (with filter and syringe) enough AR2 to mostly cover the wafer and remove bubbles quickly.
2. Spin AR2 at 3000 RPM for 30 s (~680 – 715 Å thick).
3. Pick up wafer with tweezers and while holding it, swab the ring of AR2 off the backside. Readjust tweezers to a new location to ensure all the AR2 is removed from under tweezer location as well (Here it is advisable to have two sets of wafers to negotiate the change and keep the wafer clean). This step must be completed before the AR2 bake because it is impossible to remove after the bake and will interfere with the stepper lithography.
4. Bake AR2 at 220°C for 1 min. Make sure to have the wafer in the center of the hotplate where it is the most likely to be accurate. The DUV coatings are extremely heat sensitive and a few seconds off from the required baking time can

alter the lithography results. Using two tweezers here can aid in wafer placement and removal from hotplates.

5. Cool wafer on one sheet of non-shedding wipe on the bench for 3 min (Note: the number of wipes you set the wafer on will affect the cooling of the wafer and alter the lithography results).
6. Place wafer on vacuum chuck and remove any particles with N₂ gun.
7. Pipette (with filter and syringe) enough UV210-0.3 to mostly cover the wafer. Spin immediately and do not let sit.
8. Spin UV210-0.3 at 5000 RPM for 30 s.
9. Bake UV210-0.3 for 1 min at 130°C.
10. Cool wafer on one sheet of non-shedding wipe on bench for 1 min.
11. Check the backside of wafer and remove any resist or particle with swab and EBR 100 or N₂ gun.
12. Expose 22 MJ/cm² with -0.1 focus offset (numerical aperture: 0.63; σ_{outer} : 0.8; σ_{inner} : 0.5).
13. Post-exposure bake for 90 s at 130°C.
14. Cool wafer on one sheet of non-shedding wipe on bench for 1 min.
15. Submerge wafer in 300 MIF and let sit for 45s. Do not agitate.
16. Rinse with gentle DI water (make sure water flow does not come directly on features) and dry with N₂ at ≤ 20 psi.
17. Check under DUV microscope for feature definition and add more time if needed before the hard bake.

18. To use for imprinting, remove the outer PR between your patterns and the wafer edges with a cotton swab and acetone (This will improve contact and filling between the imprint master and the substrate). The acetone has fumes that affect the surrounding PR, so it is important not to swab too close to the features. This remaining PR can be removed with a razor blade.

Laser Interference Lithography

This is a custom-built 250 nm pitch system set up in a Lloyd's mirror configuration. To be used with 1" x 1" Si substrates.

1. Pipette (with filter and syringe) enough XHRiC-11 to cover substrate.
2. Spin XHRiC-11 at 3000 RPM for 30 s (~120 nm thick).
3. Bake XHRiC-11 at 175°C for 1 min.
4. Cool wafer for 2 min.
5. Pipette THMR-IP36000HP-D resist at 5000 RPM for 30 s (~250 nm thick).
6. Bake at 90°C for 90 s.
7. Cool wafer for 1 min while cleaning the resist off the back with EBR 100 and a swab.
8. Orient the mirror and holder angle to be 54°. This corresponds to a pitch of 200 nm.
9. Expose the resist with an energy dose of 110 MJ (Calculate the time to expose based on $\text{Time} = \text{Energy(kJ)} / \text{Power}$).
10. Post-exposure bake at 115°C for 2 min.

11. Develop in AZ300MIF for 15 s using plastic basket to agitate and hold sample.
12. Rinse with gentle DI water (make sure water flow does not come directly on features) and dry with N₂ at ≤ 20 psi.
13. O₂ plasma descum for 20s at 300 mT and 100W.

Nanoimprint Lithography

Nanoimprint lithography mechanically brings the Ti foil coated with thermal resist in contact with a patterned Si imprint master to transfer the features. Both the imprint master and Ti foil are encapsulated and then pressed together with increasing pressure. For optimal filling and peeling characteristics of the pattern transfer, the following process conditions are used (NX2000, Nanonex, Inc., Monmouth, NJ):

1. 2 min pump down
2. 2 min 140°C
3. 10 min 140°C/500 psi
4. 1 min 120°C/500psi
5. 1 min 100°C/500psi
6. 1 min 80°C/500psi
7. 1 min 60°C/500psi
8. 1 min 55°C/500psi and vent

Ti Foil Preparation

1. Pipette (with filter and syringe) enough MRI 7020 to cover substrate.
2. Remove any bubbles with another clean pipette.
3. Spin MRI 7020 at 2000 RPM for 30 s (~250 nm thick).
4. Bake for 3 min at 140°C. Foil inherently does not lay flat on the hotplate.

Imprint Master Preparation

1. Sonicate for 3 min in acetone and isopropanol at highest frequency and intensity and follow with a 3 min rinse in deionized water (DI). Make sure have enough acetone in the dish to prevent evaporation and drying out at any point. The remaining residue is impossible to remove.
2. Place DI water-rinsed wafer on a clean absorbent wipe and dry with N₂ gun \leq 20 psi.
3. Dehydration bake at 115°C for 5 min. Do not use O₂ plasma to clean the imprint master because it removes the hydrophobic MVD monolayer on the Si surface.

Nanoimprint Tool Preparation and Use

1. Wipe silicone bladders clean with isopropanol. These need to be cleaned between each run.
2. Mount silicone bladders into system, confirming that there are no wrinkles to prevent the sealing of bladders to each other.
3. Use N₂ to remove any particles from surface of Si imprint master and Ti foil.

4. Immediately place Ti foil face down, centered over the Si imprint master patterns.
5. Center the Si imprint master/Ti (with Si on bottom) on the lower silicone bladder.
6. Place the upper silicone bladder into place and gently slide the drawer closed, making sure not to jolt the drawer into the latch, which, if forceful enough, can move your samples relative to each other and possibly damage the Si patterns on the imprint master.
7. Run the imprinting process with the above parameters.
8. Immediately remove the samples before they cool further and peel them in the direction of the grooved patterns (start from the Si wafer flat). Be diligent to pull the Ti foil off the Si imprint master only in a direction normal to the Si wafer surface. This will prevent shearing any of the patterns off the imprint master.

Appendix D – Reactive Ion Etching

Three different RIE tools were used based on the tool capability and needs of the substrate. The process for each of those tools is outlined below.

RIE #5 Programmable, Loadlocked Chlorine-Based System, Plasmatherm (Unaxis)

The RIE#5 is used for etching the antireflective coating (AR2) used in conjunction with the ASML.

1. 10 min O₂ clean with clean carrier wafer (manual mode).
2. Place the Si wafer with PR-pattern side up on another Si wafer and place into load lock. No need for any oil or adhesives to hold the two wafers together or to transfer heat. Perfect alignment of the two wafers on top of each other is necessary, though.
3. 30 s O₂ etch of the AR2 (20 sccm O₂, 10 mT, 100W; manual mode).

Si ICP RIE, Plasmatherm 770 SLR, Unaxis

This ICP RIE is specifically used for etching Si and is used for defining all the Si patterning coming from the steppers. The recipe cao_n_01 (Process conditions: 19 mT chamber pressure, 825 W ICP source power, 15 W substrate power, 54 sccm C₄F₈, 26 sccm SF₆, 20 sccm Ar, and 10°C lower electrode temperature) was used for seasoning and all shallow Si etches.

1. 30 min O₂ clean with clean Si wafer (manual mode).
2. 1 min Si etch season on clean Si wafer (recipe cao_n_01).

3. 2 min 55 s Si etch (~250 nm deep) on PR-patterned Si wafer to be used for imprinting (recipe cao_n_01). No need for carrier wafer. Note: If making Si samples for cell study tests, etch for ~ 12 min to yield ~ 1.3 μm deep features.

ICP RIE, E620-R&D, Panasonic Factory Solutions

This ICP RIE is compatible with processing metals, so all the Ti etching processes are in this tool. Due to the high number of differing etches and cleans, the process conditions for each etch and clean will be listed below with an etch or clean name. The etch or clean name will then be referenced in the tool process flow.

- *O₂ Clean* – Process conditions: 37.5 mT chamber pressure, 900 W ICP source power, 100 W substrate power, and 40 sccm O₂.
- *CF₄/O₂ Clean* – Process conditions: 37.5 mT chamber pressure, 700 W ICP source power, 100 W substrate power, 50 sccm CF₄, and 40 sccm O₂.
- *Residual PR Etch* – Process conditions: 3.75 mT chamber pressure, 75 W ICP source power, 65 W substrate power, and 49 sccm O₂.
- *CHF₃/CF₄ SiO₂ Etch* – Process conditions: 3.75 mT chamber pressure, 900 W ICP source power, 50 W substrate power, 20 sccm CHF₃, and 20 sccm CF₄.
- *Sub-Micron Ti Etch* – Process conditions: 3.75 mT chamber pressure, 400 W ICP source power, 100 W substrate power, 40 sccm Cl₂, and 4 sccm O₂.
- *SiO₂Vert Etch* – Process conditions: 3.75 mT chamber pressure, 900 W ICP source power, 200 W substrate power, 40 sccm CHF₃.

- *Ti Deep Etch* – Process conditions: 15 mT chamber pressure, 400 W ICP source power, 100 W substrate power, 100 sccm Cl₂, 5 sccm Ar, and 0 or 1 sccm O₂ depending on the Ti manufacturing batch.
- *SF₆/Ar SiO₂ Etch* – Process conditions: 7.5 mT chamber pressure, 600 W ICP source power, 50 W substrate power, 50 sccm SF₆, and 10 sccm Ar

All etching performed in this tool necessitates the use of oil (Santovac 5P-Ultra Pump Oil) or double-sided thermally conductive adhesive tape (9882, 3M, St. Paul, MN) to aid in heat dissipation from the sample. For the oil, use the wooden end of a cotton swab to very thinly apply the oil to the back of the sample before mounting to the larger carrier. If needed, place under vacuum to remove air bubbles in the oil after mounting. It is important to avoid applying too much oil that seeps out and pools along the sample sides, as it will lead to oil migrating onto the substrate surface. To clean the oil off the 6” Si carrier wafers after removing mounted samples, use acetone and an absorbent swab.

Ti Surface Patterning

Both 1 ¼” x 1 ¼” 80 μm Ti foils and 2 ¾” x 2 ¾” 200 μm Ti foils need to be mounted with double-sided thermally conductive adhesive tape prior to mounting. For the 1 ¼” x 1 ¼” Ti foils, mount on diamond-scribed Si carriers slightly smaller than the Ti foil; and for the 2 ¾” x 2 ¾” Ti foils, mount in the middle of a 6” Si carrier. Remove one side of the tape’s protective film, exposing the adhesive. With adhesive side facing the Si carrier, use a razor blade to advance the tape onto the Si and prevent any air pockets. If

multiple strips of tape are needed due to the width of the area being covered, place the tape next to each other so there is neither gap nor overlay. Trim remaining tape around 1 ¼" x 1 ¼" Si carrier with razor blade. Next, remove protective film from remaining side of tape. Center foil over tape with patterned side facing up and firmly press foil down into the tape with tweezer tips, beginning on one side of foil and advancing across the length of the foil and around each pattern space. This will help prevent air pocket formation. Once pressed down, repeat firmly pressing down (but not too hard or the Si wafer will break) all the unpatterned areas around and in between patterns.

If working with 1 ¼" x 1 ¼" Ti foils on Si carriers, they must be mounted with a thin layer of Santovac 5P-Ultra Pump Oil to a 6" Si carrier. Thinly apply the oil to the back of the sample and place up to four samples in the middle of a 6" Si carrier. Once mounted on the 6" Si carrier, keep covered with the lid of a substrate holder while outside the etching chamber to keep the sample clean and safe. The following is now applicable to either foil type.

1. 10 min O₂ Clean on clean 6" Si wafer.
2. 3 min 30 s Residual PR etch (season) on a clean 4" Si wafer coated with mr-I 7020 (see Appendix C for spin parameters and bake times) mounted on a clean 6" Si with Santovac 5P-Ultra Pump Oil.
3. 1 min 55 s Residual PR etch on 6" Si carrier mounted Ti patterns. This removes remaining PR in the bottom of feature trenches after 149mprinting
4. 10 min* O₂ Clean on clean 6" Si wafer.

5. 1 min 55 s CHF₃/CF₄ SiO₂ Etch (season) on a clean 6" Si wafer.
6. 1 min 55 s CHF₃/CF₄ SiO₂ Etch on 6" Si carrier mounted Ti patterns. This defines pattern into SiO₂.
7. 5 min* O₂ Clean on clean 6" Si wafer.

At this point the larger 2 3/4" x 2 3/4" Ti foils need to be diced into their individual 9- or 16 pattern samples via the dicing saw (see Appendix E), and the smaller Ti foils need to be cleaned via the procedures in Appendix A, with the addition of softly swabbing the patterned surface while submerged in acetone to remove any residue the solvents missed. After dicing and cleaning the samples, they can be remounted on a 6" Si carrier wafer with Santovac 5P-Ultra Pump Oil and the etching process can continue. Note: If the larger foils are not diced into smaller samples, micromasking occurs during the Ti etch. Also, PR must be removed before the Ti etch for similar reasons.

8. 10 min O₂ Clean on clean 6" Si wafer.
9. 1 min 20 s Sub-Micron Ti Etch on 6" Si carrier mounted Ti patterns (see Appendix G for etch depth). Up to four 16-pattern or six 9-pattern samples can be mounted on a single 6" Si carrier for this etch. Micromasking precludes mounting more than this specified amount.
10. 5 min* CF₄/O₂ Clean clean 6" Si wafer.
11. Move samples from the 6" Si carrier used for the Sub-Micron Ti Etch to a new 6" Si carrier without solvent cleaning.

12. 1 min 45 s CHF₃/CF₄ SiO₂ Etch on 6" Si carrier mounted Ti patterns. This removes the remaining SiO₂ on the pattern ridge tops. As many samples as can fit on a 6" Si wafer can be etched during this step.
13. 10 min* O₂ Clean on clean 6" Si wafer.

Ti Through Etching

To define the stent geometry as a whole, the 80 μm Ti foils are through etched. This process is described below.

1. 10 min O₂ Clean on clean 6" Si wafer.
2. Mount Ti foil taped to Si carrier to 6" Si carrier wafer with Santovac 5P-Ultra Pump Oil. Up to four samples can be mounted for the next step.
3. 19 min SiO₂ Vert Etch on 6" Si carrier mounted Ti.
4. Remove substrates from 6" Si carrier and perform a standard solvent clean (see Appendix A).
5. Remount the substrates with Santovac 5P-Ultra Pump Oil on a new 6" Si carrier.
6. 19 min* O₂ Clean on clean 6" Si wafer.
7. 55 min Ti Deep Etch on 6" Si carrier mounted Ti. Up to 2 substrates can be etched at a time.
8. Remove Ti Deep Etched substrates from 6" carrier.
9. 30 min CF₄/O₂ Clean on clean 6" Si wafer.

At this point, the passivation needs to be removed from all Ti etched samples by wet etching (see Appendix E). Upon conclusion of removing the passivation, the etched stents need to be released from the tape and remounted on PR for the final etch steps. Other forms of mounting were tried (e.g. oil, tape) but resulted in interference with the etch.

10. To release the stent from the tape, place samples in aluminum cups filled with 1165. Sonicate in heated bath at high frequency and intensity until the stents are released.
11. Rinse stents with acetone, methanol, isopropanol, and DI water by utilizing a non-shedding wipe as a filter and an aluminum cup as a reservoir to catch the liquid.
12. Air dry stents on an absorbing wipe.
13. Meanwhile, scribe a piece of Si large enough to hold all the stents. Clean the Si piece using the standard solvent cleans in Appendix A and dehydrate bake for 115°C for 5 min.
14. Pipette enough SPR 220-7 to cover the Si piece. This is used to hold the stents in place during the final etch steps and must be a positive resist because they are easier to clean off the Ti surface.
15. Spin SPR 220-7.0 at 2000 RPM for 30s.
16. With tweezers, orient the stents SiO₂-side up on top of the PR.
17. Gently lay a non-shedding wipe over the stents and set a Si wafer or other flat implement on the non-shedding wipe.

18. Apply firm pressure to the top Si wafer in order to uniformly embed the stents into the PR.
19. Remove Si wafer and non-shedding wipe to reveal stents embedded in the PR coated Si piece.
20. Hard bake at 115°C for 2 min.
21. Mount Si piece with embedded stents on 6" Si carrier wafer with Santovac 5P-Ultra Pump Oil.
22. 15 min SF₆/Ar SiO₂ Etch to remove remaining oxide from stents. An SF₆/Ar recipe is required over a CHF₃/CF₄ based etch because the latter leads to redeposition of fluorocarbons on the sidewalls.
23. Remove mounted Si piece from 6" carrier wafer and release stents by repeating steps 10-12.

*May need to increase these times depending on the number of samples processed before cleaning.

Appendix E – Miscellaneous Tools and Methods

Molecular Vapor Deposition (MVD)

The hydrophobicity of a Si imprint master must be improved through MVD (MVD 100E, Applied Microstructures, Inc., San Jose, CA) to improve release from the substrate polymer. Procedures for applying this monolayer are detailed below. The FDTS needs to be reapplied every 10-15 imprints.

1. Mix in a glass dish 3:1 sulfuric acid to hydrogen peroxide (Piranha) on a hotplate set to 80°C. Wait until bubbling occurs or add more hydrogen peroxide until bubbling starts.
2. Place Si wafer in Piranha with patterned side up for 20 min (Use metal tweezers with no coatings). If the wafer floats, use metal tweezers to encourage wafer to stay submerged.
3. Remove wafer from Piranha, rinse with DI, and N₂ dry both sides of wafer.
4. O₂ plasma descum for 3 min at 300 mT and 100W.
5. Repeat steps 3 and 4.
6. Take Si sample directly from last phase of O₂ ashing and place in MVD chamber and pump down.
7. Run standard single layer FDTS (Process conditions: 23°C chamber temperature, 600 s reaction time of H₂O and FDTS)
8. Bake Si wafer at 140°C for 2 min.

Dicing Saw

1. Spin SPR 220-7.0 at 2000 RPM on all samples to be diced to protect substrate surfaces from machine oil or any particles that prove difficult to remove.
2. Bake at 115°C for 1 min.
3. Follow procedures for mounting substrates onto single-sided tape for dicing.
4. Use blade 2.050-8C-54RU with the 52 mm hub.
5. Following dicing, samples need to be solvent cleaned (see Appendix A) with the addition of soft swabbing the surface during the acetone step.

Note: If cutting the 9- or 16-pattern, the spacing between each set of patterns is 2 mm, so starting cuts for both should be 1 mm away from the edge. Indices for the 9- and 16-patterns are 16.9 mm and 22 mm, respectively. If cutting either the 9- or 16- patterns into their sub-patterns, the starting cut should be below the dimension label block and the index is 5 mm.

Wet Etching with TFTN

The use of TFTN (diluted hydrofluoric acid to 20-30%) to remove sidewall passivation is detailed below.

1. Heat TFTN in small glass beaker to 80°C (takes ~10 min).
2. Submerge substrate with stents into heated TFTN and agitate for 1 min. Top and bottom of stents are protected from wet etching by the remaining SiO₂ and tape.
3. Remove and rinse with DI water and N₂ dry.

Appendix F – Tool Process Flow

Stepper Imprint Master * (50 – 0.15 μm patterns)

1. Clean – Appendix A
2. Stepper UV Lithography – Appendix C
3. RIE – Appendix D
4. Si ICP RIE – Appendix D
5. MVD – Appendix E

*Skip step 5 for patterned Si substrates used in cell studies.

Laser Interference Lithography Imprint Master (0.1 μm patterns)

1. Clean – Appendix A
2. Deposition (0.2 μm) – Appendix B
3. Laser Interference Lithography – Appendix C
4. ICP RIE – Appendix D
5. Si ICP RIE – Appendix D
6. MVD – Appendix E

*Skip step 5 for patterned Si substrates used in cell studies.

Patterned Substrates (200 μm Ti foils)

1. Clean – Appendix A
2. Deposition (200 μm) – Appendix B
3. Imprint Lithography – Appendix C
4. ICP RIE – Appendix D

- a. Dicing Saw – Appendix E

Patterned Stents (80 μm Ti foils)

1. Clean – Appendix A
2. Deposition (0.2 μm) – Appendix B
3. Imprint Lithography – Appendix C
4. ICP RIE – Appendix D
5. Deposition (4.2 μm) – Appendix B
6. Contact Lithography – Appendix C
7. ICP RIE – Appendix D
 - a. TFTN Wet Etching – Appendix E

Appendix G – Ti Material Properties

To determine the mechanical properties of the 80 μm stent material, dogbone-shaped tensile test specimens were made from the material via the TI DRIE process (Parker *et al.* 2005) (see 2.6 Titanium Etching). It is known that the way a material is made can have an effect on the anisotropy of the mechanical properties, cold rolling being no exception (Bryukhanov *et al.* 1979). For this reason, three sets of dogbones were created with three dogbones in each set. The long axis of each set was oriented at a different angle (0° , 45° , and 90°) to the rolling direction in order to capture the full range of mechanical response. The Ti dogbones were clamped into a material testing system (810, MTS, Eden Prairie, NM) and pulled in tension to failure. Reflective tape placed on either side of the narrow dogbone section was used in conjunction with a laser extensometer (LE Model, Electronic Instrument Research, Irwin, PA) to gather strain data. An average of the stress-strain curves for each angle (Figures G-1, G-2, G-3, G-4) was made and the mechanical properties are summarized in Table G-1

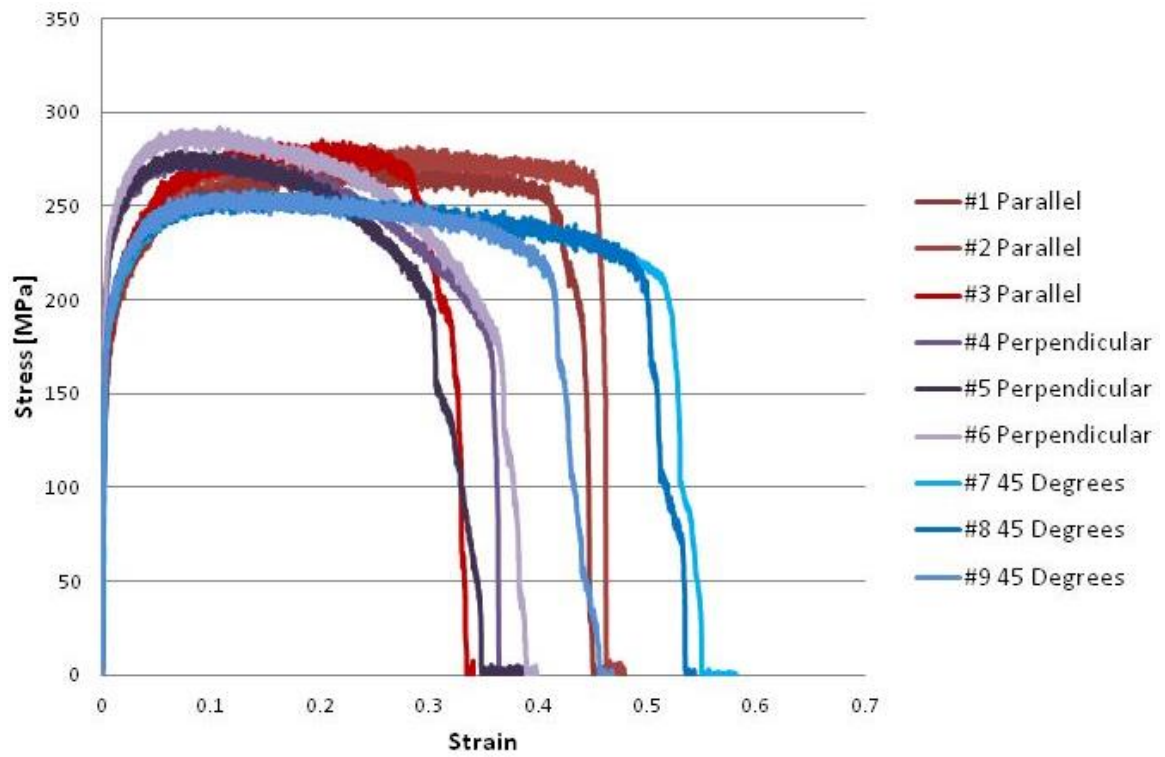


Figure G-1. Stress-strain data for each Ti dogbone tensile test preformed.

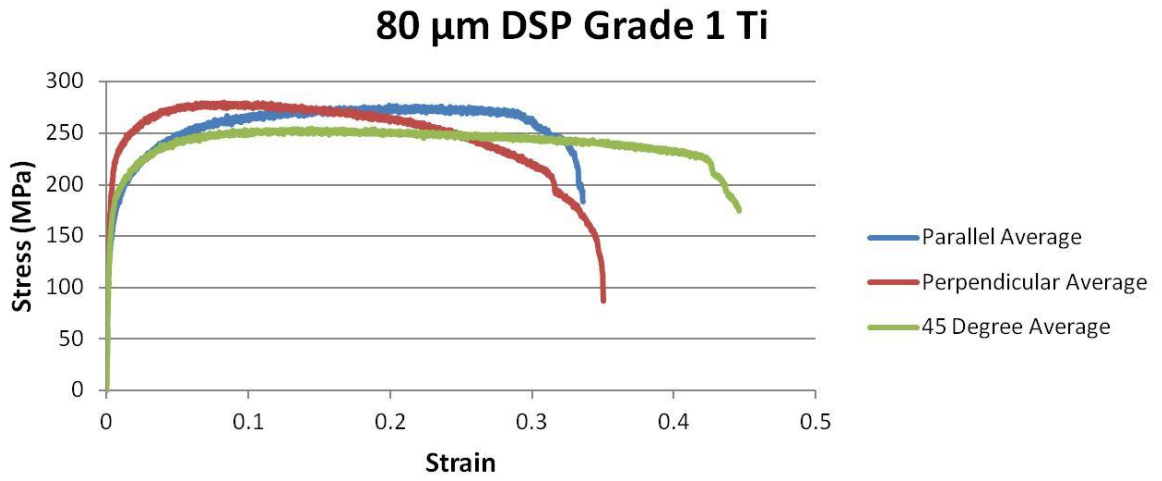


Figure G-2. Ti dogbone stress-strain data averaged according to orientation.

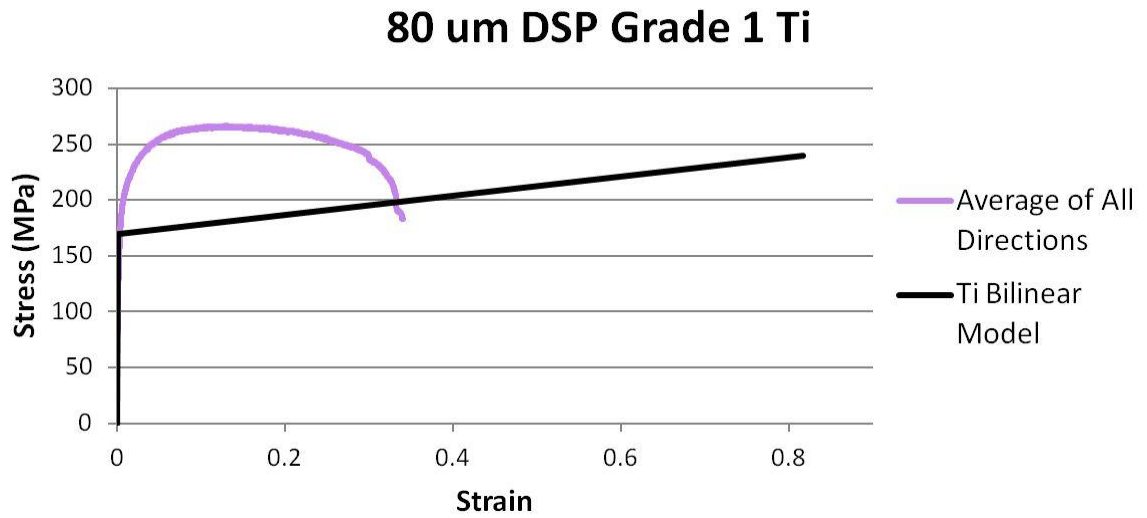
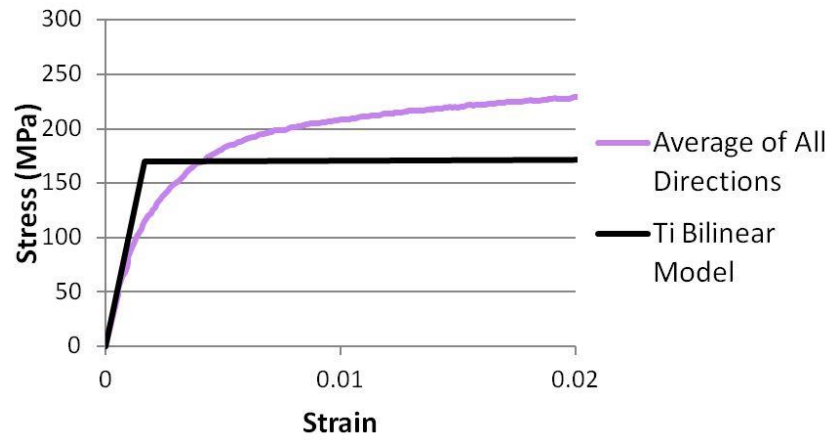


Figure G-3. Ti dogbone stress-strain data averaged across orientations.

80 μm thick DSP Grade 1 Ti



Figures G-4. Close-up of the elastic region of Figure G-3.

Elastic Modulus	116.5 GPa
Yield Stress (based off 0.2% offset)	167 MPa
Ultimate Tensile Strength	266 MPa

Table G-1: Average Mechanical Properties for 80 μm thick CP Grade 1 Ti.

Appendix H – Finite Element Analysis via Femap

The following includes all the steps to setup a stent model in Femap for expansion and compression analysis.

Importing Geometry

1. File > Import > Geometry
2. Select stent geometry file generated from program like Solidworks – must be saved as a parasolid (.x_t)
3. Change ‘Geometry Scale Factor’ to 1. All units are assumed to be meters and it will try to convert automatically to inches if left unchanged.
4. Click OK

Section Geometry to Facilitate Meshing

1. Geometry > Solid > Slice
2. Select the desired solid to slice (to ensure the correct solid was chosen, use the highlight button)
3. Under ‘Methods,’ choose the best method for slicing the surface. Depending on the geometry to be sliced, ‘Points,’ ‘Global Plane,’ or ‘Surface Normal’ are good options.
4. According to the method chosen, slice the surface. Be sure that both sides of the slice are the same length, or meshing errors will occur.
5. Repeat the above steps as many times as needed to allow for easy meshing

Create Half Cylinders to Imitate Needle Threading

First, a workplane is established from which the half cylinder geometry can be drawn and extruded. This workplane should be perpendicular to the longitudinal axis of the stent and spaced slightly away from the end of the stent so that the half cylinder are longer than the stent.

Create a Point Slightly Removed From the End of the Stent

1. Geometry > Point
2. Methods > Offset
3. Choose a point on the longitudinal end of the stent.
4. Use your discretion to offset the point away from the stent in the longitudinal direction.
5. Click OK

Establish the Workplane at the Created Point

6. Press F2 and check 'Draw Workplane'
7. Click 'Select Workplane'
8. Methods > Global Plane
9. Right click on screen and choose 'snap to point'
10. For the base, choose the created point
11. Select the appropriate plane for being perpendicular to the longitudinal direction
12. Click OK

Create Points for Arc Centers

First create a point in the center (center of both thickness and width) of stent

13. Geometry > Point

14. Methods > Between

15. Choose a point on the upper face and outer side of one sidebeam.

16. Choose the second point to be the lower face and outside of the opposing side beam. This should create a point in the center of the stent as you look at it down the longitudinal axis.

17. Click OK

Second, offset points to be the center of the arcs from the last created point.

18. Geometry > Point

19. Methods > Offset

20. From the previous created center point, offset points so that they are the desired arc radius plus some away from two stent faces. This is so the arcs are not in contact with the stent face when the simulation begins, which can lead to instability.

Create Half Cylinder Arcs

21. Geometry > Curve-Arc > Angle-Center-Start

22. Method > On Point

23. Select the created point for the center of the arc.

24. Click OK

25. Method > Offset

26. Choose the base to be the center of the arc. Offset the radius of the arc in the desired start direction of the arc.

27. Type in 180 degrees for the angle, choosing positive or negative so that the convex part of the arc is toward the stent face.
28. Click OK
29. Repeat so that there is one arc on each side of the stent.

Extrude Half Cylinder Arcs

30. Geometry > Surface > Extrude
31. Select half cylinders.
32. Click OK
33. Methods > Global Axis
34. Select appropriate axis and positive/negative to extruded down the longitudinal axis
35. In 'Length' box enter the length of the stent plus the two overlapping sections on either end.
36. Click OK.

Create Cylinder to Imitate Balloon Expansion

1. Geometry > Curve-Circle > Radius
2. Methods > On Point
3. Choose the point you created in the center of the stent as the center of the circle.
4. In the 'Length' box, type a radius slightly smaller than the needle expanded radius of the stent. This is to ensure the cylinder and stent faces are not touching when contact elements are turned on.

5. Click OK

Extrude Cylinder

1. Geometry > Surface > Extrude
2. Select cylinder.
3. Click OK
4. Methods > Global Axis
37. Select appropriate axis and positive/negative to extruded down the longitudinal axis
- 5.
6. In 'Length' box enter the length of the stent plus the two overlapping sections on either end. The two half cylinders and the whole cylinder should all be the same length.
7. Click OK.

Create Plates to Imitate Parallel Plate Compression Testing

1. Geometry > Point
2. Method > Offset
3. Choose the previously created center point to be the base.
4. Offset a distance slightly larger than the desired expanded radius of the stent in the direction perpendicular to the stent sidebeams.
5. Repeat to mirror the created point on the other side of the stent.
6. Geometry > Curve-Line >Project Points

7. Method > Offset
8. Choose one of the points previously created in this section and offset the two points of the line parallel to the stent facet and in the directions toward the sidebeams. The offset amount should be the expected radius of the expanded stent plus 0.5 mm or so beyond. This should yield a single line parallel to the stent
9. Repeat for the other created point for a line on the other side of the stent.

Extrude Line

10. Geometry > Surface > Extrude
11. Select both lines.
12. Click OK
13. Methods > Global Axis
14. Select appropriate axis and positive/negative to extruded down the longitudinal axis
15. In 'Length' box enter the length of the stent plus the two overlapping sections on either end. The lines can be the same length at the cylinders and half cylinders.
16. Click OK.

Define Material Properties

Stent

1. Model > Materials > New
2. Input the Youngs Modulus, Poisson's Ratio, and Mass Density in the General Tab.

3. In the Nonlinear tab, choose either Elasto-Plastic (bilinear model) or the Plastic (experimental material data).
4. If choosing Elasto-Plastic:
 - a. Press the button 'Compute From Target modulus, Et' and enter the tangent modulus.
 - b. Enter a value for the 'Initial Yield Stress.'
5. If choosing Plastic:
 - a. Create a function of the material data (see below) and select that function in the 'Function Dependence' menu.
 - b. Copy and paste the yield value from the experimental material data to the 'Initial Yield Stress' field. The two values must be exactly the same.
6. Click OK

Create a Material Function

1. Model > Functions
2. Copy material data from excel and 'Paste From Clipboard.' A simplified version of the stress vs. strain data is best, where there are as few points as possible until finishing at the ultimate tensile strength (see below).
3. Choose 'vs Stress' under 'Type'
4. Click OK

Stress (Pa)	Strain
0	0
1.68 (10 ⁸)	0.003898
2.07 (10 ⁸)	0.009454
2.29 (10 ⁸)	0.020027
2.41 (10 ⁸)	0.030478
2.49 (10 ⁸)	0.041168
2.55 (10 ⁸)	0.05189
2.59 (10 ⁸)	0.062982
2.62 (10 ⁸)	0.074164
2.64 (10 ⁸)	0.085641
2.64 (10 ⁸)	0.097101
2.65 (10 ⁸)	0.108779
2.65 (10 ⁸)	0.120476
2.66 (10 ⁸)	0.132396
2.65 (10 ⁸)	0.144499
2.65 (10 ⁸)	0.156764
2.65 (10 ⁸)	0.16905
2.64 (10 ⁸)	0.181497

Table H-1: Abbreviated stress vs. strain data of 80 μm thick Ti foils for FEA.

Cylinder, Half Cylinders, and Plates

1. Model > Material > New
2. Click 'Load'
3. Choose AISI 4340 Steel. The material here doesn't matter because we are not gathering stress data from the cylinder/half cylinders and we are using ridged elements for the plates.

4. Click OK

Setting Up the Element Properties

Stent

1. Model > Properties > New
2. Click 'Elem/Property Type' and choose 'Solid'
3. Click OK
4. Under the 'Material' dropdown menu, select the material that corresponded with the desired stent material, e.g. Ti.
5. Click OK

Cylinder, Half Cylinders, and Plates

1. Model > Properties > New
2. Click 'Elem/Property Type' and choose 'Plate'
3. Click OK
4. Under the 'Material' dropdown menu, select the material that corresponded with the desired material, e.g. Steel.
5. Enter 'Thicknesses, Tavg or T1' to be 1e-10 (needs to be sufficiently small).
6. Click OK

Set Mesh Sizing

Stent

1. Mesh > Mesh Control > Size on Solid

2. Select all stent pieces and click OK.
3. Select 'Hex Meshing.'
4. Change 'Element Size' to 1.5e-5.
5. Min Elements on Edge: 2.
6. Click OK

Cylinder, Half Cylinders, and Plates

1. Mesh > Mesh Control > Size on Surface
2. Select cylinder, half cylinder, and plate pieces and click OK.
3. Select 'Hex Meshing.'
4. Change 'Element Size' to 1.5e-5.
5. Min Elements on Edge: 2.
6. Click OK

Mesh Solids and Surfaces

Stent

1. Mesh > Geometry > HexMesh Solids
2. Choose the solid property from the dropdown menu corresponding to the stent.
3. Click OK
4. If errors occur indicating that the solid is not able to be meshed, the solid may need to be sliced further. In that case, delete the mesh, slice the solid, and remesh.

Cylinder, Half Cylinders, and Plates

1. Mesh > Geometry > Surfaces

2. Choose the plate property from the dropdown menu corresponding to the remaining surfaces.
3. Click OK

Create Rigid Body Node

The rigid body node allows for facile extraction of nodal forces. All nodes linked to the rigid node will ultimately be summed and act in one accord with the rigid node.

1. Geometry > Point
2. Method > Between
3. Select the two of the points diagonal to each other on a plate (corners).
4. Model > Element
5. Press 'Type' and choose 'Rigid.'
6. Click OK
7. Under 'RBE2' tab, click 'Nodes'
8. Method > On Surface
9. Select the plate.
10. Click OK twice.
11. At the prompt 'Node 0 does not Exist. OK to Create?' click Yes
12. Methods > Offset
13. Select the point created on the plate in this section as the base.
14. Offset the node away from the stent the distance 0.001 m.
15. Make sure the coordinate system is basic rectangular.

16. Click OK

17. Repeat all steps for the second plate.

Define Boundary Conditions

Constraints - Stent

1. Constraints > New > OK
2. Constraint Definitions > On surface
3. For planar stents, all four ends of the sidebeams were selected.
4. Click OK
5. Select 'Arbitrary in CSystem.'
6. In dropdown menu, select 'Basic Rectangular.'
7. Check the box to prevent translational movement in the longitudinal direction.

Constraints – Cylinder and Half Cylinders

1. Constraint Definitions > On Surface
2. Select cylinder and half cylinders.
3. Under 'Standard Types' select 'Fixed.'
4. Click OK

Constraints – Cylinder and Half Cylinders

1. Constraints Definitions > Nodal
2. Select both rigid nodes.
3. Under 'Standard Types' select 'Fixed.'
4. Click OK

Loads- Half Cylinder

1. Loads > New > OK
2. Load Definition > On Surface
3. Select one of the half cylinders.
4. Click OK
5. Choose 'Basic Rectangular' for the coordinate system.
6. Highlight 'Displacement.'
7. Check the appropriate translation direction for moving the half cylinder toward the stent and place 1 or -1 for its value depending on the direction the half cylinder will be moving.
8. Create a time function for this load by clicking 'fxy' and link to it in the 'Time/Freq Dependence' dropdown box.
 - a. Under 'Type,' select 'vs. Time.'
 - b. Enter the following X,Y pairs: (0,0); (100, distance half cylinder would need to move to open stent to crimped diameter); (150,0); (350,0).
 - c. Click OK
9. Click OK
10. Repeat for the other half cylinder.

Loads- Cylinder

1. Load Definitions > On Surface
2. Select cylinder
3. Click OK

4. Choose 'Basic Cylindrical' for the coordinate system.
5. Highlight 'Displacement.'
6. Make sure TX is checked and has a value of 1.
7. Create a time function for this load by clicking 'fxy' and link to it in the 'Time/Freq Dependence' dropdown box.
 - a. Under 'Type,' select 'vs. Time.'
 - b. Enter the following X,Y pairs: (0,0); (100,0); (200, radius of cylinder + stent thickness – radius of final expanded state e.g. 1.5 mm); (250,0); (350,0).
 - c. Click OK
8. Click OK

Loads- Plates

1. Load Definition > Nodal
2. Select one of the rigid nodes.
3. Click OK
4. Choose 'Basic Rectangular' for the coordinate system.
5. Highlight 'Displacement.'
6. Check the appropriate translation direction for moving the plate toward the stent and place 1 or -1 for its value depending on the direction the plate will be moving.
7. Create a time function for this load by clicking 'fxy' and link to it in the 'Time/Freq Dependence' dropdown box.
 - a. Under 'Type,' select 'vs. Time.'

- b. Enter the following X,Y pairs: (0,0); (200,0); (350, distance needed to move plate to crush the stent half its original diameter).
 - c. Click OK
8. Click OK

Define Contact Elements

Stent and Half Cylinder Contact

1. Connect > Surfaces
2. Click 'Multiple' for 'Master (Target)' and select one of the half cylinder surfaces.
3. Click OK
4. Click 'Multiple' for 'Slave (Source)' and select the complementary stent surfaces that will mimic needle threading.
5. Click OK
6. Click the icon to the right of the 'Connection Property' dropdown menu to define the connection property.
7. Under the 'NX Adv Nonlin' tab, set the element birth time to 100 and death time to 250. These correspond to the time functions created earlier.
8. Click OK
9. Repeat all steps through #5 for the other half cylinder and stent connection. Since the connection property was already created, it can be selected from the dropdown menu under 'Connection Property.'

Stent and Cylinder Contact

1. Connect > Surfaces
2. Click 'Multiple' for 'Master (Target)' and select all cylinder surfaces.
3. Click OK
4. Click 'Multiple' for 'Slave (Source)' and select all stent surfaces that will be facing the balloon when crimped.
5. Click OK
6. Click the icon to the right of the 'Connection Property' dropdown menu to define the connection property.
7. Under the 'NX Adv Nonlin' tab, set the element birth time to 100 and death time to 250. These correspond to the time functions created earlier.
8. Click OK

Stent and Plate Contact

1. Connect > Surfaces
2. Click 'Multiple' for 'Master (Target)' and select one of the plates.
3. Click OK
4. Click 'Multiple' for 'Slave (Source)' and select the complementary stent surfaces that will come in contact with the plate.
5. Click OK
6. Click the icon to the right of the 'Connection Property' dropdown menu to define the connection property.

7. Under the 'NX Adv Nonlin' tab, set the element birth time to 200 and death time to 999. These correspond to the time functions created earlier.
8. Click OK
9. Repeat all steps through #5 for the other plate and stent connection. Since the connection property was already created, it can be selected from the dropdown menu under 'Connection Property.'

Set Analysis Parameters

1. Analyses > Manage
2. Click New
3. Under 'Analysis Type' select 'Advanced Nonlinear Transient.'
4. Click OK
5. Check 'Number of Processors' and enter at least 2
6. Under 'Solver Memory,' enter at least 4000
7. Click Next
8. Check 'LGSTRN'
9. Click Next 3 times
10. Click 'Extra Time Steps.'
11. Type 1750 under the first row of 'Num Steps' and 0.2 under the first row of 'Time Increment.' The total 'Num Steps' multiplied by the 'Time Increment' is equal to the total amount of time step. Choosing a larger quantity of 'Num Steps' with smaller 'Time Increment' aids in convergence.

12. Click OK
13. In the 'RBE2 opt' dropdown menu, choose 'Rigid.'
14. Click Next
15. Turn on the Auto Increment.
16. Change the 'Smallest Step Divisor' to 1000.
17. Change Max Iterations/Step to 30.
18. Turn on the Line Search.
19. Under the dropdown menu for 'Damping Method,' select 'All Steps Damping.'
20. Enter the 'Normal Damping Coefficient' to be 0.001.
21. Enter the 'Tangential Damping Coefficient' to be 0.001.
22. Click OK.

When Ready to Run an Analysis

1. Analysis > Preview Input
2. Check 'Edit Preview.'
3. Scroll down a few lines to where it says NXSTRAT.
4. Each section consists of 8 character spaces and a single entry consists of two sections. The first of these sections is a name and the second is a number, both right aligned within their 8 character section. Beginning at NXSTRAT there are entries on each row. When the row ends with a + and the next row starts with a +, the entries continue to the next row. Find the last row that starts with a +, but doesn't end with a +. If there are sections left on this last row, then add

‘PLASALG’ and ‘2’ both right justified. If there are no more open sections, add a + at the end of the last row, start a new row with a +, and then type ‘PLASALG’ and ‘2’ both right justified.

Post Processing to Gather Load vs. Displacement Data

1. Select the ‘Charting’ icon.
2. For a new data series, press the ‘xy’ button.
3. Under ‘Type,’ choose ‘XY vs. Set Value.’
4. Uncheck ‘Use All Output Sets’
5. Choose the ‘start’ and ‘end’ time points corresponding to the beginning and ending of the plates engaging the crushing of the stent.
6. Select ‘Total Constraint Force’ for the vector.
7. For ‘Location,’ select one of the rigid body nodes.
8. Click OK
9. Repeat previous steps for the ‘Total Translation’ vector.
10. When finished select ‘Copy Chart to Clipboard’ icon and transfer into excel for graphing.